Ab initio calculation of structural and electronic properties of α-Ga surfaces

Thesis submitted for the degree of

"Doctor Philosophiæ"

CANDIDATE

Marco Bernasconi

SUPERVISORS

Prof. Erio Tosatti

Dr. Guido Chiarotti

October 1993

Table of Contents

Table of Contents i

1 Introduction 1

2 Computational Method 5

3 Bulk Properties and Phase Diagram of Ga 12

3.1 Structural Properties 16

3.2 Electronic Properties 27

4 The α-Ga(001) Surface 37

4.1 Surface Structure 37

4.2 Surface Electronic Properties 52

4.3 The role of metallization in the self-wetting phenomena 69

5 The α-Ga(010) Surface 75

5.1 Surface Structure 75

5.2 Surface Electronic Properties 83

5.3 Discussion 87

6 Conclusions and outlooks 89

Acknowledgements **93**

A Non Linear Core Correction to Pseudopotential **95**

B Linear analytic method for Brillouin Zone integration in 2D **99**

C Calculated STM image **103**

Bibliography 106

1 Introduction

In this thesis I present the results of an *ab initio* study of the structural and electronic properties of the bulk crystalline phases of gallium and of the main surfaces of α-Ga which is the stable phase at normal conditions.

Gallium is a remarkable metal in several ways. It is one of few metals that do not crystallize under known conditions to any of the simple crystal structures. The phase stable at normal conditions, α-Ga, is based centered orthorhombic with eight atoms in the conventional unit cell [1]. Gallium also posseses a rather complicated phase diagram with many stable and metastable crystalline phases all closely competing for the ground state. Two phases, GaII and GaIII [2], are stable at high pressure. In addition a number of metastable phases has been identified at atmospheric pressure designated β [3], γ [4], δ [5], and ϵ.

A peculiar feature of the α phase is that each atom has only one nearest neighbor in the first coordination shell centered at 2.44 Å, and six other neighbors within 0.39 Å further apart. The structure of α-Ga can be regarded as consisting of strongly buckled planes orthogonal to the c axis connected by short bonds between the first neighbors which lie in different planes (see fig. 3.1 in chapter 3). A variety of experimental data - summarized in chapter 3 - reveal the partial covalent character of the short bonds which can be seen to form essentially covalent Ga_2 dimers. There is a long history to the literature and ideas

relating to covalency in α-Ga [6, 7]. The covalency of the dimer and its fingerprint in the electronic properties, in particular the presence of a pseudogap at the Fermi level in the electronic densities of states, has been recently confirmed by first-principle calculations by Gong *et al.* [8] and by Hafner *et al.* [9].

While repeating the calculation by Gong *et al.* we found it necessary to increase the accuracy of Brillouin Zone integrations, expecially in order to obtain the correct hierarchy of the less-stable phases. The closeness in energy of the less-stable fully metallic phases is expected to be relevant in the physics of α-Ga surfaces, since at surface the relative importance of covalency and metallicity may change.

For this reason we recalculated the properties of the phases α, β, GaII, GaIII and fcc, in part discussed by Gong *et al*, with a higher level of accuracy in k-sums and allowing now a full relaxation of all the lattice parameters (a,b,c in α-Ga for instance). In chapter 2 we present the details of our general computational framework and in chapter 3 we discuss our results for the bulk phases. Our resulting electronic properties of α-Ga represent minor changes with respect to ref. [8], while the hierarchy in energy of the losing structures is largely modified. In particular the phase named GaII by Bosio [2] (and by us hereafter) is the phase reached from α-Ga by application of hydrostatic pressure, in agreement with the experimental evidence [2]. In ref. [8] the name GaII was given, according to a older nomenclature [10], to the structure named GaIII and identified as the phase stable at high pressure and high temperature by Bosio (and by us hereafter) [2]. In addition a new pressure induced phase transition above 152 Kb is predicted from true GaII to fcc.

The double nature -covalent and metallic- of bulk α-Ga makes its surfaces especially interesting. Only few sp-metal surfaces are known to reconstruct, while reconstruction is the rule for semiconductors, where bulk covalency forces the presence of unsaturated dangling bonds. Therefore, it is interesting to study which of the two characters of α-Ga

prevails on the different surface orientations.

Gallium has a very low melting temperature ($T_m = 303K$) which suggested it to be a suitable system for the study of the disordering process at surface near T_m with Scanning Tunneling Microscope (STM). In particular theoretical arguments suggest that α-Ga should eventually display blocked surface melting [12, 11]. This comes from the presence of attractive the Van der Waals (VdW) forces between the liquid surface and the liquid-solid interface of solid gallium wetted by a thick liquid film [12]. These facts have stimulated the extensive investigation of the α-Ga surfaces with STM by Züger and Dürig [13, 14]. It turns out that the α-Ga surfaces not only do not melt, but several orientations present a remarkable thermal stability. For instance on the (001) and (010) surfaces no step diffusion nor other kind of surface mobility was detected up to T_m. Some of this apparent may be just due to insufficient diffusion at room temperature, meaning that the surfaces might still be out of equilibrium, when bulk melting takes place. More surprisingly the (001) surface is flat and atomically ordered even when macroscopic amounts of the underlying bulk are already molten [14].

We studied both the (001) and the (010) surfaces, modeled in a slab geometry within standard total energy framework. We found that in one of the two possible ideal configurations of the (001) surface the covalent character of gallium shows up by inducing half-filled bands of surface dangling bonds. As in most semiconductors, the presence of unsaturated dangling bonds produces an instability, removed by a large rearrangement of surface geometry. Based on *ab initio* calculation we propose that in the ground state the (001) surface of α-Ga is covered by two layers of GaIII, a denser phase stable in the bulk only at high pressure and temperature. This self-wetting phenomenon is favoured because the surface energy of the fully metallic GaIII is so much lower than the surface energy of ideal relaxed α-Ga surface to make it worthwhile paying for interface energy plus the

difference in bulk energy between α-Ga and GaIII which is indeed very small. At the atomic density of the thin film covering α-Ga, GaIII is known to melt 100 K above the melting point of α-Ga, probably accounting therefore for the anomalous thermal stability of (001) surface. The structural and electronic properties of the (001) surface are discussed in chapter 4. Conversely on the ideal (010) surface no covalent bonds are broken, and so no unsaturated dangling bonds are present to drive a surface reconstruction. Then on the (010) orientation, surface atoms undergo only a minor rearrangement consisting of a 14 degrees rotation of the surface Ga_2 dimers. Our results on the (010) surface will be discussed in chapter 5. Chapter 6 will be devoted to a general discussion and to conclusions.

2 Computational Method

We studied structural and electronic properties of bulk gallium phases and of α-Ga surfaces within *ab initio* total energy framework. We used standard Density Functional Theory [15] in the Local Density Approximation (LDA). For local exchange and correlation (XC) energy we adopted the parameterization of Perdew and Zuger [16]. An *ab initio* norm-conserving pseudopotential for Ga was taken in the Kleinman-Bylander form [17], constructed from the tables of Stumpf, Gonze, and Scheffler [18]. The parameters of the pseudopotential in the notation of Bachelet, Hamann, and Schluter [19] are given in table 2.1.

This pseudopotential is constructed by linearizing the XC energy with respect to valence and core contributions, i.e. in the applications of the pseudopotentials the XC energy in computed using only the valence (pseudo)charge density. This approximation is usually well suited when the overlap between core and valence charges is small. In order to test explicitly this approximation we also generated a pseudopotential with the Non-Linear Core

L	α_1	α_2	α_3	c_1	c_2	c_3	c_4	c_5	c_6
core	2.01	0.80		4.0511	−3.0511				
0	1.99	2.30	2.46	−3.6305	0.9488	−0.0793	0.1672	0.0901	0.0131
1	1.27	1.75	2.35	−3.0051	0.0581	0.0118	0.0979	0.0512	0.0136
2	1.51	1.85	1.97	−3.0412	0.1489	0.0099	−0.0891	−0.1281	−0.0416

Table 2.1: Coefficient of the pseudopotential for gallium in the Kleinman-Bylander form from ref. [18], following the notation of ref. [19].

Correction (NLCC), according to the prescriptions suggested by Louie, Froyen and Cohen [20]. The idea is to evaluate the XC energy using the total - rather than the valence- charge density: this is achieved by adding the frozen-core charge to the self-consistent valence charge. The details of the construction of the NLCC pseudopotential of Ga are reported in appendix A. However, as we will see in chapter 3, the variations in the structural parameters of bulk gallium introduced by the NLCC correction are negligible. Therefore we used the pseudopotential of ref. [18] in the surface calculations.

The surfaces were studied in the periodic slab geometry. Both surface and bulk calculations were performed by solving the Kohn-Sham (KS) equation in reciprocal space. KS orbitals were expanded in planes waves up to 14 Ry energy cutoff. We tested the convergence with respect to the energy cutoff particularly on the equilibrium volumes of bulk phases.

The use of slab geometry in the surface calculations, with large dimension d of the unit cell in the direction perpendicular to the surface, leads to small Fourier components ($G_z = 2\pi/d$) of the coulomb potential which are very sensitive to the shift of charge across the surface. This "charge sloshing" effect leads to great difficulties in achieving the self-consistent solution of KS equation. To accelerate the convergence in the iteration procedure we used the modified Broyden scheme [1] [21]. At each step in the self-consistent loop the single particle hamiltonian is diagonalized by using the Davidson's iterative diagonalization technique [22].

Brillouin Zone Integration: Since gallium is a metal in all its crystalline phases the functions to be integrated over the Brillouin Zone (BZ) in order to obtain observable quantities such as energy, charge density, etc..., are discontinuous at the Fermi level.

[1] The main advantage of this scheme resides in the mixing procedure of input and output potentials. The mixing parameter is allowed to have different values for the different Fourier components of the potential, therefore treating on different footing the small Fourier components which converge more slowly.

For this reason it is not possible to use the notion of special points which requires the differentiability of the functions to be integrated [23]. This fact leads to a very slow convergence with respect to the density of a uniform mesh in the BZ. On the other hand the closeness in energy of the different crystalline phases of gallium requires a very high accuracy BZ integration in order to have energy precision within $1\,mRy/atom$. Due to slight inaccuracy in the k-sum, previous work done in our group on bulk gallium in ref. [8], although properly reproducing the electronic properties of α-Ga did non correctly predict the hierarchy in energy of the other phases, and consequently the pressure induced phase transitions. To cure this problem we devised high precision BZ integration following the scheme proposed by Methfessel and Paxton [25]. It consists in a modification of the more popular gaussian smearing technique of Fu and Ho [24]. In general we wish to evaluate integrals over the BZ in the form

$$I = \int_{BZ} f(\mathbf{k}) z(E_f - E(\mathbf{k})) d\mathbf{k} \tag{2.1}$$

where

$$z(E_f - E(\mathbf{k})) = \int_{-\infty}^{E_f} \delta(\epsilon - E(\mathbf{k})) d\epsilon \tag{2.2}$$

In the gaussian smearing technique the δ function in 2.2 is broadened into a gaussian with variance W. By using a sufficiently large W, one immediately improves the k-sum convergence. However the only justification for this *ad hoc* procedure is that in the limit $W \to 0$ one would recover the absolutely converged result at the expense of using a prohibitively fine mesh. Thus for each choice of W the k-sum converges to a eventually different result, and the convergence with respect to W must be further checked. Methfessel and Paxton [25] suggested a more efficient way to achieve absolute convergence.

They expand the δ function in eq. 2.2 as

$$\delta(x) = \sum_{n=0}^{\infty} A_n \, H_{2n} \, e^{-x^2} \tag{2.3}$$

where $x = \frac{\epsilon - E(\mathbf{k})}{W}$, H_{2n} are Hermite polynomials, A_n are the expansion coefficients, and W is an arbitrary "linewidth". By truncating the sum in eq. 2.3 to a finite order N we obtain a spreading of the δ function. The order $N = 0$ corresponds to the simple gaussian broadening. The idea is to assign a value to W such that the k-sum converges at a chosen number of k points for $N = 0$. Then the absolute convergence is tested not by varying W, but by changing the order N of the representation of δ. The order N is determined by the required precision: for a fixed W, small N requires fewer k points at the expense of convergence to a less precise result, higher orders guarantee convergence to a correct result, but require more k points. Methfessel and Paxton showed that for a suitable choice of W and N the convergence to the correct result is obtained with fewer k points than in the simple gaussian scheme. We required precision within $3\,meV/atom$ in the bulk total energy of the different phases. We used the following spreading parameters (W, N) and numbers of k points in the Irreducible BZ (IBZ):

i) α-Ga : $N_{\mathbf{k}} = 27\,, N = 0\,, W = 20\,mRy$

ii) β-Ga : $N_{\mathbf{k}} = 250\,, N = 25\,, W = 50\,mRy$

iii) GaII : $N_{\mathbf{k}} = 40\,, N = 10\,, W = 70\,mRy$

iv) GaIII : $N_{\mathbf{k}} = 300\,, N = 5\,, W = 80\,mRy$

v) FCC : $N_{\mathbf{k}} = 203\,, N = 10\,, W = 70\,mRy$

For the calculation of surface energies we evaluated the bulk energy to be subtracted from the total energy of the slab by using a sampling grid in the surface plane identical to that used in the surface calculation, and a grid perpendicular to the surface equivalent

to a slab thickness as close as possible to those used in the surface calculation. A one to one correspondence between the mesh of the bulk and the mesh of the slab is not always possible because in some cases the slabs used are not an integer number of bulk unit cells along the normal to the surface.

Optimization of Structural Parameters: The structure of some phases of gallium is determined by several lattice and internal parameters. In α-Ga for example there are the three lattice parameters a, b, c of the orthorhombic cell, and two internal degrees of freedom which control the bond length and orientation of the Ga_2 dimer. For all the phases studied we found the equilibrium structural parameters which minimize the total energy at each volume, by calculating forces and stress from the self-consistent wave functions by means of Hellman-Feynman (HF) [26] and stress [27] theorems.

At each fixed volume preliminary calculations were performed with different values of the lattice parameters, the number of preliminary calculations for each volume being equal to the number of lattice parameters. For each choice of the lattice parameters the internal degrees of freedom were optimized by relaxing the atomic positions inside the unit cell guided by the HF forces. We then deduced the equilibrium values of the lattice constants for each volume by a linear extrapolation of the anisotropic part of the stress tensor ($\sigma_{xx} - \sigma_{yy}$, and $\sigma_{xx} - \sigma_{zz}$ for α-Ga or $\sigma_{xx} - \sigma_{zz}$ for the tetragonal GaIII for instance. x, y, and z being along the crystallographic axis.). The residual anisotropy in the stress is less than 1 kb for α-Ga and GaIII, and 10 kb for β-Ga which is cumbersome, requiring the optimization of four lattice parameters (a, b, c, $cos(ac)$). The structure near the equilibrium volume has been further optimized also for β-Ga with a residual anisotropy in the stress less than 1 kb. The relaxation of atomic positions at fixed lattice parameters in the bulk and slab calculations was performed using the forces at previous iterations and updating the inverse of the hessian matrix, by following the Broyden-Fletcher-Goldfarb-

Shanoo (BFGS) algorithm [28]. At step n in the atomic relaxation procedure the starting potential in the self-consistent loop was taken equal to the self-consistent potential at step $n-1$ scaled by the ratio of the structure factors at step n and step $n-1$. With this choice of the starting potential the convergence of the self-consistent loop is accelerated in the slab calculations.

Surface Stress Calculation: In the slab calculation the in-plane lattice parameters are fixed to the equilibrium values obtained from the bulk calculation. On the assumption that the deep bulk portion of the slab is stress-free, one can deduce the surface stress tensor from the stress tensor of the full 3D slab supercell as

$$\sigma_{ij}^{surf} = -\partial\gamma/\partial\epsilon_{ij} = \frac{1}{2}\, d\, \sigma_{ij}^{slab} \tag{2.4}$$

where d is the dimension of the supercell along the z direction, and i, j run over the surface coordinates. The surface stress was obtained from eq. 2.4 after some precautions were taken. First, the stress calculated in the bulk from the wave functions through the stress theorem is not zero at the minimum of the energy versus volume curve ($E(V)$) calculated at constant cutoff (E_{cut}). This is a "basis set effect" which occurs because the stress calculated through the stress theorem is computed with the number of plane waves held constant, while the derivatives of the curve $E(V)$ are calculated at constant E_{cut}. The difference between the stress at constant E_{cut} and at constant number of plane waves is called Pulay stress and it is equal to [29]:

$$\sigma_{ij}^{Pulay} = \frac{2N}{3V}\, \partial E/\partial ln E_{cut}\, \delta_{ij} \tag{2.5}$$

where N and V are the number of atoms and the volume of the cell. σ_{Pulay} vanishes when $E_{cut} \to \infty$. With our $E_{cut} = 14Ry$, σ_{Pulay} at the bulk equilibrium volume of α-Ga is 3 kb.

This small value independently confirms the good convergence of our results with respect to E_{cut}. σ_{Pulay} obtained from the bulk calculation was subtracted from σ^{slab} in eq. 2.4. Second, the anisotropic part of the stress in the bulk is not zero if we use the k-points mesh equivalent to the slab geometry instead of the k-points mesh at convergence in the bulk. This residual anisotropic stress ($\Delta\sigma^{bulk}_{k-mesh}$) in the bulk due to this k-points effect is also subtracted from σ^{slab} in eq. 2.4. In conclusion, we take

$$\sigma^{surf}_{ij} = \frac{1}{2}\, d\, [\sigma^{slab} + \frac{N}{V}\Big|_{slab} \frac{V}{N}\Big|_{bulk} (\sigma^{bulk}_{Pulay} - \Delta\sigma^{bulk}_{k-mesh})] \tag{2.6}$$

With these precautions the stress perpendicular to the surface is indeed very close to zero ($\sim$ 0.03 kb). The term $\Delta\sigma^{bulk}_{k-mesh}$ introduces in some cases a large uncertainty in the calculation of surface stress. For instance in the ground state configuration of the (001) surface the component along the [100] direction of the surface stress is -27 and $-5\, mRy/atom$ respectively with and without the "k-mesh correction".

3 Bulk Properties and Phase Diagram of Ga

Gallium is a trivalent metal with an unusual crystal structure in the stable low pressure phase, called α-Ga. The structure is commonly described in terms of the face-centered orthorhombic unit cell with eight atoms per cell reported in figure 3.1 [1].

A peculiar feature is that each atom has only one nearest neighbor at a distance 2.44Å. The second, third and fourth shells each contains two atoms, and are 0.27Å, 0.30Å, and 0.39Å further apart. These six atoms can be seen as lying on a strongly buckled plane, about 1.9Å thick, perpendicular to the [001] direction. Each atom in the strongly buckled planes is pairwise connected by a short bond to the the first neighbor which lie on a neighboring plane. The distance between nearest-neighbor atom pairs is comparatively short for a normal metallic bond, which has led to discussion about the covalent nature of this bond [6]. In the extreme covalent picture the Ga_2 pairs can be seen as dimers, making α-Ga the only elemental solid exhibiting both metallic and "molecular" character at zero pressure. Most molecular solids will in fact turn metallic upon application of a sufficiently large external pressure. For elemental molecular solids, however, it is generally believed that the disappearance of the band gap and subsequent disappearance of the molecular structure are pretty close together, if not downright coincident. A rare known example of metallic molecular solids is represented by the case of crystalline I_2, where the metal-

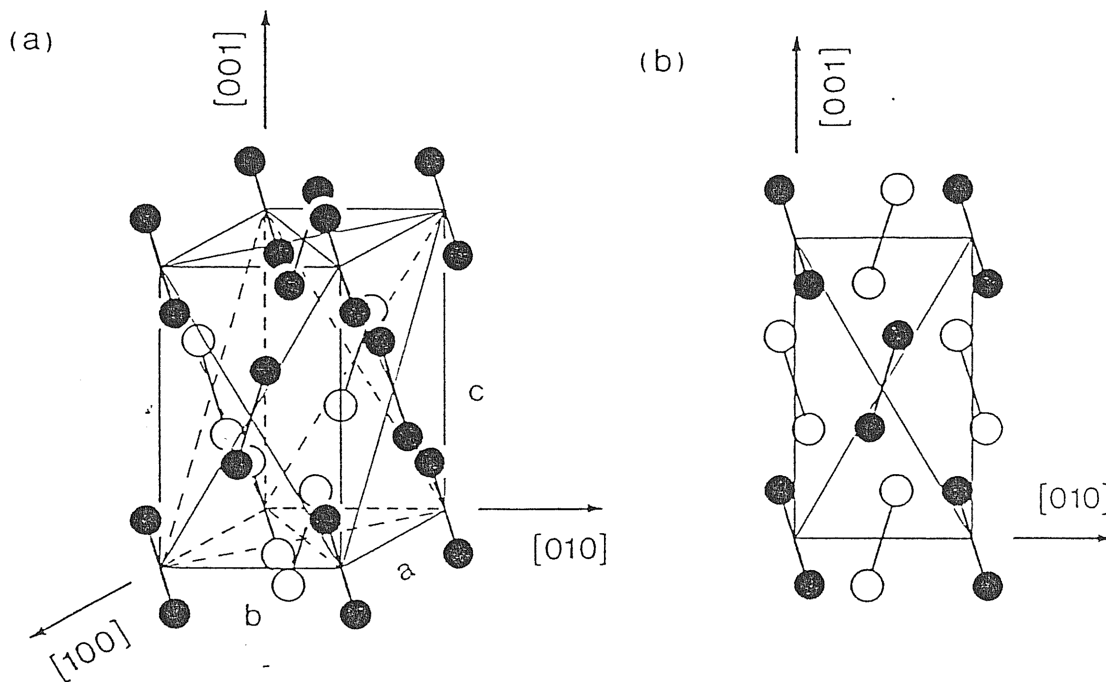

Figure 3.1: a) Face-centered orthorhombic cell of α-Ga. Each site of the cell is occupied by a covalent bonded Ga_2-dimer. b) Side view on the (100) plane (solid circles) and on the next lower plane (open circles) at a depth of $a/2 = 2.25$Å. The dimer axis lies within the (100) plane.

nonmetal transition occurs at a pressure lower than that required to induce molecular dissociation [30].

Several physical properties further substantiate the partial covalent character of α-Ga. The thermal and electrical conductivities are highly anisotropic ($\sigma_c : \sigma_b : \sigma_a = 1 : 2.3 : 6.7$, for electrical conductivities), being lowest along the [001] direction, which is close to the direction of the presumed Ga_2 dimers [31] [1]. In liquid Ga, instead, these conductivities are about a factor of 2 higher than the corresponding value along the c axis of the crystal. Similar behavior is found in most semimetals (Sb,Bi,Te) and is especially striking in semiconductors (Si,Ge), whose constituents are unequivocally covalently bonded [32], while the melt is metallic. As in covalent semiconductors (Si, Ge), the density of gallium in the liquid phase is higher than in the crystalline phase: the corresponding change in specific volume is about 3.2 % [32]. Moreover the low temperature structure factor (S(k)) of liquid Ga exhibits also some covalent features similar to those of Si and Ge, in particular a shoulder of S(k) at about 3 Å^{-1}, which lies on the high momentum side of the first and main peak [33]. No such shoulder is found instead in the isoelectronic liquid metals Al, In, and Tl [33], which do not posses a stable covalent phase.

Further indications of the covalent character of Ga comes from measurements of electronic properties. Optical reflectivity spectra contain a sharp peak at a photon energy of 2.3 eV [34, 35], similar in shape to the bonding-antibonding transition in semiconductors. In a photoemission experiment on polycrystalline Ga, the electronic density-of-states (DOS), derived from the photoelectron yield spectra, shows a broad maximum 1.2 eV below the Fermi level (E_f) and an unusually steep decrease towards E_f [36], indicative of a pseudogap. The presence of a pseudogap in the DOS at E_f is also suggested by the

[1] It should be noted that contrary to the case of α-Ga, the metallic "molecular" I_2 has the largest conductivity in the direction of the I_2 bonds.

anomalous low value of the measured Knight shift [37]. A strong bond between nearest neighbor is also in accordance with the phonon band structure deduced from neutron scattering data in ref. [38]. The flat phonon branches around $7Thz$, separated by a $1Thz$ gap from the other branches, can be associated to dimer stretching. Conversely in the fully metallic β-Ga phase for example, the corresponding feature in the phonon density of states is absent [39].

Theoretically, the covalent character was suggested by interpretations of the band structure calculations based on empirical pseudopotentials [6, 34, 40]. The highest occupied and lowest unoccupied Σ-bands along the [001] direction have remarkably low dispersion and are symmetric about E_f. Although the band structure of α-Ga is rather complicated, the calculated shape of most parts of the Fermi-surface are in good agreement with experimental data. A compilation can be found in ref. [40]. Further refinements of the Fermi surface come from newer de Haas-van Alphen measurement [41].

The recent *ab initio* calculation, based on LDA and pseudopotentials, by Gong *et al* [8] fully confirmed the presence of the covalent bond between each Ga_2 pair in α-Ga. They found a pronounced pseudogap in the electronic DOS at E_f, and a good agreement between theoretical prediction and experimental data on electronic band structure and optical conductivity. Moreover Gong *et al* [42] performed an *ab initio* simulation of liquid Ga at high temperature (1000 K). Their results reproduced the faint shoulder in the structure factor S(k) observed experimentally at k$\sim$ 3Å^{-1}in this temperature range. The electron DOS of the liquid turns out in their calculation to resemble much more β-Ga than α-Ga. In particular, the pseudogap at E_f characteristic of α-Ga DOS is absent in the high temperature liquid phase. This result explains the regular (large) Knight shift of liquid Ga [46] and the fact that its value is so close to that of β-Ga. However in the liquid phase the metallic and covalent characters still coexist. Covalency manifest itself

in the appearance in the simulation of very short-lived Ga-Ga bonds, which represent the remnants in the liquid of the dimers in crystalline α-Ga.

In the following we present our new results on the electronic and structural properties of α-Ga and of other known phases. They were done at zero temperature, with the improved technique discussed in the previous chapter. In particular, unlike the previous work by Gong *et al*, where only the Γ point in a 72-atoms supercell was included in the k-sums, we used a high accuracy BZ integration scheme. Pseudopotential, XC energy functional and plane waves expansion are the same as in ref. [8]. In addition we have also optimized all the lattice parameters, whose ratios were instead fixed to the experimental values in ref. [8]. It turns out that, while the overall structure and electronic properties of α-Ga suffer minor changes with respect to the results in ref. [8], the hierarchy in energy of the losing structures, and consequently the pressure induced phase transition, are largely modified by our improved calculation.

3.1 Structural Properties

The structure of α-Ga is shown in fig. 3.1. Each atom and its first neighbor are depicted as a dimer. The bond length and orientation of the dimer are controlled by two internal degrees of freedom: u and v. The structure is thus determined by five parameters: $a, b/a, c/a, u, v$. The positions of the eight atoms in the orthorhombic unit cell (two times larger than the primitive unit cell) as a function of u and v are [1]

$$\begin{array}{cccc} (0,u,v) & (\tfrac{1}{2},u,\tfrac{1}{2}+v) & (\frac{1}{2},\frac{1}{2}+u,-v) & (0,\frac{1}{2}+u,\frac{1}{2}-v) \\ (0,-u,-v) & (\tfrac{1}{2},-u,\tfrac{1}{2}-v) & (\frac{1}{2},\frac{1}{2}-u,v) & (0,\frac{1}{2}-u,\frac{1}{2}+v) \end{array} \tag{3.1}$$

with $u = 0.0785$, and $v = 0.1525$ (x, y, z, are intended to be multiplied by a, b, c respectively). The experimental values of the lattice parameters are reported in table 3.1.

Two other phases are stable at high pressure: GaII and GaIII. GaII is body-centered cubic with six atoms in the unit cell. Their coordinates in unit of a are [2]

$$\begin{array}{ccc} (3/8,0,1/4) & (1/4,3/8,0) & (0,1/4,3/8) \\ (1/8,0,3/4) & (3/4,1/8,0) & (0,3/4,1/8) \end{array} \tag{3.2}$$

Each atom has eight nearest neighbors in the GaII structure. GaIII is face centered tetragonal [2] similar in structure to indium, it has only two structural parameters: $a, c/a$. The experimental lattice parameters of GaII and GaIII are reported in table 3.1. The phase diagram of gallium displaying the stability regions of α-Ga, GaII, and GaIII along with the metastability lines of the phases $\beta, \gamma, \delta, \epsilon$, is reported in figure 3.2 [2].

β-Ga is a metastable phase obtained by supercooling the liquid [3], or by heating amorphous-Ga [43], obtained in turn by deposition of the vapour onto a cold substrate [44]. β-Ga is C-centred monoclinic, space group C_{2h}^6 (C2/c). The four atoms in the conventional monoclinic unit cell (figure 3.3) are at $\pm(0, y, \frac{1}{4})$ and at $(\frac{1}{2}, \frac{1}{2}, 0) \pm (0, y, \frac{1}{4})$ with $y = 0.131$ at $248\,K$ [3]. The primitive unit cell contains the two atoms at $\pm(0, y, \frac{1}{4})$. The nearest neighbors atoms form zig-zag chains along the [001] direction as shown in fig. 3.3. The experimental values of the lattice parameters are reported in table 3.1.

The metastable phases δ [5], and γ [4] whose unit cells contain 40 and 22 atoms respectively, and the phase ϵ, whose structure has not yet been determined, are not considered here any further.

Bosio [2] pointed out that GaIII may be prepared in a metastable state below the

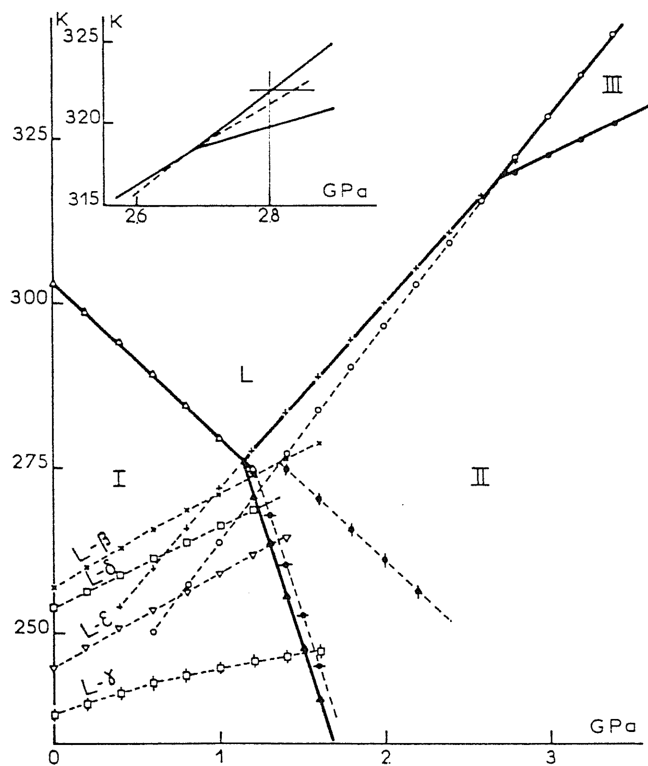

Figure 3.2: Equilibrium phase diagram of gallium taken from ref. [2]. The inset shows the liquid-GaII-GaIII triple point. The dotted lines represent the metastable equilibrium phase boundaries. GaI refers to α-Ga.

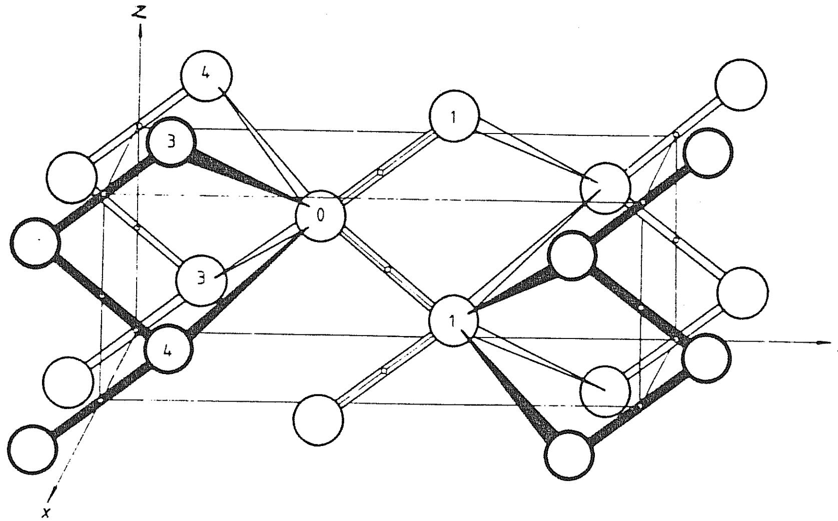

Figure 3.3: The crystal structure of β-Ga. The angle between the positive x and z axis is $\beta > 90^o$. The first, third and fourth nearest neighbours of a particular atom (labelled 0) are indicated. The second nearest neighbours are at $\pm(a, 0, 0)$. The figure is taken from ref. [3].

liquid-α-GaII triple point by compressing or cooling the liquid, and at 4 GPa, GaIII may be supercooled by as much as 80-100 K before it transforms to GaII. In previous studies [10, 45] of the crystal structure of Ga at high pressure these metastability phenomena were not considered and so the phase GaII in fig. 3.2 was erroneously identified with the face-centered tetragonal structure of GaIII. Following these older results Gong *et al* [8] studied the pressure induced phase transition α-Ga $\rightarrow$ GaIII (named GaII there) and ignored instead the true structure of GaII discovered by Bosio [2].

In figure 3.4 we report the energy versus volume per atom of the various phases. The points were obtained by allowing a full relaxation of atomic positions inside the unit cell and by optimizing the lattice constants at each volume by using the calculated stress tensor as discussed in chapter 2. The zero point vibrational energy is neglected. The points have been interpolated with a Murnaghan's equation of state [47],

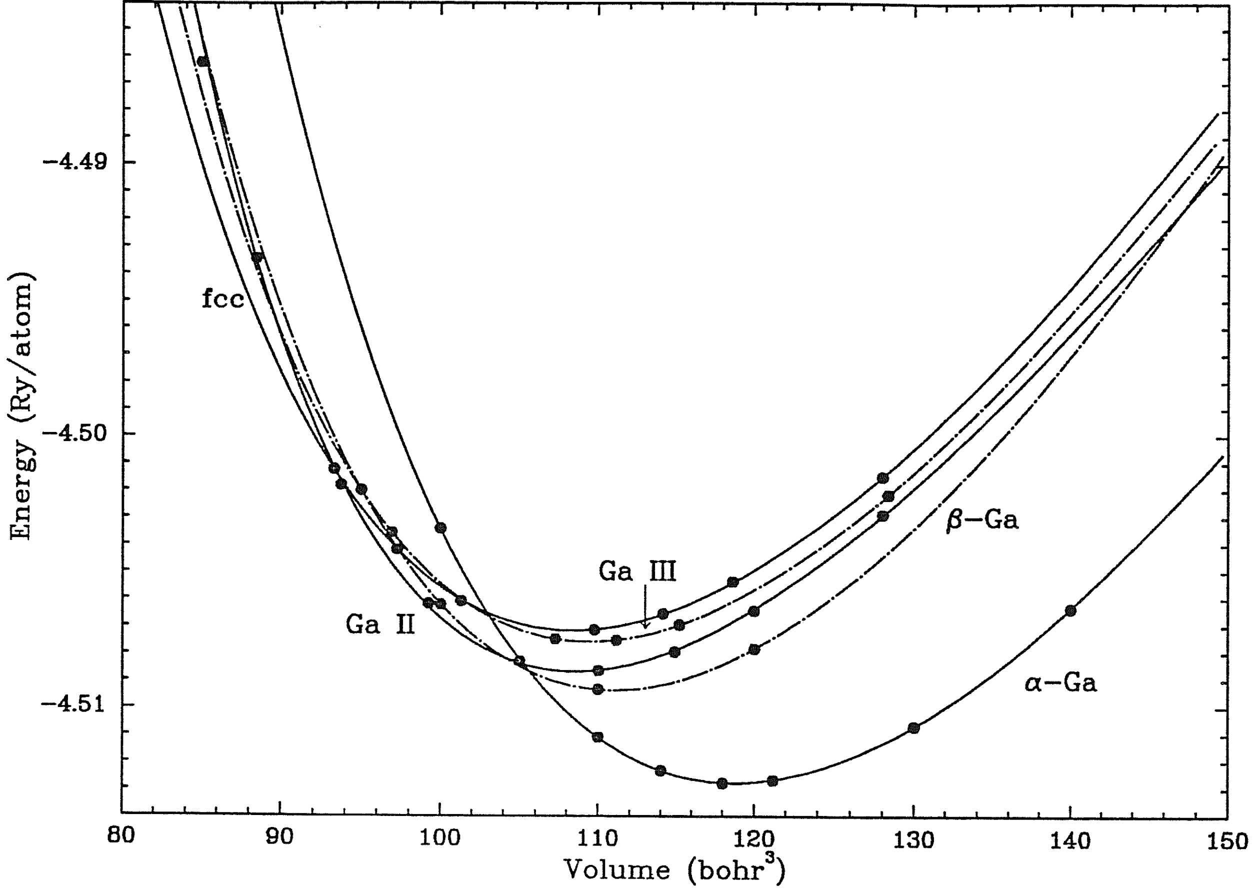

Figure 3.4: Equation of state of five phases of gallium. The zero point vibrational energy is neglected.

$$E_{tot}(V) = \frac{B_o V}{B_o'}\left[\frac{(V_o/V)^{B_o'}}{B_o'-1} + 1\right] + const \tag{3.3}$$

where B_o and B_o' are the bulk modulus and its pressure derivative at the equilibrium volume V_o. The theoretical lattice parameters at V_o are compared with the experimental data in table 3.1. The theoretical internal degrees of freedom at equilibrium for α-Ga are $u = 0.0803, v = 0.1567$ (exp. $u = 0.0785, v = 0.1525$ [1]), while the internal parameter y in β-Ga is $y = 0.134$ (exp. $y = 0.131$, [3]). The theoretical B_o and B_o' are reported in table 3.2. The experimental bulk modulus is known only for α-Ga and it is equal to $B_o^{exp} = 613\ kb$ at 4.2 K and atmospheric pressure [48]. The agreement with the theoretical value (669 kb) is remarkably good.

phase	Theory				Exp.			
	a	b/a	c/a	Vol.	a	b/a	c/a	Vol.
α	8.271	0.994	1.688	119	8.523	1.0013	1.695	131
β	4.954	2.973	1.218	111	5.227	2.911	1.205	125
GaII	10.921			109	11.246			119
GaIII	7.092		1.227	109	7.518		1.119	119
fcc	7.568			108				

Table 3.1: Theoretical and experimental lattice constants in a.u. of different phases of gallium. The experimental data are taken from ref. [1] for α-Ga (4.2 K, and atmospheric pressure), from ref. [2] for GaII (at 313 K and 2.6 GPa), from ref. [2] for GaIII (at 298 K and 2.8 GPa), and from ref. [3] for β-Ga (at 248 K and atmospheric pressure). The small deviation from orthorhombic symmetry in β-Ga is accounted for by the angle β between a and c axis. We obtained $\beta = 92.45^o$, while experimentally $\beta = 92.03^o$.

	α	β	GaII	GaIII	fcc
B_o (kb)	669	709	706	652	629
B'_o	4.683	4.265	6.217	4.725	4.466

Table 3.2: Theoretical bulk modulus (B_o) in kb and its pressure derivative (B'_o) at the equilibrium volume for the different phases. The experimental bulk modulus is known only for α-Ga and it is equal to $B_o^{exp} = 613\, kb$ at 4.2 K and atmospheric pressure [48].

	α	β	GaII	GaIII	fcc
$Energy/atom$ (Ry)	-4.5128	-4.5094	-4.5087	-4.5076	-4.5072

Table 3.3: Energy per atom (Ry/atom) at the equilibrium volume of the different phases.

The theoretical lattice parameter a is 3 % smaller than the experimental one for all phases. The other structural parameters of α-Ga and β-Ga are in excellent agreement with experimental data (error $< 2\,\%$). However, in GaIII the c/a parameter has a larger deviation (9 %). At 100 kb the theoretical c/a of GaIII is 1.202, still larger than the experimental value (cfr. table 3.1).

Figures 3.5a-c report the dependence of b/a, c/a, and of the dimer bond length (d_{dimer}) on the volume of α-Ga. Both b/a and c/a increases with pressure. The line in fig. 3.5c represents the ideal scaling of the dimer bond length, i.e $d_{dimer} \sim 0.929 V^{\frac{1}{3}}$, where 0.929 is the ratio $d_{dimer}/V_o^{\frac{1}{3}}$ at equilibrium. This line interpolate rather well our results, indicating that the Ga-Ga distance in the dimer varies with the volume as the average Ga-Ga distance. In the previous work by Gong *et al* [8] the slope of the straight line interpolating their results was 20 % lower than the ideal value, but there the ratio of the lattice parameters were fixed at the experimental value and not allowed to vary with pressure. Actually the c/a, and b/a ratios have a non-negligible variation with volume as reported in figs. 3.5a-b.

Note that the energy minimum of all phases (table 3.3) lie within a narrow energy window, $6\,mRy/atom$ large. Although the α-Ga structure had been found as the stable phase also in older calculations within pseudopotential perturbation theory [6, 7, 49], the exact hierarchy in energy of the other phases, and the related pressure induced phase transitions, differ widely in different works, depending on the choice of pseudopotentials and dielectric functions. In our calculation the phase closest to α-Ga is β-Ga as we would expect from the wide metastability region of the latter phase and from its high melting temperature ($T_m(\beta) = 257K$, while $T_m(\alpha) = 303K$, $T_m(\alpha) - T_m(\beta) = 0.3\,mRy$). Moreover the density of β-Ga, being 7% higher than those of α-Ga at equilibrium, is closer to that of liquid gallium, consistently with the easy growth of β-Ga from the supercooled liquid.

The phase reached by α-Ga under hydrostatic pressure is GaII, in agreement with

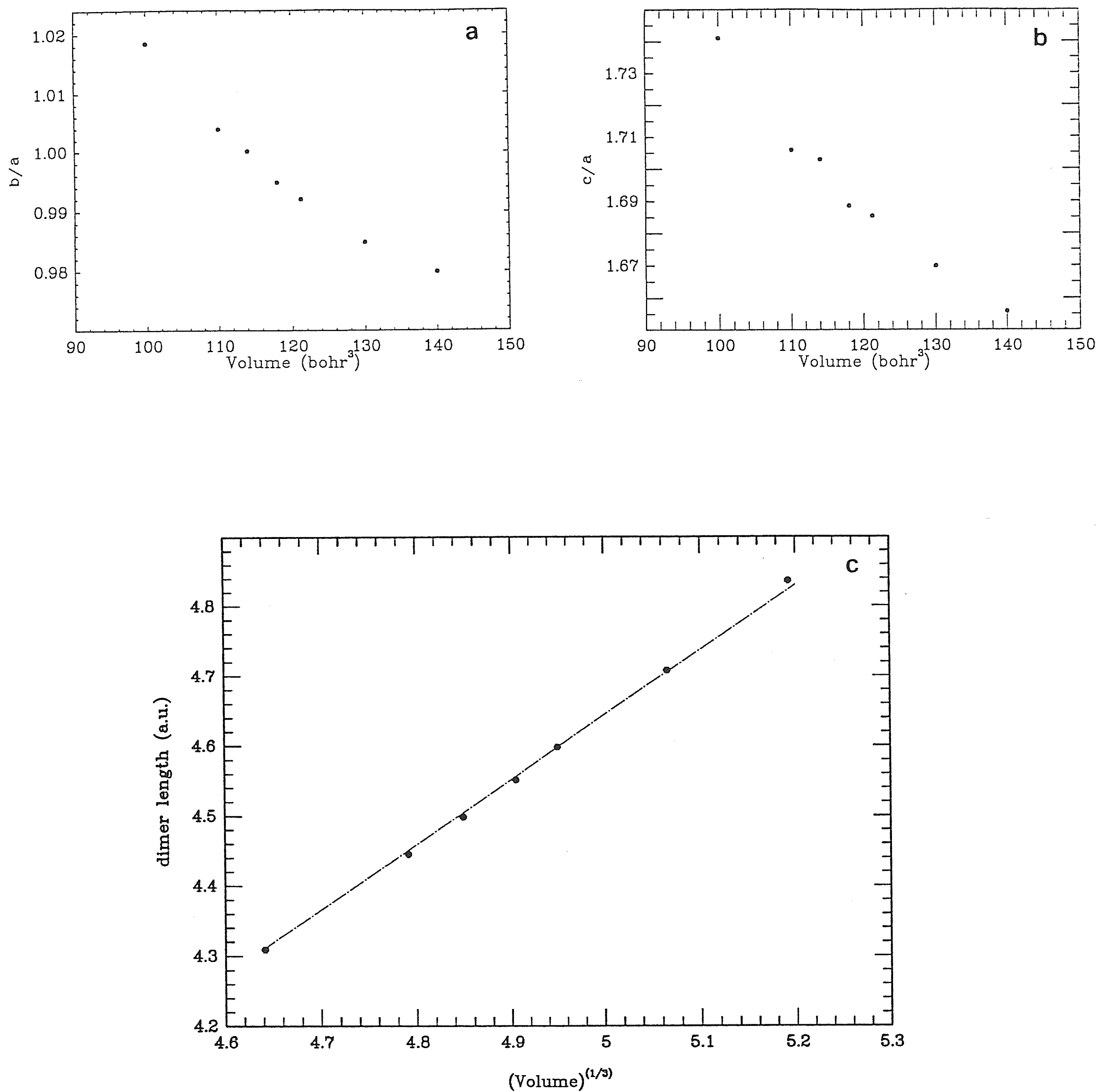

Figure 3.5: Dependence on the volume in α-Ga of the structural parameters a) b/a, b) c/a, and c) the dimer bond length. In figure c) the dotted line corresponds to the "ideal" bond length obtained from the bond length at equilibrium just by scaling it by $V^{\frac{1}{3}}$. Its slope is 0.929, equal to $d_{dimer}/V_o^{\frac{1}{3}}$ at the equilibrium volume.

experimental evidence [2]. Our theoretical transition pressure is $P_{\alpha-GaII} = 64\,kb$. The experimental transition pressure at $T = 0K$ can be obtained by extrapolating the α-Ga/GaII coexistence line in fig. 3.2. A linear extrapolation down to zero temperature gives an upper bound of 48 kb. A better estimate could be obtained by taking the linear extrapolation up to about one fifth of the Debye temperature (240 K), giving 41 kb. This value still compares reasonably well with our theoretical result.

At higher pressure, a new phase transition from GaII to fcc is predicted at 152 kb. As far as we know this region of pressure has not yet been explored experimentally. Thus we propose that the phase diagram in fig. 3.2 should be enriched with the new coexistence line GaII-fcc, which should continue also in the GaIII region as a GaIII-fcc coexistence line. In facts in our calculation GaIII turns out to be mechanically unstable for pressure higher than 250 kb. For fixed equilibrium volume higher than 87 a.u. (pressure lower than 250 kb) the energy per atom as a function of the ratio c/a has two minima: one at $c/a = 1$ corresponding to ideal fcc, and the other for c/a in the range $1.2 - 1.26$ corresponding to GaIII. For volume higher than 101 a.u. the minimum corresponding at GaIII is deeper (GaIII has lower energy than fcc, see fig. 3.4), while for volume lower than 101 a.u. the situation is reversed with the GaIII minimum more and more shallow as pressure increases. Finally for volumes less than 87 a.u (P > 250 kb) the minimum in the $E = E(c/a)$ curve corresponding to GaIII disappers, and only the minimum at $c/a = 1$ (fcc) survives, therefore indicating that GaIII is mechanically unstable in this range of pressure.

The theoretical equilibrium volume is about 9% lower than the experimental one for all phases (cfr. table 3.1). While a certain tendency to overestimate the atomic density is common to most LDA calculations, this error is somewhat larger than usual. In order to estimate if our neglect of the core charges plays a role in this misfit, we

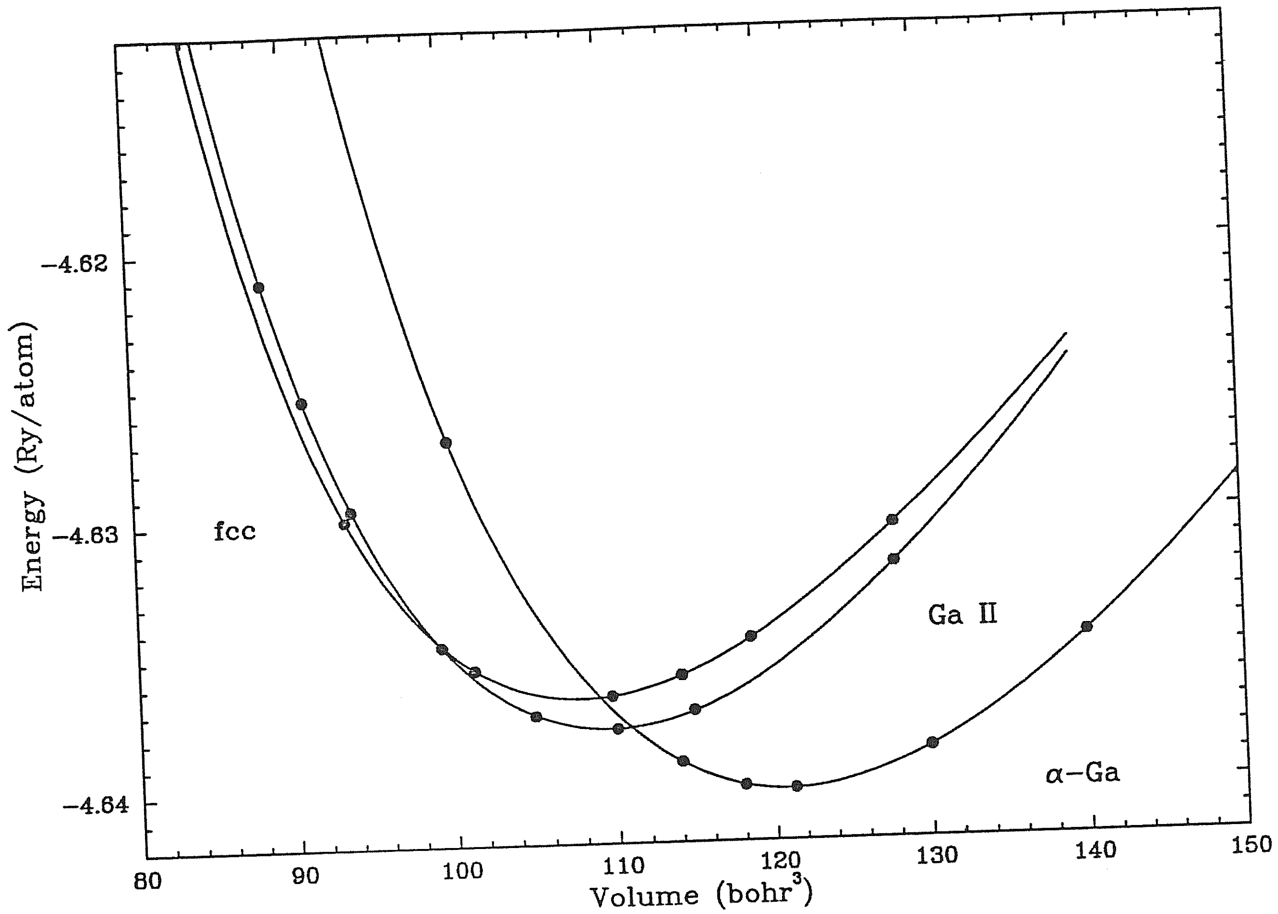

Figure 3.6: Total energy curves for α-Ga, GaII, and fcc with a NLCC-pseudopotential.

re-computed the equation of state for α-Ga, GaII, and fcc with a new pseudopotential including the Non-Linear-Core-Correction (NLCC). The details of the derivation of the NLCC-pseudopotential are reported in appendix A. The new $E(V)$ curves and lattice parameters are reported in fig. 3.6 and table 3.4.

From table 3.4 we can see that the NLCC does not improve the misfit in the equilibrium

phase	Theoret. lattice parameters with NLCC					
	a	b/a	c/a	Vol.	u	v
α	8.374	1.0013	1.695	121	0.0814	0.1573
GaII	10.95			110		
fcc	7.556			108		

Table 3.4: Structural parameters in a.u. of α-Ga, GaII, and fcc at the equilibrium volume calculated with a NLCC-pseudopotential.

volumes. The other structural parameters are only slightly modified by the change of the pseudopotential except for the transition pressures which undergo large variations. $P_{\alpha-GaII}$ is now 34 kb (64 kb without NLCC), and $P_{GaII-fcc}$=93 kb (152 kb without NLCC). These variations are indeed very large, and mainly due to the change in the relative energies of the three phases (cfr. figs. 3.4 and 3.6). However we remark that the quality of our NLCC-pseudopotential in appendix A is worse than the pseudopotential without NLCC by Stumpf *et al* [18]: the deviation of the atomic pseudo-orbitals from the all-electron orbitals outside the core radius is larger for our NLCC-pseudopotential (see fig. A.1). Nevertheless the mean message of our NLCC results is that the neglection of NLCC is not the source of the error in the equilibrium volumes. This misfit is more likely a failure of the LDA which is well known to overbind molecules. The properties of the Ga_2 molecule have been recently studied by Jones [50] in LDA with the pseudopotential of ref. [18]. The LDA interatomic distance of the molecule in the electronic ground state $^3\Sigma_u$ is 4.864 a.u.. The experimental interatomic distance is not known, but the LDA value is indeed 7% smaller than the value obtained with an all-electron quantum chemistry calculation (Complete active space SCF followed by second order configurations interactions) [51]. The quantum-chemistry calculation of ref. [51] is actually not a full CI, and the LDA vibrational frequency is 184 cm^{-1}, closer to the experimental result (184 cm^{-1}) than the quantum-chemistry value (154 cm^{-1}). Thus the accuracy of LDA for Ga_2 molecule is unclear, and should be further investigated, by comparison with more accurate quantum-chemistry calculation. Also the role of core-core interaction/relaxation should be studied through an all-electron LDA calculation on Ga_2 molecule.

3.2 Electronic Properties

Our analysis of the electronic properties of α-Ga shows very clearly the long standing proposed covalency of the bond between each Ga pair and its fingerprint in the electronic density of states consisting of a pronounced pseudogap at the Fermi level. The electron (pseudo)charge density of α-Ga is compared to those of the other phases of gallium in fig. 3.7.

The "molecular" Ga_2 bonding in α-Ga is visible as a pile up of charge in the center of the dimer. Conversely in all the other phases the distribution of charge is atomic-like with a maximum of charge near each atom and not midway between the atom and its nearest neighbors. The maximum of (pseudo)charge density in the dimer covalent bond is ~ 0.058 a.u., comparable to the corresponding value in the covalent bond of germanium which is 0.0742 a.u. [54]. We can roughly compare the number of electrons participating in the covalent bond of α-Ga and Ge, by multiplying the maximum of the bonding charge by the bond length cubed. In this crude approximation we find in the α-Ga bonding charge $\sim$0.25 electrons less than in Ge, that is 1.5 electrons per bond charge in α-Ga assuming 2 electrons per bond charge in Ge.

The partial covalent character of α-Ga and the fully metallic nature of the other phases show up in the electronic Density Of States (DOS) in fig. 3.8. The electronic bands along some high symmetry lines in the IBZ of the different phases are reported in figs. 3.9- 3.13. The DOS of α-Ga is rather structured and shows a pronounced pseudogap at the Fermi level, in agreement with photoemission study [36]. The α-Ga DOS in fig. 3.8 is very similar to those reported in refs. [8, 9]. The connection between the pseudo-gap and covalency in α-Ga was discussed long ago by Heine [6]. The residual states in the pseudo-gap are mainly related to the overlap of the electronic wave functions along the buckled planes

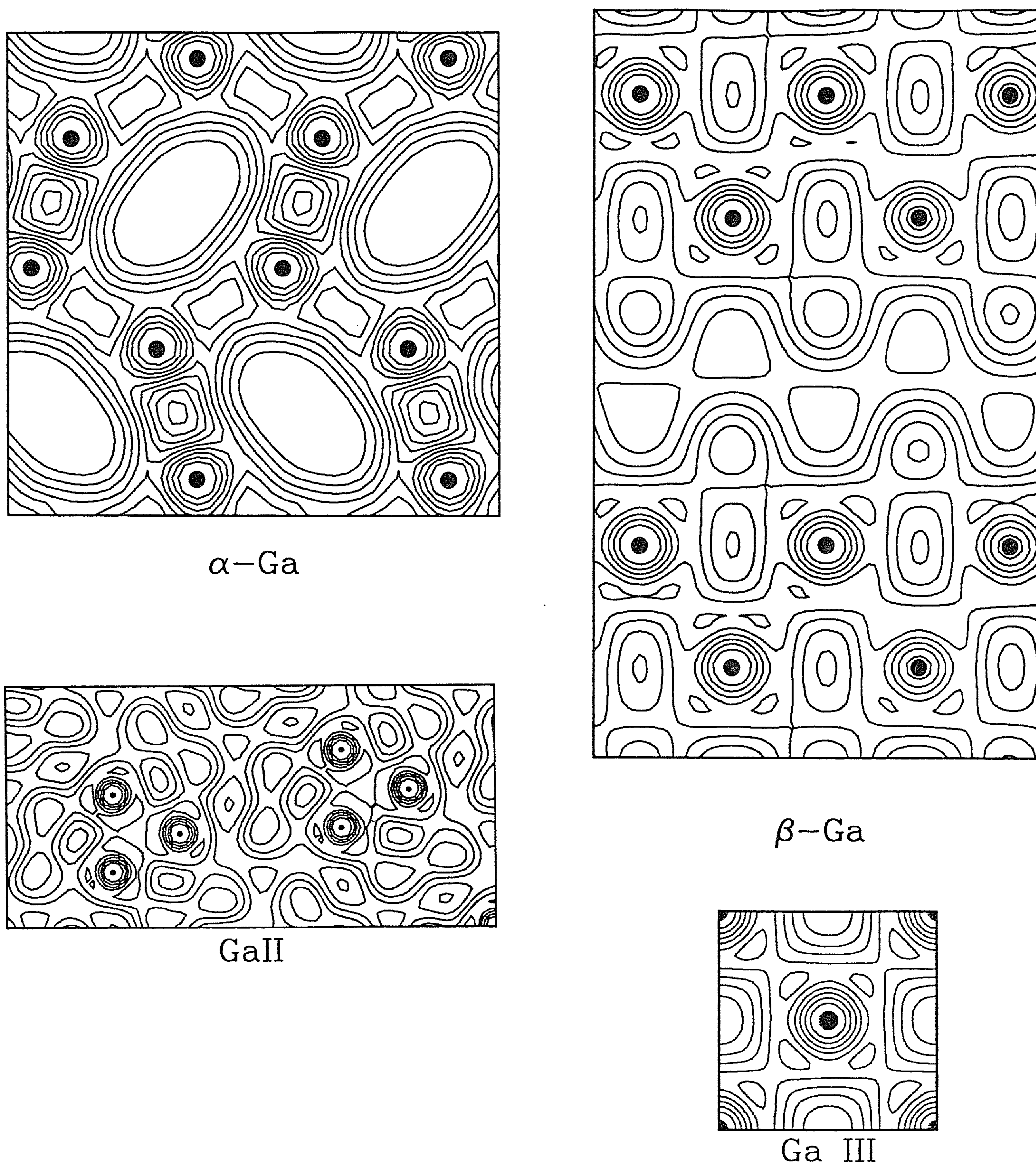

Figure 3.7: Electron (pseudo)charge density map of the different phases of gallium computed at the equilibrium volume of each phase. The contour lines are separated by 0.005 a.u.. α-Ga and β-Ga charge densities are plotted on the (100) plane. GaIII charge density is plotted on the (001) plane. GaII charge density is plotted on the plane passing through the atoms of the trimers shown. The scale is half those of the other pictures. The trimers correspond to one atom and other two atoms among its eight first neighbors.

perpendicular to the "molecular" bond. These states lead to metallic behavior, which thus coexists with the molecular state. S-like states, localized in the buckled planes are also the main contribution to the density of states from the bottom of the valence bands ($\sim$ -12 eV) up to -6.5 eV below the Fermi level. The flexibility of simultaneously forming two kinds of chemical bonds greatly contributes to the stability of this structure. The fact that the states in the gap are related to the in-plane electron motion is also suggested by the band structure of fig. 3.9.

Our α-Ga band structure is very close to that previously obtained by Gong *et al* [8]. The strong anisotropy at the Fermi surface indicates preferential conduction along the (001) planes in agreement with experiments. Details of the electronic structure at the Fermi level [40, 41], such as the small hole pocket in the T direction are well brought out. Note the presence of roughly parallel bonding-antibonding bands nearly symmetric with respect to the Fermi level, typical of covalent materials. Gong *et al* have shown that the gap ($\sim$ 2.3 eV) between these parallel bands, indicated by the arrows in fig. 3.9, gives rise to a strong peak in the optical conductivity. This is a rather unusual feature for a metallic system, and in fact reflects directly the bonding $\rightarrow$ antibonding transition of the Ga_2 covalent "molecule". The antibonding character of the states which mostly contribute to the peak in the DOS just above E_F, is confirmed by direct inspection of our KS orbitals. The agreement between the experimental $\sigma(\omega)$ [34, 35] and that calculated in ref. [8] is remarkably good (cfr. fig. 4 in ref. [8]), indicating that the LDA first principle theory correctly reproduces the electronic properties of α-Ga, down to a very considerable detail.

Coming now to the other phases we note that GaIII, β-Ga and fcc-Ga have a very similar DOS, nearly free-electron like in the low energy range, and with a large value at the Fermi level, consistently with their good metallic properties. In particular, since GaIII is a tetragonally distorted fcc, its electronic densities and bands are very similar to those

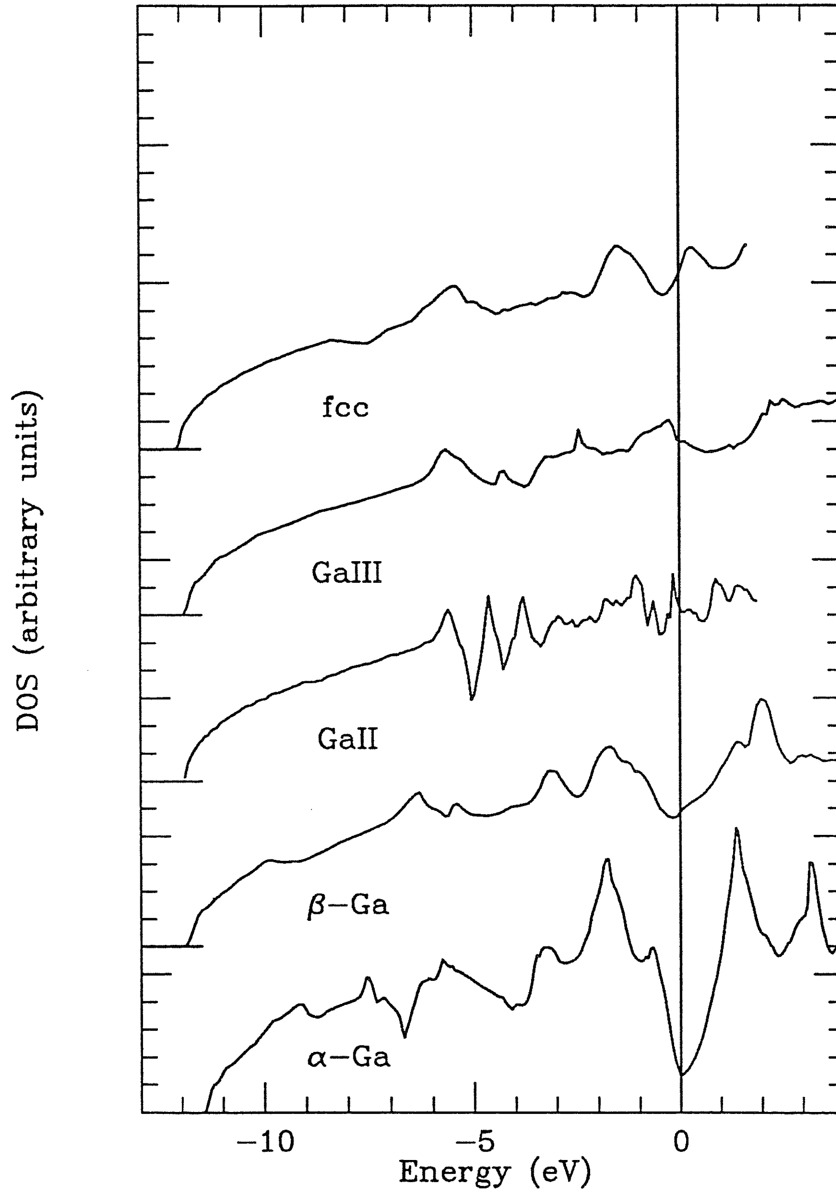

Figure 3.8: Electronic density of states of the different phases of gallium. They have been computed at the equilibrium volume of each phase by using a uniform mesh in the IBZ including up to 300 k points. The tetrahedron linear analytic interpolating method has been used [65].

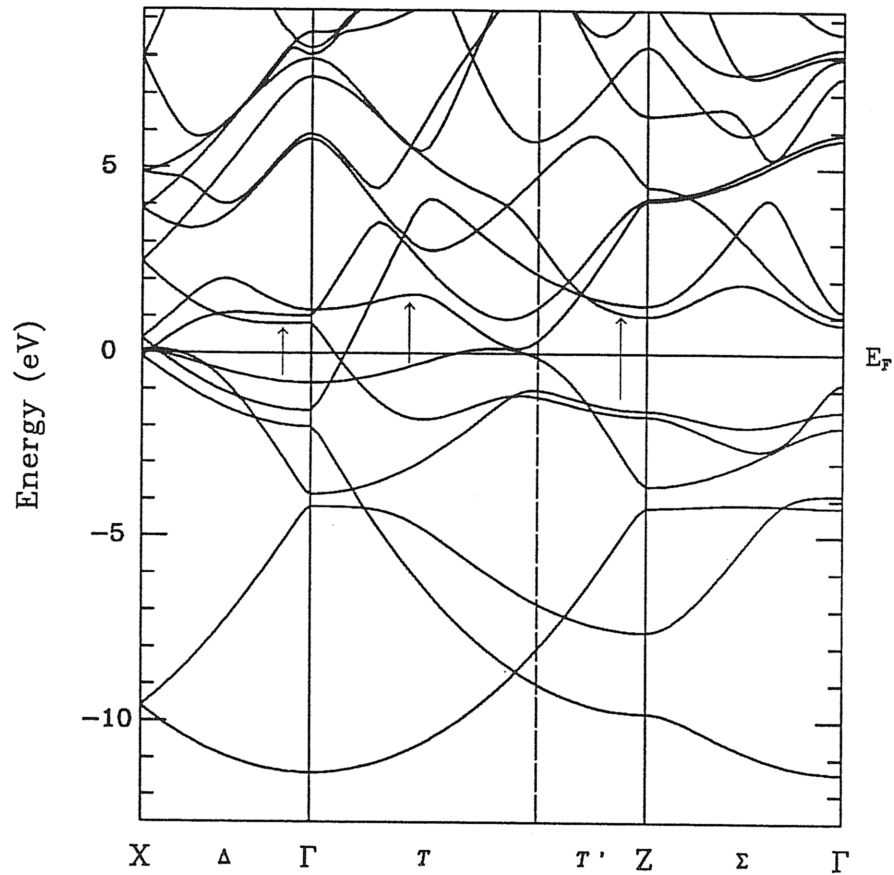

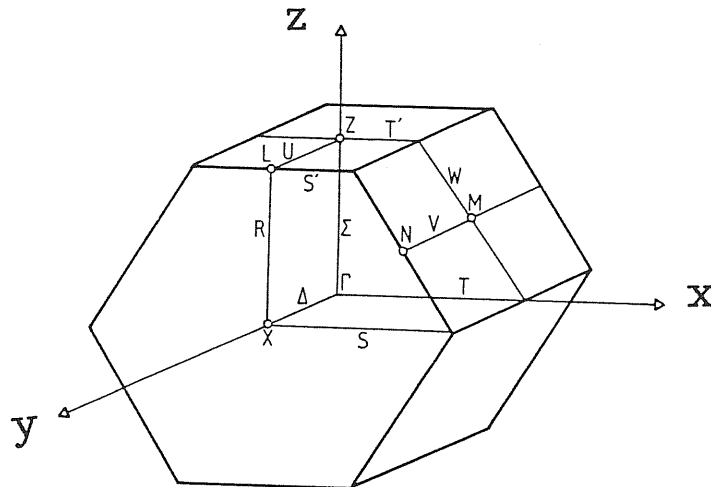

Figure 3.9: The band structure of α-Ga along some high symmetry lines in the Brillouin Zone. Arrows denote important molecular bonding-antibonding optical transitions.

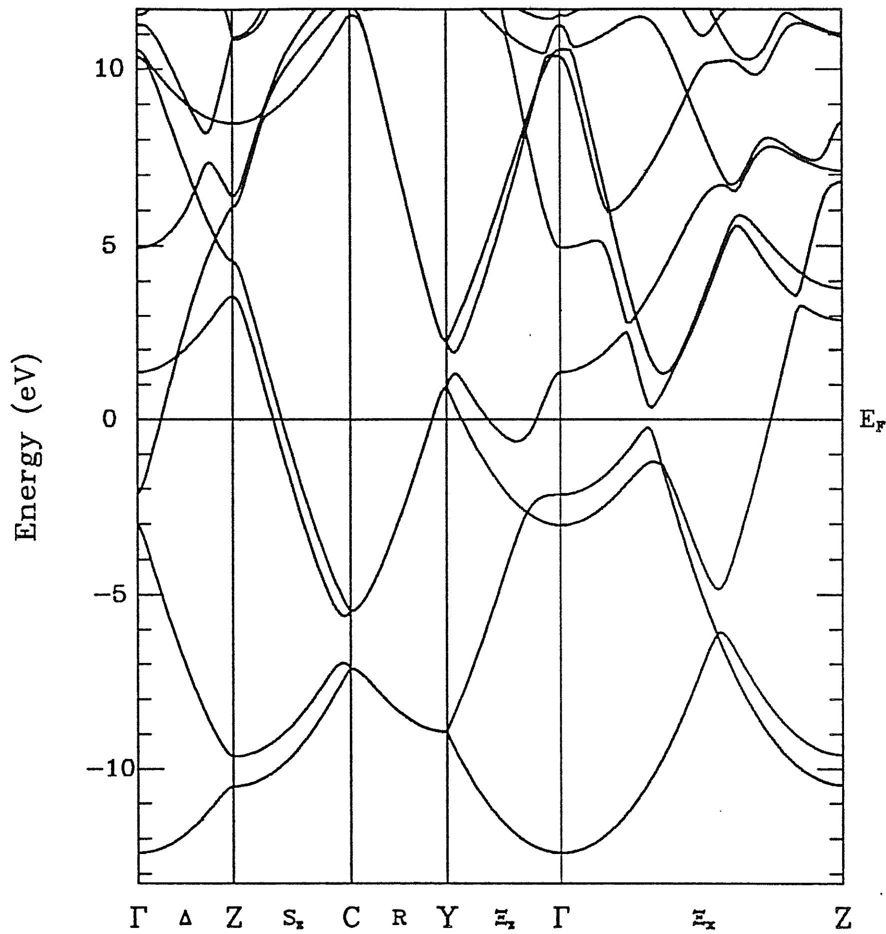

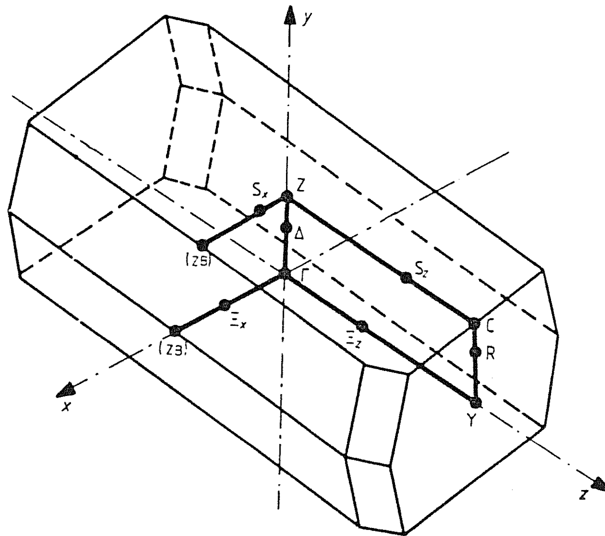

Figure 3.10: The band structure of β-Ga along some high symmetry lines in the Brillouin Zone. The figure of the Brillouin Zone is taken from ref. [39]. In the figure of the Brillouin Zone the scales in the three directions have been modified to clarify the view, and the difference between β and 90° has been exaggerated.

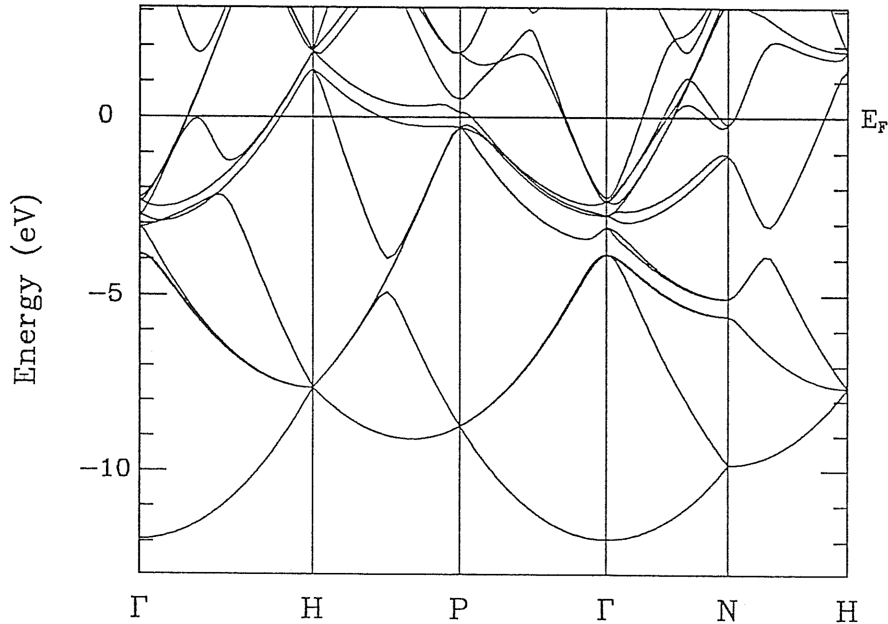

Figure 3.11: The band structure of GaII along some high symmetry lines in the bcc Brillouin Zone. Points are labelled following Zak [52].

of fcc-Ga. Conversely the phase GaII still presents some structures in the DOS around 4-5 eV below the Fermi level.

The difference between the DOS at the Fermi level ($D(E_F)$) of α-Ga and β-Ga is experimentally reflected in the Knight Shift, which in β-Ga is about 3 times larger than in α-Ga [37]. We obtained a ratio of about 3.5 between the calculated values of $D(E_F)$. Although we have not attempted to estimate the relative values of $|\Psi(0)|^2$ between α-Ga and β-Ga, the pseudocharge densities near the s core radius (r_s=1.72 a.u.) are not unlike, which suggests that the difference in $D(E_F)$ is indeed the main factor.

Finally we recall that Gong *et al.*, in order to suggest some direct method to detect the covalent bond, compared in ref. [8] the electronic structure factor calculated in two different ways: the first [$S_c(k)$] using the true electronic charge density and the second [$S_a(k)$] using a superposition of atomic charges. $S_c(k)$ and $S_a(k)$ show a similar overall

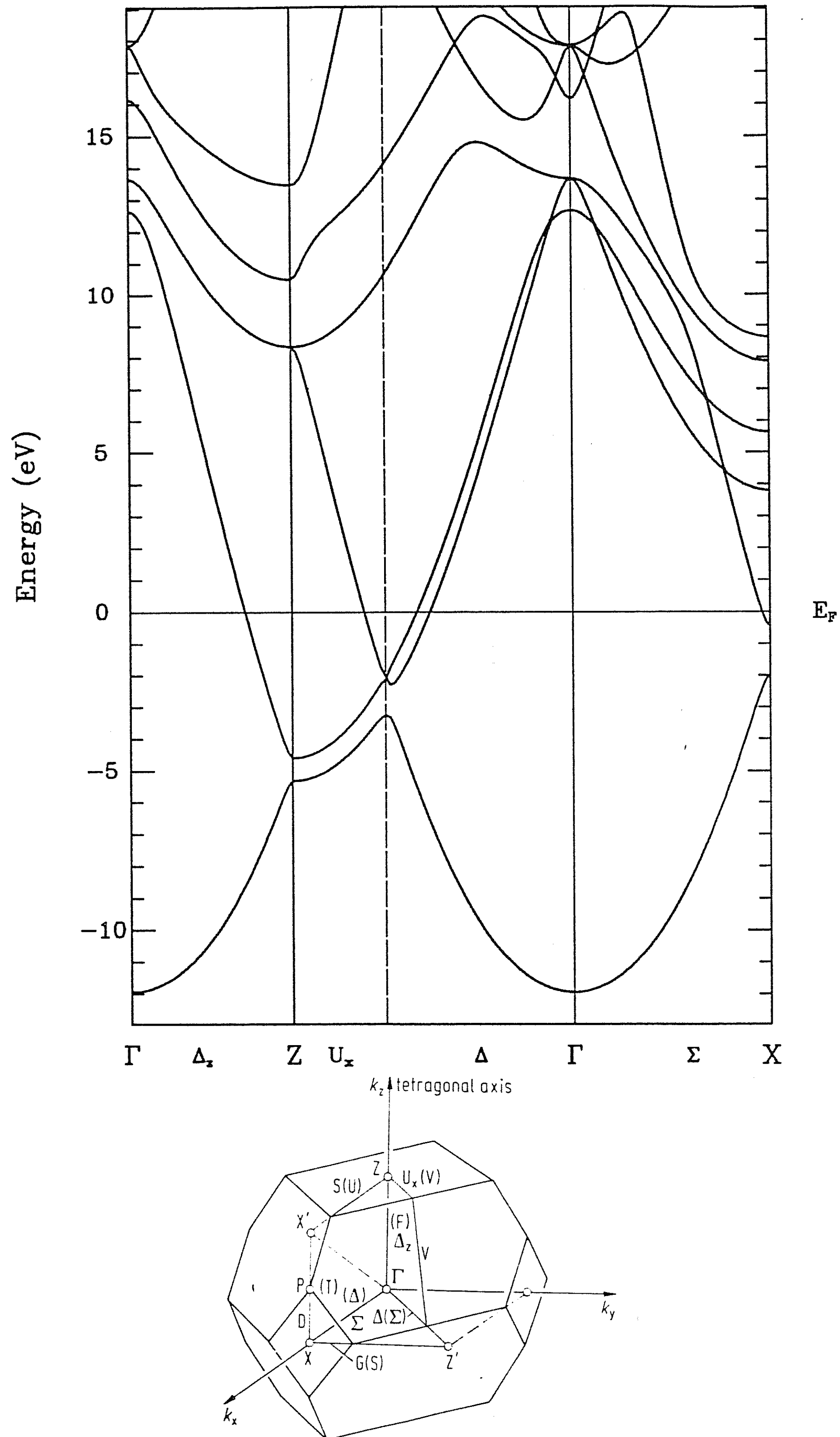

Figure 3.12: The band structure of GaIII along some high symmetry lines in the Brillouin Zone.

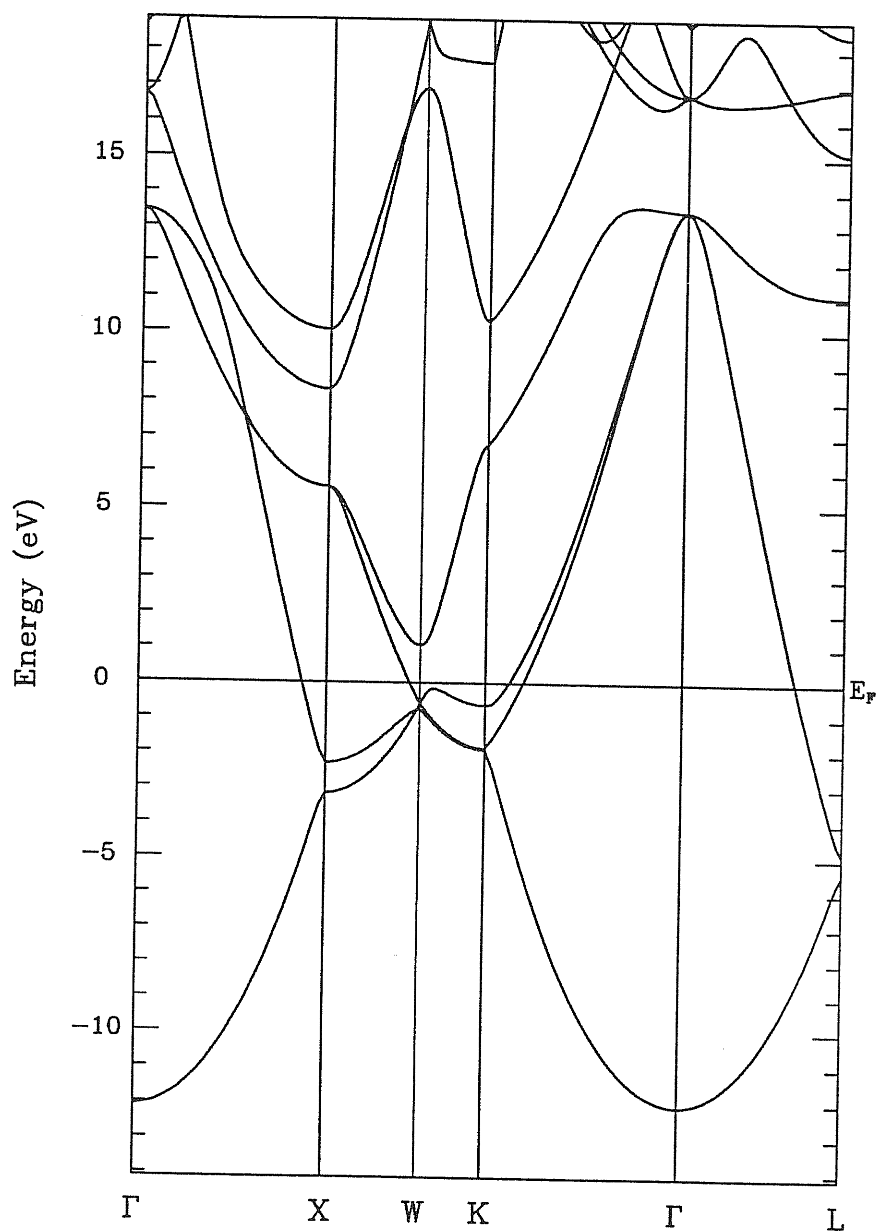

Figure 3.13: The band structure of fcc-Ga along some high symmetry lines in the Brillouin Zone. Points are labelled following Zak [52].

behaviour, apart from a close multiplet K^* of reciprocal lattice vectors ([113] [121] [022] [004]) which is enhanced in $S_c(\mathbf{k})$. Unfortunately here the situation is different from diamond where the presence of the covalent bond gives rise to a forbidden reflection at $\frac{2\pi}{a}(222)$, and its presence is thus directly confirmed by X-ray measurements [53]. In the case of α-Ga the reflection at the the K^* multiplet is not forbidden by symmetry as shown by the presence of a (small) contribution to the K^* multiplet from $S_a(\mathbf{k})$ [8]. For this reason if one includes core electrons in the calculation of the electronic structure factor, as should be done for a comparison with X-ray intensities, the difference between $S_c(\mathbf{k})$ and $S_a(\mathbf{k})$ become much less pronounced, being of only few % at the K^* multiplet, and almost impossible to detect experimentally [55]. Thus, rectifying the suggestion in ref. [8] we can now state that *X-ray measurements cannot be used to confirm the presence of the covalent bond.* The presence of the covalent bond should therefore be confirmed only indirectly by studying situations where it is expected to play a crucial role such as, for instance, the physics of α-Ga surfaces discussed in the following chapters.

4 The α-Ga(001) Surface

4.1 Surface Structure

The (001) surface is the main stable surface of α-Ga, with the highest packing density. It appears spontaneously on the crystal. The structure of the α-Ga(001) surface has been recently investigated by Scanning Tunnel Microscopy (STM) [13, 14], where it appears to be exceptionally stable: no step diffusion or other type of surface mobility was detected up to the bulk melting point ($T_m = 303K$). More surprisingly, at T_m the Ga crystal begins to melt from *inside* the sample, with the surface still appearing flat, and atomically ordered [14]! In figure 4.1 we reproduce an STM image of a sample cooled to room temperature just after onset of bulk melting [14]. A large hillock (height ~ 500 Å) is observed on the otherwise flat (001) surface. It is part of a micrometer-size droplet solidified after cooling below T_m. The area around this hillock is still in its original, atomically flat state. The surface has the typical terrace structure with atomic steps separated by several 100 Å. Obviously the liquid does not wet the (001) surface. The droplet forming the hillock structure must have emerged from the underlying bulk. From the fact that atomically flat regions coexisted with a macroscopic liquid droplet on the surface, Züger and Dürig concluded [14] that the (001) surface was still stable when part of the underlying sample had already undergone the melting transition.

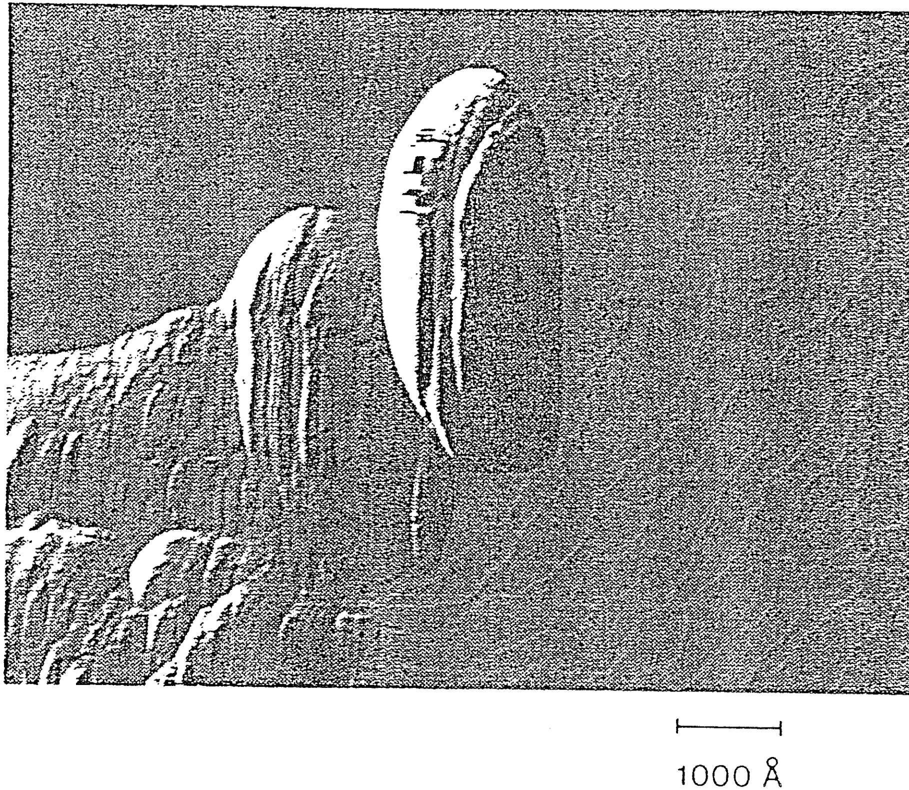

Figure 4.1: Representative image of the (001) surface after heating to T_m and cooling to 296 K. The hillock is part of a solidified droplet of liquid Ga that emerged from the underlying bulk at T_m while the area around the hillock remained in its crystalline state. The figure is taken from ref. [14].

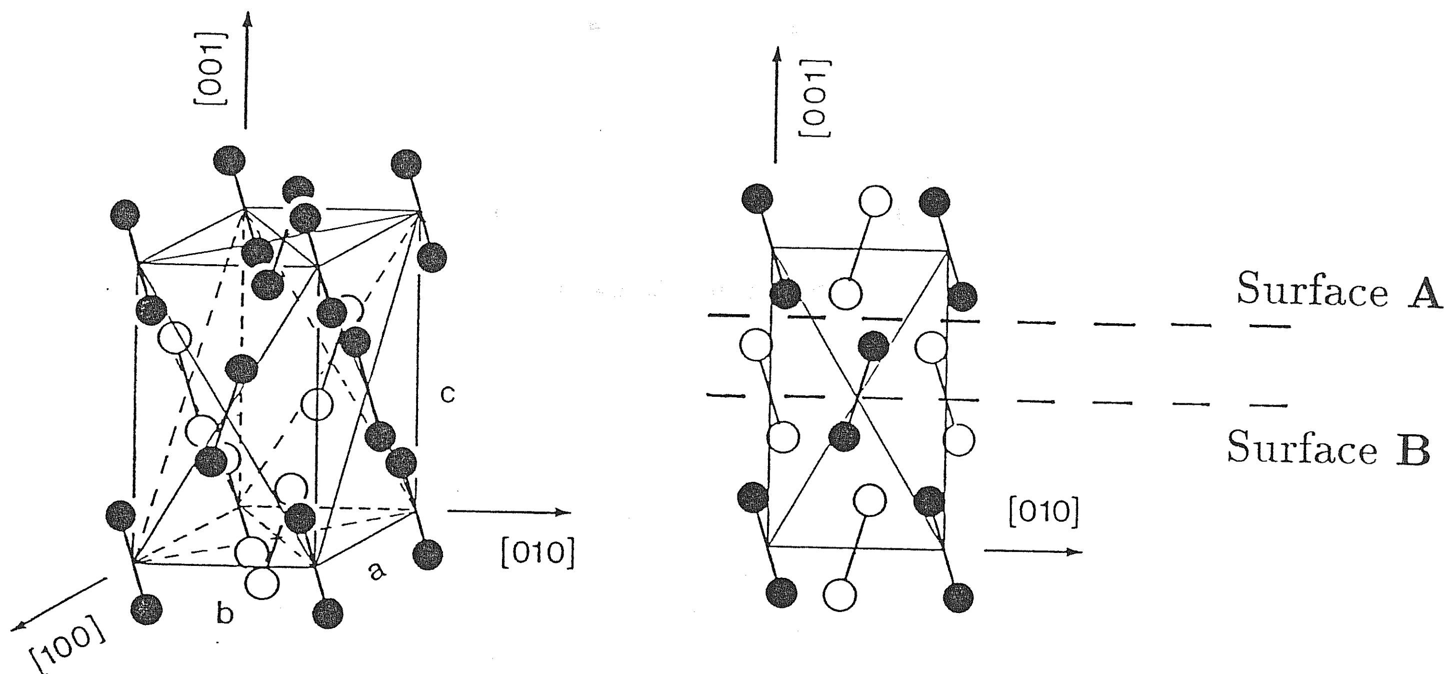

Figure 4.2: a) Orthorhombic unit cell of α-Ga. b) Side view on the (100) plane (solid circles) and on the next lower plane (open circles) at a depth of a/2. The dimers lie within the (100) planes. A and B indicates two inequivalent cuts of the bulk.

Besides this rather anomalous thermal behaviour, this surface raises additional questions. In principle, in fact, the ideal α-Ga (001) surface can be formed in two ways, by cutting the crystal at a) a plane that separates dimer layers, without cutting "covalent" bonds (surface A), or at b) a plane that cuts the dimer covalent bonds (surface B) (see fig. 4.2).

The top-view geometries for the ideal surfaces A and B are the same, and can be described by a nearly square lattice with two atoms per surface cell, forming chains along the [100] direction, with coordinates (in lattice units) (0,0,0) and (0.5,0.34,0). The STM map, shown in fig. 4.3a, clearly shows this chain structure [13].

Close inspection of the STM image in fig 4.3a reveals a dimerization reconstruction. Locating the surface atoms at the maxima of the current spots in the image, Züger and

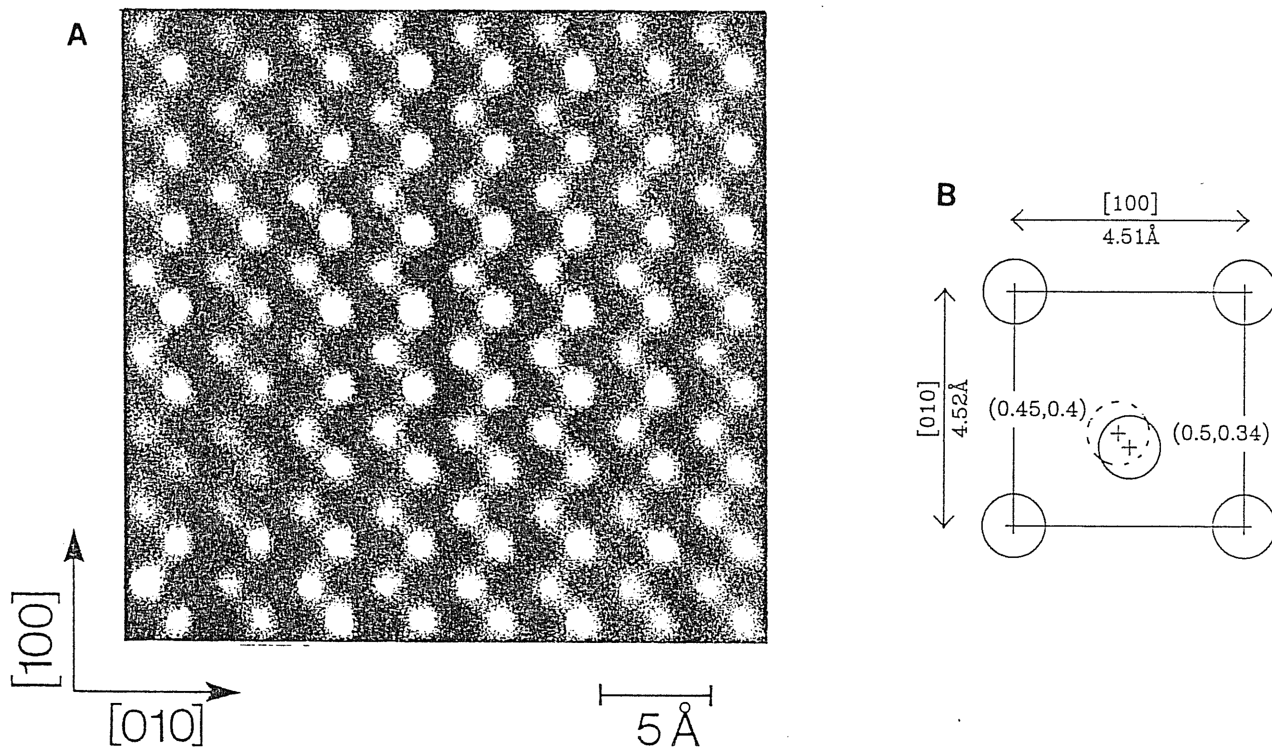

Figure 4.3: a) Experimental STM image of α-Ga(001) [13]. It has been measured using an Ir tip and tunneling parameters $I_t = 1\,nA$ and $V_t = -0.3V$ (a negative voltage means tunneling out of occupied sample states). The corrugation calculated from the signal is ~ 0.2Å$_{\mathrm{pp}}$. b) Truncated bulk structure of the α-Ga(001) surface (solid circle) and the reconstruction (dashed circle) as inferred from STM images [13].

Dürig assigned to the atom at the center of the cell a shift of ~ 0.35Å, from the ideal position (0.5,0.34) to (0.45,0.4) (in lattice units, see fig. 4.3b). They also found a ~ 0.05Å buckling of the two atoms. The dimerization of the chain is independently supported by the static LEED measurements which show a non zero intensity of the spots (2n+1,0) (in the surface notation), where n is an integer [13]. These spots would have zero intensity in the ideal geometry, due to the presence of the (100) mirror plane. We remark however that a buckling of the atoms in the unit cell, still preserving the (100) mirror plane, should be sufficient to produce the (2n+1,0) spots in LEED. Now, if both configurations A and B were simultaneously realized, for example in adjacent domains, then steps with a height of $c/4 \simeq 1.9$Å should be present; conversely if one of the two surfaces had a much lower energy, the smallest step height expected would be $c/2 \simeq 3.8$Å. The observed step-height distribution [13] supports the latter scenario, with just a single step of 3.8Å height (see fig.4.4). However, this still does not distinguish between possibilities A, B, or others.

In order to solve the aforementioned problems we have studied both surfaces A and B within the total energy framework presented in chapter 2. Part of our results on the (001) surface has been already published in ref. [56]. As customary [57] the surfaces have been modeled by periodically repeated slabs, 10 to 14 layers thick, separated by four vacuum layers. (If not otherwise specified the two surfaces of the slab are identical.) Convergency of k-sums has been tested up to 49 k points in the irreducible ideal surface BZ (ISBZ); simple gaussian spreading with variance from 20 to 5 mRy has been used. The lattice parameters and the starting atomic positions were obtained by an independent bulk calculation (see chapter 3). Guided by the calculated Hellmann-Feynman forces we let the atoms in the slab relax to their lowest energy positions, with residual forces less than $1.5\, 10^{-3} Ry/a_o$.

Figures 4.5a and 4.5b show the electronic (pseudo) charge density on a (100) plane,

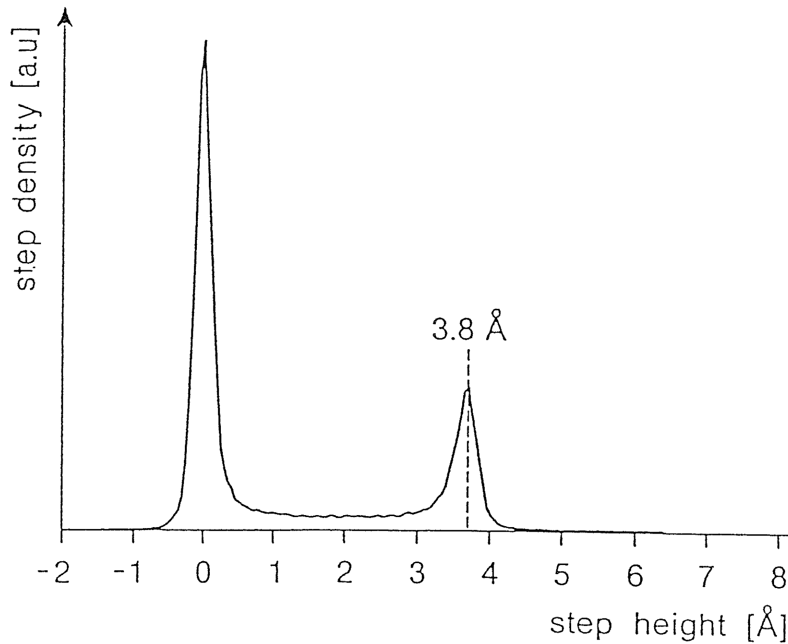

Figure 4.4: Histogram of the step-height distribution measured by STM [13]. The peak at zero height results from atomically flat terraces. There is no indication of steps with a height of 1.9Å, which would originate from monoatomic steps. The figure is taken from ref. [13].

for fully relaxed configurations of surfaces A and B respectively. Both relaxed surfaces A and B do not present the chain dimerization inferred from STM, as one see from the plot of the charge density on the surface plane in figure 4.6.

Surface A has energy $\gamma = 70\,mRy/atom$ when unrelaxed, and $57\,mRy/atom$ when fully relaxed. For the unrelaxed and relaxed B surfaces we find $\gamma = 59$ and $57\,mRy/atom$ respectively [1]. Surface energies were obtained by subtracting from the slab total energy the bulk energy for the same number of atoms, calculated with a k-points sampling as close as possible to that used in the slab calculation. Surface energies are converged within $\pm 1\,mRy/atom$ with respect to k points (9-49 in ISBZ), gaussian spreading (20-5 mRy), slab thickness (10-14 layers) and vacuum thickness (4-6 layers).

[1]Despite the stiffness of the covalent bond, the change in atomic coordination (surface B is obtained by breaking only one stiff covalent bond, while 4 metallic "bonds" are broken in surface A) makes the unrelaxed surface A higher in energy than unrelaxed surface B.

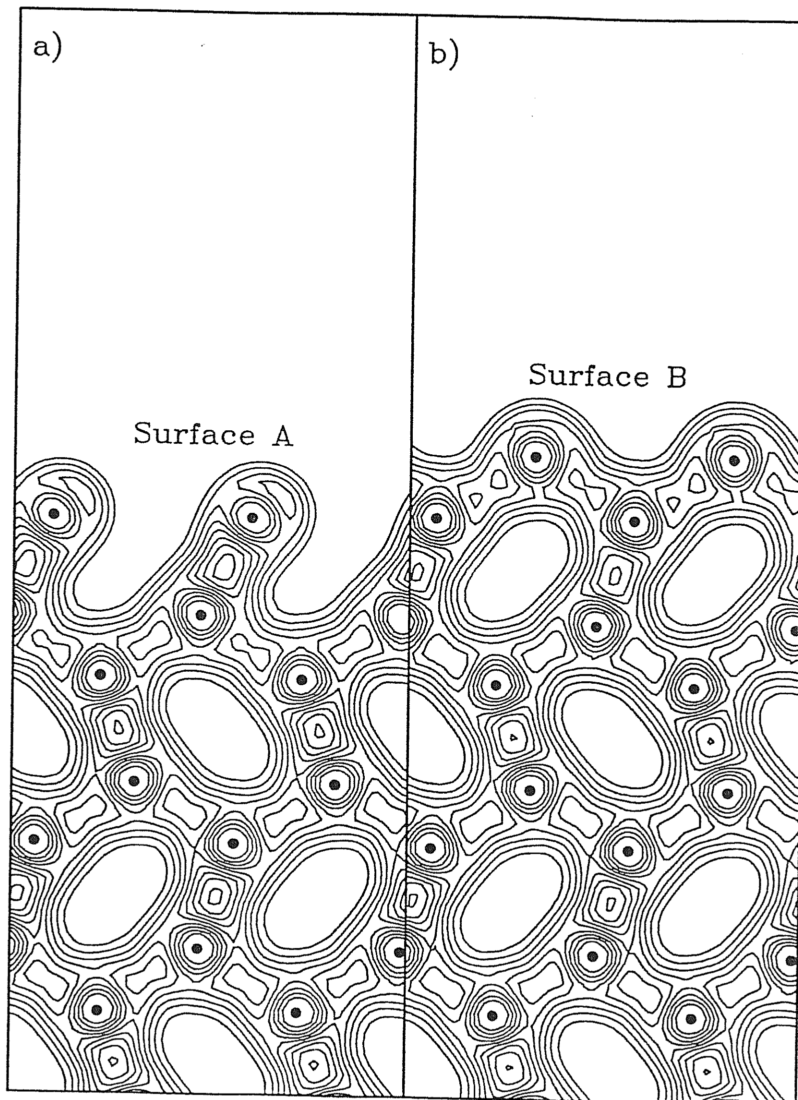

Figure 4.5: a) Charge density of relaxed surface A plotted onto the (100) plane passing through all atoms shown, $\gamma_A = 57\,mRy/atom$; b) same as in a) for surface B, $\gamma_B = 57\,mRy/atom$. Contour lines are separated by 0.005 a.u..

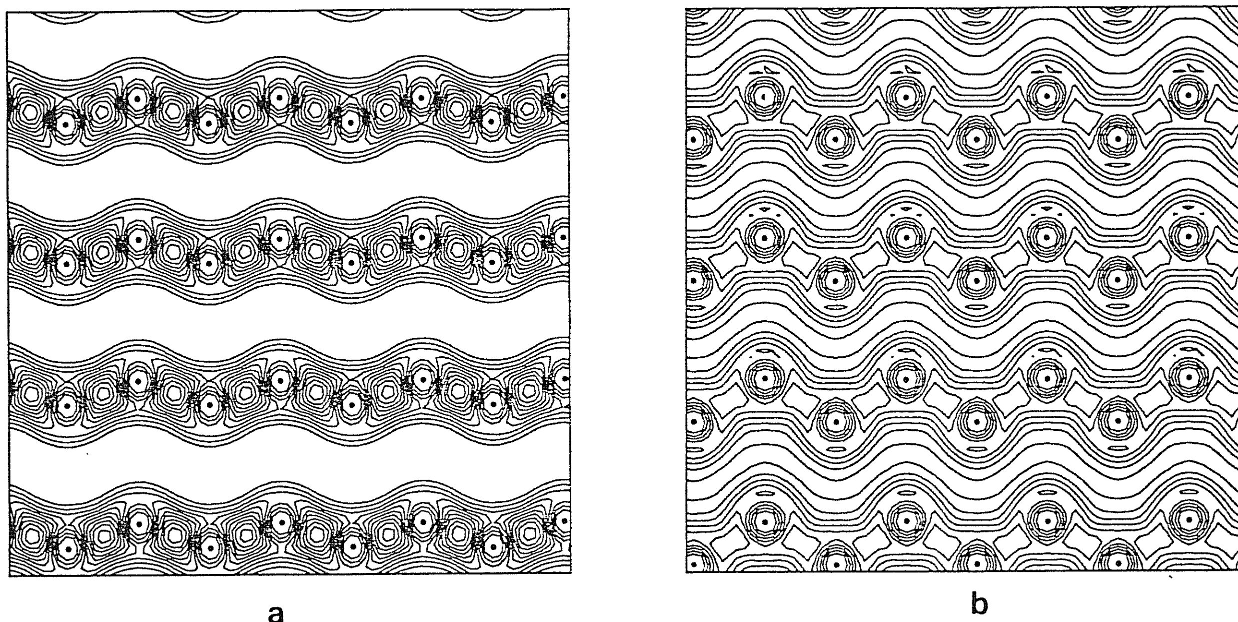

Figure 4.6: a) Charge density of relaxed surface A plotted onto the surface plane (001). b) same as in a) for surface B. Contour lines are the same as in fig. 4.5.

These values for the surface energies appear to be high when compared with the T=0 K extrapolation of the experimental result $\gamma_{expt.} \sim 41\,mRy/atom$ [58]. The two relaxed surfaces A and B end up having the same energy, which does not explain the STM step-height distribution. Moreover, the strong corrugation of charge density in surface A (see fig. 4.5a) looks unreasonable, and indirectly suggests the existence of a different ground state. Also, the chain structure in surface A is different from the STM image: the chains are exceedingly packed when compared to the STM picture (cfr figs. 4.6 and 4.3a). Surface B is instead far more compact, and its chain structure is very similar to the STM image, but it has one unsaturated dangling bond per atom, which again suggests instability. (Details on the electronic structure of the two surfaces will be given in the next section). Guided by this reasoning we rearranged drastically surface A, by pushing the outermost atom down to fill the hole underneath. This is equivalent to adsorbing a plane of adatoms onto surface B, therefore removing the dangling bonds. We find a dramatic lowering of γ

down to 47 $mRy/atom$, which now compares much better with the experimental value.

The charge density of the new optimal configuration (hereafter referred to as C) on the (100) and (001) planes is plotted in fig. 4.7a and 4.7b respectively. Atomic coordinates are given in the figure caption [2]. Remarkably, the top-view geometry of surface C is still similar to the ideal surface. In particular the chains along the [100] direction still survive. Our results do not explain the chain dimerization, and the buckling but these effects probably involve energies below our present resolution. We will discuss further this point in section 4.3.

In fig. 4.8 we compare the STM experimental image [13] with the theoretical STM image calculated for surface C in the Tersoff-Hamann approximation [59]. The approximations involved in the calculation of the STM image are summarized in appendix B. The characteristic chain present in the data is very well reproduced by our model. Also the non-spherical shape of the experimental current spots, with a flat region at one side, compares well with our theoretical image.

Remarkably, the structure of the two outermost surface layers of surface C and their optimal charge density have become very reminiscent of those of bulk GaIII (see fig. 4.7a). Bulk GaIII is a tetragonally distorted FCC structure, stable at high pressure and temperature [2] (cfr. chapter 3), and appears to wet epitaxially the α-Ga(001) lattice in configuration C. Actually, the chain structure at surface C is not present in the geometry of unstrained GaIII. However we have checked that, by forcing GaIII to have the same

[2] For completeness we give here the atomic coordinates for relaxed surfaces A and B. The notation is the same as in figure 4.7.

Surface A: the fully relaxed interlayer distance for the outermost layers d_{12}, d_{23}, d_{34} are 0.500, 0.328, and 0.529 respectively, in unit of $a = 4.377$Å. The corresponding (x,y) in-plane coordinates (in unit of a) of the two atoms per cell in the four outermost planes are (0,0) (0.5,0.165); (0,-0.252) (0.5,0.417); (0,0.247) (0.5,-0.082); (0,0.414) (0.5,-0.249) respectively.

Surface B: d_{12}, d_{23}, d_{34} are 0.330, 0.532, 0.314 and 0.526 respectively. The (x,y) in-plane coordinates of the two atoms per cell in the four outermost planes are (0,0) (0.5,0.299); (0,0.493) (0.5,-0.195); (0,313) (0.5,-0.014); (0,-0.186) (0.5,484) respectively.

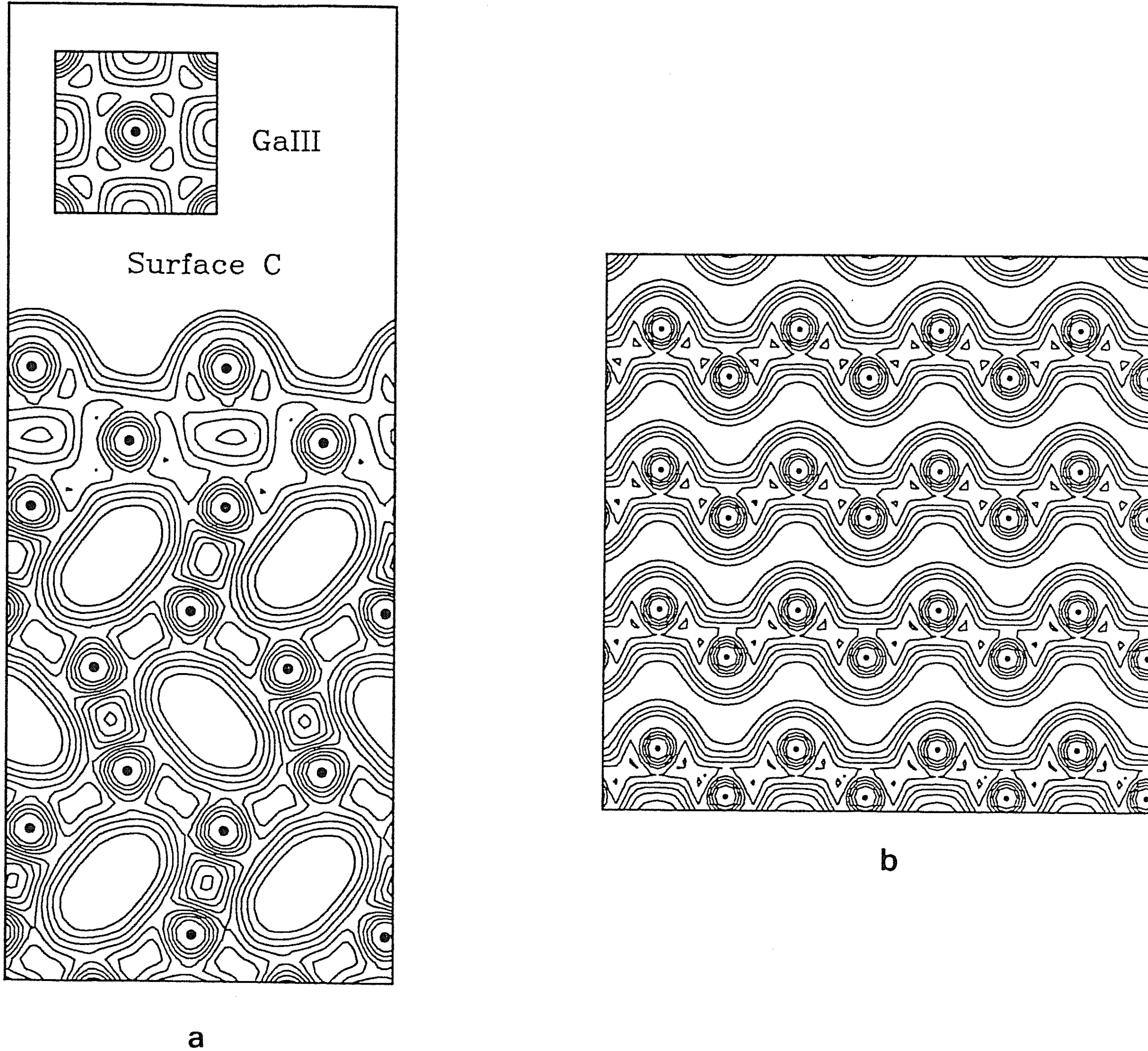

Figure 4.7: a) Charge density of our proposed optimal structure for α-Ga(001) (surface C). $\gamma_C = 47\,mRy/atom$. The fully relaxed interlayer distance for the outermost layers d_{12}, d_{23}, d_{34} are 0.380, 0.347, and 0.525 respectively, in unit of $a = 4.377$Å. The corresponding (x,y) in-plane coordinates (in unit of a) of the two atoms per cell in the four outermost planes are (0,0) (0.5,-0.324); (0,0.505) (0.5,0.171); (0,0.002) (0.5,-0.326); (0,0.179) (0.5,-0.502) respectively. The two outermost surface layers now mimic closely the bulk GaIII phase (inset). b) Charge density of surface C plotted onto the surface plane (001). Contour lines are the same as in fig. 4.5.

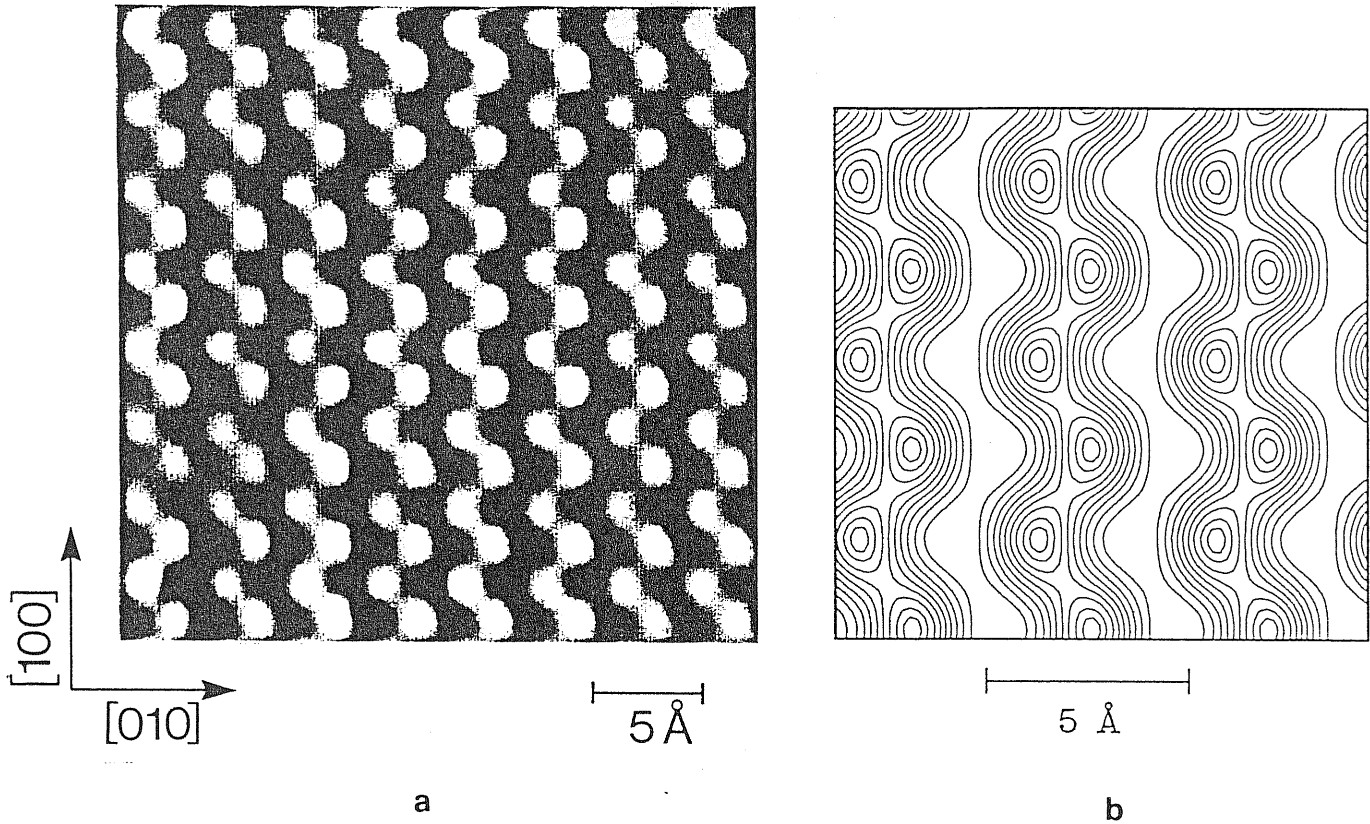

Figure 4.8: a) Experimental STM image of α-Ga(001) [13]. b) Local density of states $\rho(\mathbf{r}, \Delta E)$ calculated for surface C at a plane $z \simeq 2$Å above surface atoms, and including states inside an energy window $\Delta E = 0.5$ eV below the Fermi level. States from 36 k points at the boundary of the ISBZ were included. In the simplest approximation this plot corresponds to the theoretical STM image with states at the ISBZ boundary playing the major role [59]. Note the close similarity of features in the two pictures. We have checked that the use of a uniform mesh of 49 k points in the IBZ, and the extrapolation of the wave functions tails up to 8 Å from the surface, as described in appendix C, does not change qualitatively the STM image.

in plane lattice constants as those of α-Ga, its original FCC-like symmetry is unstable and the chain structure appears also in the bulk. This structure mimics GaIII epitaxially grown on α-Ga and will be referred to as "epitaxial GaIII". A separate study (made with a 12-layer slab) of the free surface of epitaxial GaIII gives rise to a top layer structure which is identical to that of our surface C [3]. We also find that the surface energy of epitaxial GaIII (γ_{III}) is $43\, mRy/atom$. This value is sufficiently lower than the surface energy of the ideal configurations ($\gamma_A = \gamma_B = 57\, mRy/atom$) to make it worth paying for an additional α-Ga/GaIII interface plus the difference in bulk energies of α-Ga and epitaxial GaIII ($\Delta E = E_{bulk}$(epitax. GaIII) - $E_{bulk}(\alpha$-Ga)) which we have separately calculated to be $\Delta E \sim 5\, mRy/atom$. All these results support the prediction that *in the ground state the (001) surface of α-Ga should be wetted by two layers of GaIII epitaxially grown on α-Ga.* This prediction is now open for direct experimental verification.

We have also calculated the surface stress tensor , which we find to be tensile for surface C: $-\partial\gamma/\partial\epsilon_{xx} = -27\, mRy/atom$ and $-\partial\gamma/\partial\epsilon_{yy} = -53\, mRy/atom$. ($x$ and y are the [100] and the [010] directions in fig. 2, and ϵ_{ij} is the strain. The "k-point correction" discussed in chapter 2 is included and equal to $-22\, mRy/atom$, and $-3\, mRy/atom$ for $-\partial\gamma/\partial\epsilon_{xx}$ and $-\partial\gamma/\partial\epsilon_{yy}$ respectively). The presence of a negative surface stress is obviously connected with the lateral expansion required for the structure of GaIII to fit epitaxially on α-Ga, with the associated contraction in the vertical direction.

Once wetting has begun, one might perhaps expect the number of layers to grow. However, since adding a third GaIII layer produces a step height roughly one half the experimental value, the wetting must in fact be confined to the first two layers up to T_m,

[3]The distance along the [010] direction of the two surface atoms in the unit cell are 0.319, and 0.321 (in unit of a = 8.271 a.u.) for epitaxial GaIII surface and surface C respectively. For bulk epitaxial GaIII the same quantity is 0.358, i.e. the chains along the [100] direction in epitaxial GaIII are more packed at the surface than in the bulk.

in order to be consistent with STM. Indeed, by a separate calculation, we find that the surface energy of the relaxed configuration with *three* layers of GaIII (γ_3) is as high as $60\, mRy/atom$, and that with *four* GaIII layers is $\gamma_4 = 65\, mRy/atom$ [4] (The charge density of the configuration with 3 GaIII layers is reported in fig. 4.9). These values, compared with that of surface C ($\gamma_C = 47\, mRy/atom$), guarantee that surface domains with one and two, or with two and three GaIII layers are unlikely to be simultaneously present, in agreement with the observed step height distribution. Furthermore the surface energy for three GaIII layers is much higher than the value obtained by adding to γ_C the bulk energy difference ΔE, required by the added GaIII plane.

We may write the overall surface energy of the configuration with n layers of GaIII on top of α-Ga as a sum of physically distinct terms

$$\gamma_n = \gamma_{III} + \gamma_{\alpha-III} + n \cdot \Delta E + V(n) \tag{4.1}$$

where $\gamma_{\alpha-III}$ is the unperturbed interface energy (as obtained in the limit $n \to \infty$), and $V(n)$ is an interface-surface interaction potential.

From the above calculation we know γ_{III} and ΔE, while $\gamma_{\alpha-III}$, and $V(n)$ are still unknown. Since $\gamma_4 - \gamma_3 \sim \Delta E$, we may assume $V(n)$ to be negligible for $n \geq 4$. Under this assumption the interface energy $\gamma_{\alpha-III}$ can be obtained from eq. 4.1, and from the known quantities γ_4, γ_{III}, and ΔE as $\gamma_{\alpha-III} = \gamma_4 - \gamma_{III} - 4\Delta E = 2\, mRy/atom$. From eq. 4.1 and this estimated value of $\gamma_{\alpha-III}$ we can now deduce also the interaction energy $V(n)$. We find $V(2) = -9$, and $V(3) = -1\, mRy/atom$ respectively for the $n = 2$ (surface C), and 3 GaIII layers. The surface-interface interaction is therefore strongly attractive and limits the wetting film thickness to strictly two atomic layers, causing the wetting of

[4] γ_4 is obtained from a fully relaxed slab, 12 layers thick, where one surface has the geometry of configuration C, and the other is covered with four layers of GaIII.

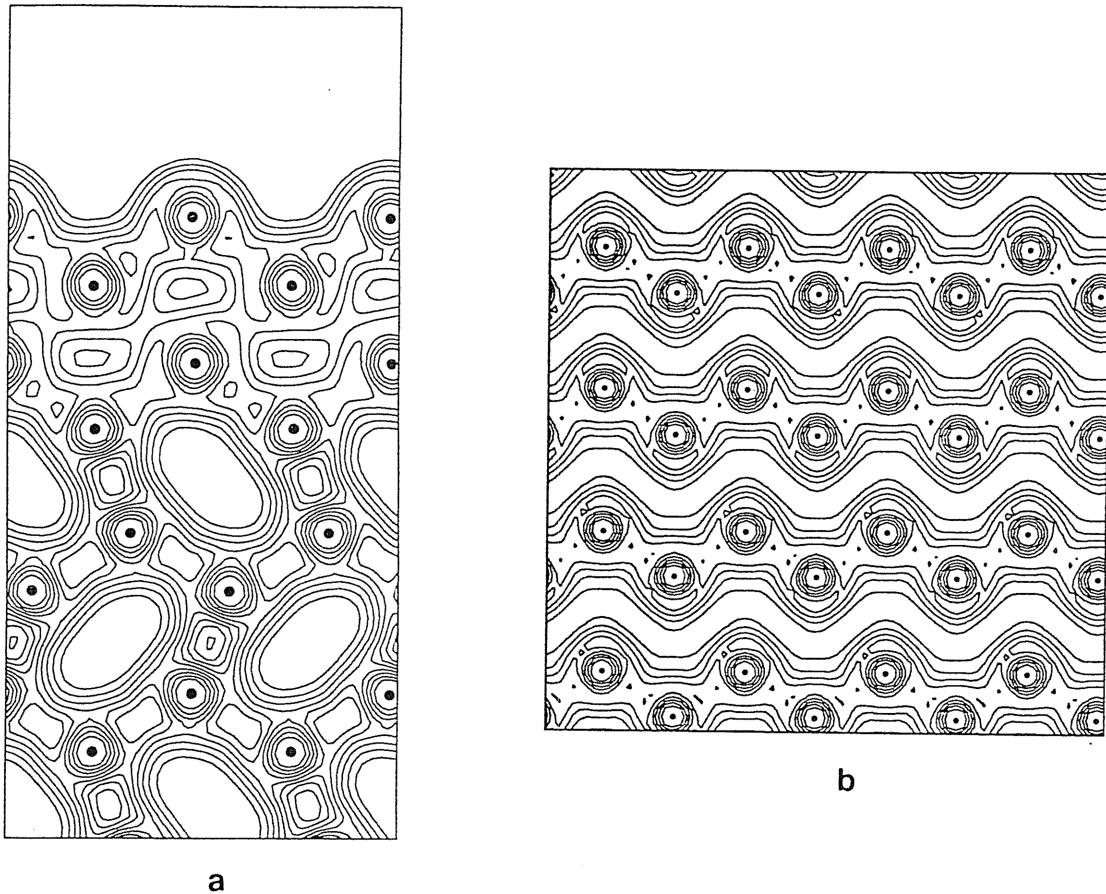

Figure 4.9: a) Charge density of the relaxed configuration with three GaIII layers plotted on the (100) plane passing through all the atoms shown. The three outermost layers mimic closely the bulk GaIII phase. (see inset of fig. 4.7a). The surface energy is $\gamma_3 = 60\,mRy/atom$. b) Charge density plotted on the surface plane (001) for the same configuration as in a).

α-Ga by epitaxial GaIII to be incomplete.

The surface energy balance described above raises two puzzling questions, namely why is $\gamma_{\alpha-III}$ so small, and why is $V(n)$ so attractive. The interface energy could be roughly expected to be a substantial fraction of the overall surface energies, due to the difference in density of the two phases ($\sim$ 10%). An attraction between α-Ga and the GaIII-like surface is also unexpected, since the two lattices are very different and spontaneous epitaxy correspondingly difficult. This attraction is not associated with a visible dependence of the local atomic structure of the interface on the film thickness. In fact the interplanar

	$\alpha + 2\,(C)$	$\alpha + 3$	$\alpha + 4$	$\infty\ (GaIII)$
d_{12}	0.386	0.344	0.357	0.361
d_{23}	–	0.396	0.397	0.392
d_{34}	–	–	0.400	0.404
d_I	0.346	0.346	0.340	–
d_{dimer}	0.525	0.526	0.529	–

Table 4.1: Interplanar distances of the outermost surface layers for configurations with 2,3,4 and ∞ numbers of GaIII layers epitaxially grown on α-Ga. The distance are in lattice unit (a=8.27 a.u.). d_I correspond to the interplanar distance between the innermost GaIII layer of the film and the outermost dimer of α-Ga. d_{dimer} is the bond length of the outermost dimer of α-Ga. Note that both d_I and d_{dimer}, i.e. the interface structure, are poorly dependent on the thickness of GaIII film. $d = 0.398\,a$ in bulk epitaxial GaIII, and $d_{dimer} = 0.528\,a$ in bulk $\alpha - Ga$.

distances for the configurations with different numbers of GaIII layers reported in table 4.1 show a nearly constant interface structure (d_I and d_{dimer} in table 4.1). The origin of both the smallness of $\gamma_{\alpha-III}$ and the surface-interface attraction should therefore have a more subtle electronic origin. The distinguishing feature of GaIII is its unmitigated metallicity, as opposed to the semi-metallicity of α-Ga. We will see in the next sections that surface metallization might precisely be the key to understand both the above points.

The surface-interface attraction produces a 3D atomic density in the GaIII film in surface C roughly 8 % higher than the bulk equilibrium density of epitaxial GaIII [5]. If this density increase were obtained by hydrostatic pressure it would cause GaIII to melt about 100 K above the melting temperature of α-Ga [6]. We believe that this finding could account for the anomalous thermal stability of the α-Ga(001) surface detected experimentally [13, 14].

[5]The volume per atom in the GaIII film in surface C is 103 a.u, while in bulk epitaxial GaIII it is 112 a.u.

[6]The estimate of the melting temperature of GaIII were obtained by linear extrapolation of the experimental liquid-GaIII coexistence line in ref. [2] up to the pressure needed to induced a 8% density increase of bulk GaIII at 0 K.

4.2 Surface Electronic Properties

Work function: The work function ϕ has been computed as $\phi = \tilde{V}_H(vacuum) - E_F$, where E_F is the Fermi energy and $\tilde{V}_H$ is the macroscopic average of the Hartree potential defined as [60]

$$\tilde{V}(z) = 2/c \int_{z'-c/4}^{z'+c/4} dz' \int d\mathrm{x}\, V_H(\mathrm{x}, z') \tag{4.2}$$

z is perpendicular to the surface, and the $d\mathrm{x}$ integral is in the surface planes, c/2 is half the lattice parameter c of α-Ga, which corresponds to the periodicity along z direction of the planar averaged Hartree potential in the bulk. $\tilde{V}(z)$ is constant is the vacuum and central regions of the slab as shown in figure 4.10.

	A	B	C	$\alpha + 3$	$GaIII$	(010)	$exp.$
$Work\, function\, (eV)$	4.35	4.86	4.44	4.39	4.44	4.39	$4.32 \div 4.39$

Table 4.2: Work function for different surface configurations (cfr. section 4.1). GaIII refers to a relaxed slab of epitaxial GaIII, $\alpha + 3$ refer to α-Ga wetted by 3 layers of GaIII. The work function for surface C is obtained from a 14-layers slab. The corresponding value for a 10-layer slab is 4.56 eV. The experimental work function refers to a polycrystalline sample [36]. The calculated work function for our proposed ground state configuration of (010) surface is also reported (cfr. chapter 5).

The values of the work function for our proposed ground state, surface C, and for the other less stable structures are summarized in table 4.2. The agreement with the experimental work function is remarkable. The most corrugated surface A has the lowest work function as expected from the Smoluchowski charge smoothing argument [61]. The same argument does not apparently apply to the comparison of the work functions of surfaces B and C, which have similar corrugations [7], but a 0.5 eV difference in the work function. The reduction of the work function of surface C is due to the presence of a dipole moment at the α-Ga/GaIII interface of opposite sign with respect to the surface

[7] The outermost interplanar distance is $0.329a$, and $0.386a$ for surface B and C respectively.

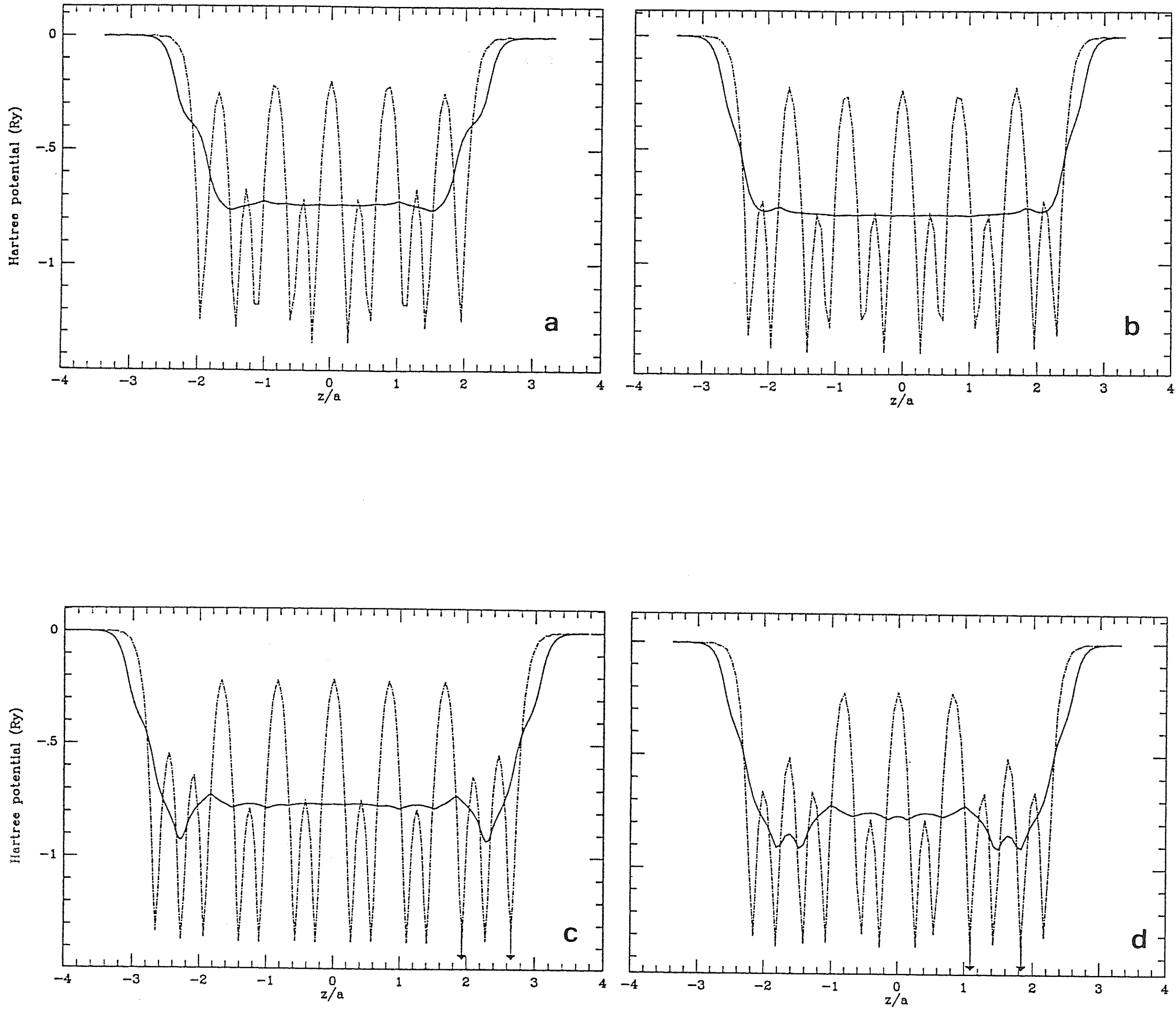

Figure 4.10: Planar averaged Hartree potential plotted along the [001] direction (dash-dotted line), and its macroscopic average $\tilde{V}_H$ in eq. 4.2 (continuous line) for a) surface A, b) surface B, c) surface C, and d) α-Ga wetted by three GaIII layers. The slabs have different thickness. The distance along the [001] direction are in unit of a= 8.27 a.u.. The positions of the surface plane and of the α-Ga/GaIII interface are marked by arrows. The non constant value of $\tilde{V}_H$ in the center of the slab in panel d) is due to the interplanar relaxations propagating deeply in the slab. The two surfaces of the slabs are identical.

dipole. This interface dipole shows up as a drop in $\tilde{V}_H$ at the α-Ga/GaIII interface in fig. 4.10c, absent in surfaces A and B (cfr. figs. 4.10a, b). A similar drop in $\tilde{V}_H$ appears at the α-Ga/GaIII interface in the configuration with three layers of GaIII in fig. 4.10d. The interface dipole is produced by an electron transfer from the GaIII film to the α-Ga region, necessary to align the Fermi level of α-Ga and GaIII which are in bulk 5.76 and 6.61 eV respectively. This is the usual charge transfer at a bimetallic junction, producing a jump in electrostatic potential exactly equal to the difference in the bulk Fermi levels of the two materials [62]. α-Ga is more electronegative than GaIII which implies a contact potential of about 1 eV.

The fact that surface C and the surface of GaIII have the same work functions (cfr. table 4.2, also the work function of the configuration with 3 GaIII layers should be regarded as equal to that of surface C within our error) further confirms our picture with a surface dipole very similar in surface C and in the surface of GaIII, a local Fermi level in the GaIII film close to those of bulk GaIII (referred to the local average Hartree potential in the film and in bulk GaIII respectively) , and an interface dipole necessary to produce a jump in the electrostatic potential aligning the chemical potential across the interface.

The charge transfer decreases the energy cost of the interface. In fact the interface energy calculated for the junction of two jellia at different densities is negative for densities similar to those of α-Ga ($r_s = 3.05$). In the bimetallic junction of two jellia the lowering of the electron kinetic energy in the charge transfer in only partially cancelled by the Hartree and XC energy cost, ending up with a negative cost of the interface [63]. This effect produce a negative contribution to the α-Ga/GaIII interface energy which is probably responsible for the low value estimated for $\gamma_{\alpha-III}$ ($2\, mRy/atom$).

Band structure and electronic densities of states: The slab band structure of surface C along the high symmetry lines of the ISBZ is reported in fig. 4.11. In figs. 4.12, and 4.13 are reported for comparison the band structures of surfaces A and B.

The states in the energy regions forbidden in the bulk are surface states. An artifact of the slab geometry is that all surface states occur pairwise, one from each surface of the slab. For an infinitely thick slab the two states would be degenerate, but for finite thickness the two states hybridize and the degeneracy is lifted (an exception is the low lying surface state in the S direction of surface C). The splitting of surface states is drastically reduced by increasing the slab thickness: for example the splitting of surface states in configurations C, 7-8 eV below E_F, are reduced by a factor 3 by increasing the slab thickness from 10 layers to 14 layers, although the changes in surface structure and energy are negligible [8].

By comparing the electronic bands of different structures in figs. 4.11-4.13 one notes that filled surface states appear in the surface-projected bulk gaps 7-8 eV below E_F only in surfaces A and C. Conversely filled surface states in the surface-projected bulk gap along S and Δ' crossing the Fermi level are present only in surface B. The latter surface states in configuration B correspond to half filled bands of surface dangling bonds, produced by the cutting of the outermost Ga_2 dimer (cfr. fig. 4.13). The two bands, split by the surface-surface interaction across the slab, are both double degenerate: there is one dangling bond per atom in the surface unit cell. Each dangling bond is strongly localized on one of the atoms in the surface unit cell, as evident in figure 4.14. The two dangling

[8] This is a well known property: the surface energy and structure reach convergency with respect to the slab thickness much faster than the fine details of the band structure do. For the analysis of surface states one usually employes thicker slab, constructed by inserting "bulk" layers in the middle of a thinner slab, whose self-consistent potential is known. The potential for the inserted "bulk" layers are then put equal to the self-consistent potential at the center of the thinner slab. The rational for this stretching procedure is that the potential so defined is expected to be very close to the full self-consistent potential of the stretched slab. This procedure could be adopted in a future refined calculation of our band structures. At the time being the band structures reported here are sufficient to identify the main features of the surface electronic properties.

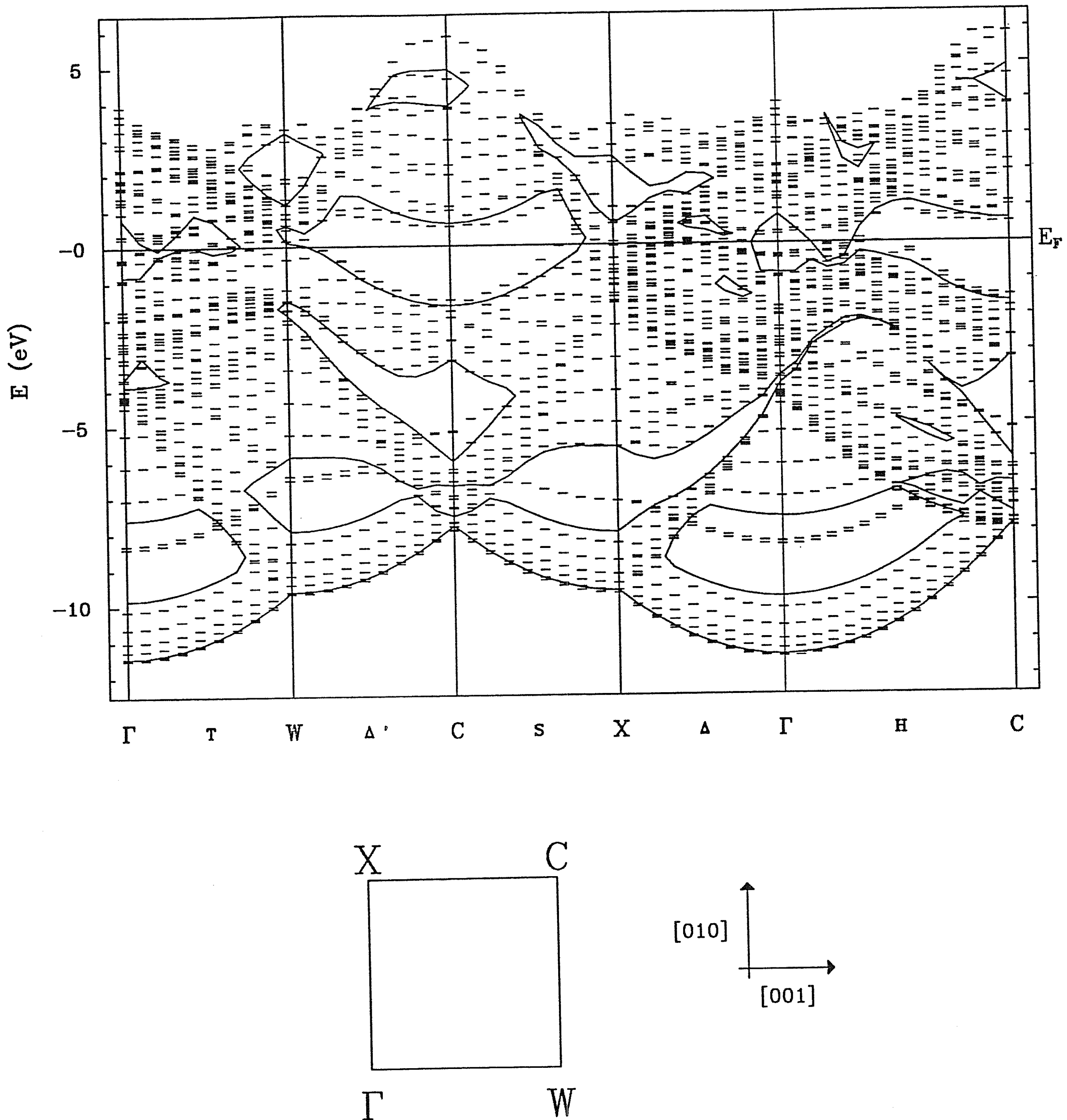

Figure 4.11: The surface band structure of configuration C from a 14-layers slab. Continuous lines represent the band edges of the surface-projected band structure of the bulk. The zero of energy corresponds to the Fermi level. The energies of bulk and slab calculations are aligned by matching the average Hartree potential in the bulk and at the center of the slab (cfr. fig. 4.10). Inset: Irreducible Surface Brillouin Zone.

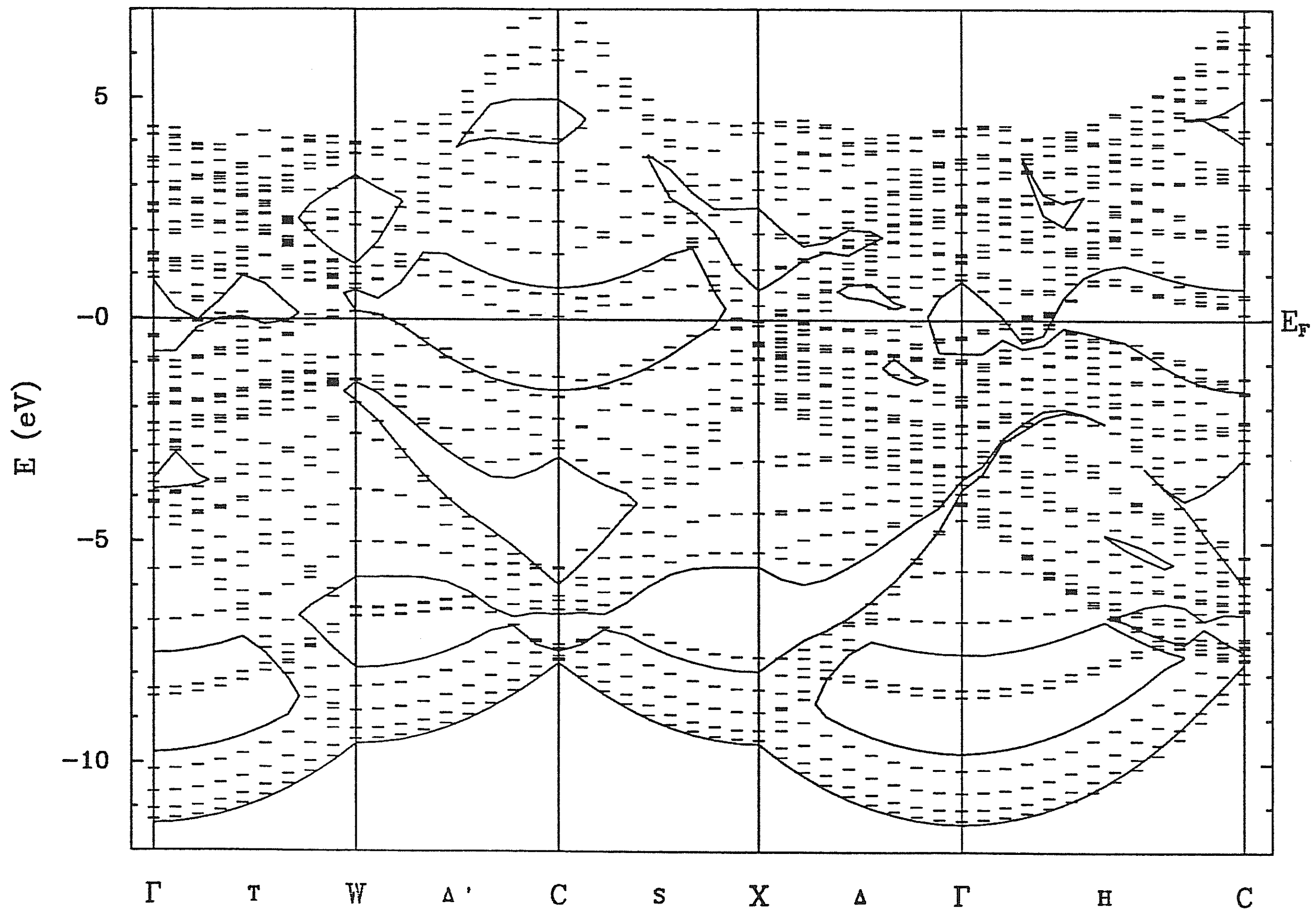

Figure 4.12: The same as in fig. 4.11 for surface A. The slab is 10 layers thick.

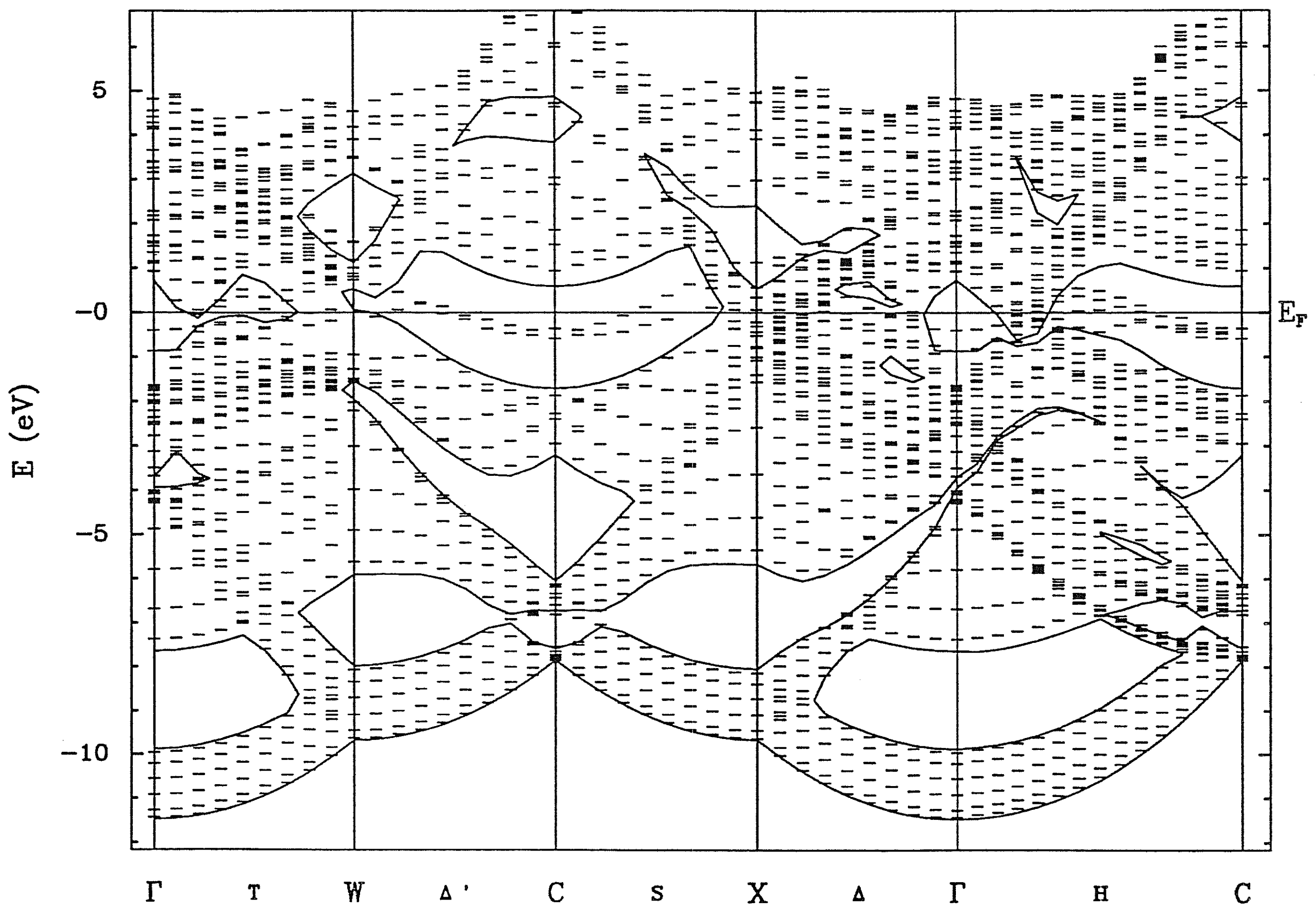

Figure 4.13: The same as in fig. 4.11 for surface B. The slab is 12 layers thick. The difference in the number of electronic states per k point in figs. 4.11-4.13 is due to different slab thickness.

bonds on different sublattices do not couple, they always point in opposite directions. They still "repel" each other if we artificially dimerize the chain along the [100] direction. Thus, surface B cannot be stabilized by the formation of filled bonding state and empty antibonding states, obtained from the coupling of the dangling bonds, as is the case for example on Si(100)(2x1) [64] [9]. The instability suggested by the presence of half filled dangling bonds bands, which induces a large peak in the surface projected density of states (SDOS) at E_F, is removed instead by the self-wetting scenario discussed above.

Not surprisingly, unsaturated dangling bonds at E_F are absent in both surfaces A and C. In surface A the nearly two electrons per surface atom, available after breaking the buckled metallic planes, participate in the formation of a strong bonding of the atoms along the [100] chains. These bonds, visible in the total charge density in fig. 4.5a, are mainly due to the deep surface states 7-8 eV below E_F in the band structure in fig. 4.12. The latter are plotted in fig. 4.15, they are responsible for the large contraction along [010] direction of the chains in surface A.

Coming back to our proposed ground state, surface C, one can recognize in fig. 4.11 surface states in three energy regions: i) surface states near Γ just above and below the Fermi level, ii) surface states 5 eV below E_F near the C point, iii) surface states in the surface-projected bulk gap 7-8 Ev below E_F extending almost throughout the BZ in fig. 4.11. These states show up very clearly in figure 4.16 where the SDOS is compared to the DOS projected in the center layer of the slab (bulk DOS). The surface states contribution to the SDOS are indicated as shaded areas in fig. 4.16.

The pseudogap at E_F in the bulk DOS is largely smoothed in the SDOS of surface C, which is now much more similar to the SDOS of epitaxial GaIII than to α-Ga bulk DOS,

[9]The dangling bonds repel each other also in the configuration obtained by moving the atom 2 in fig. 4.14 in the specular position with respect to the [010] plane.

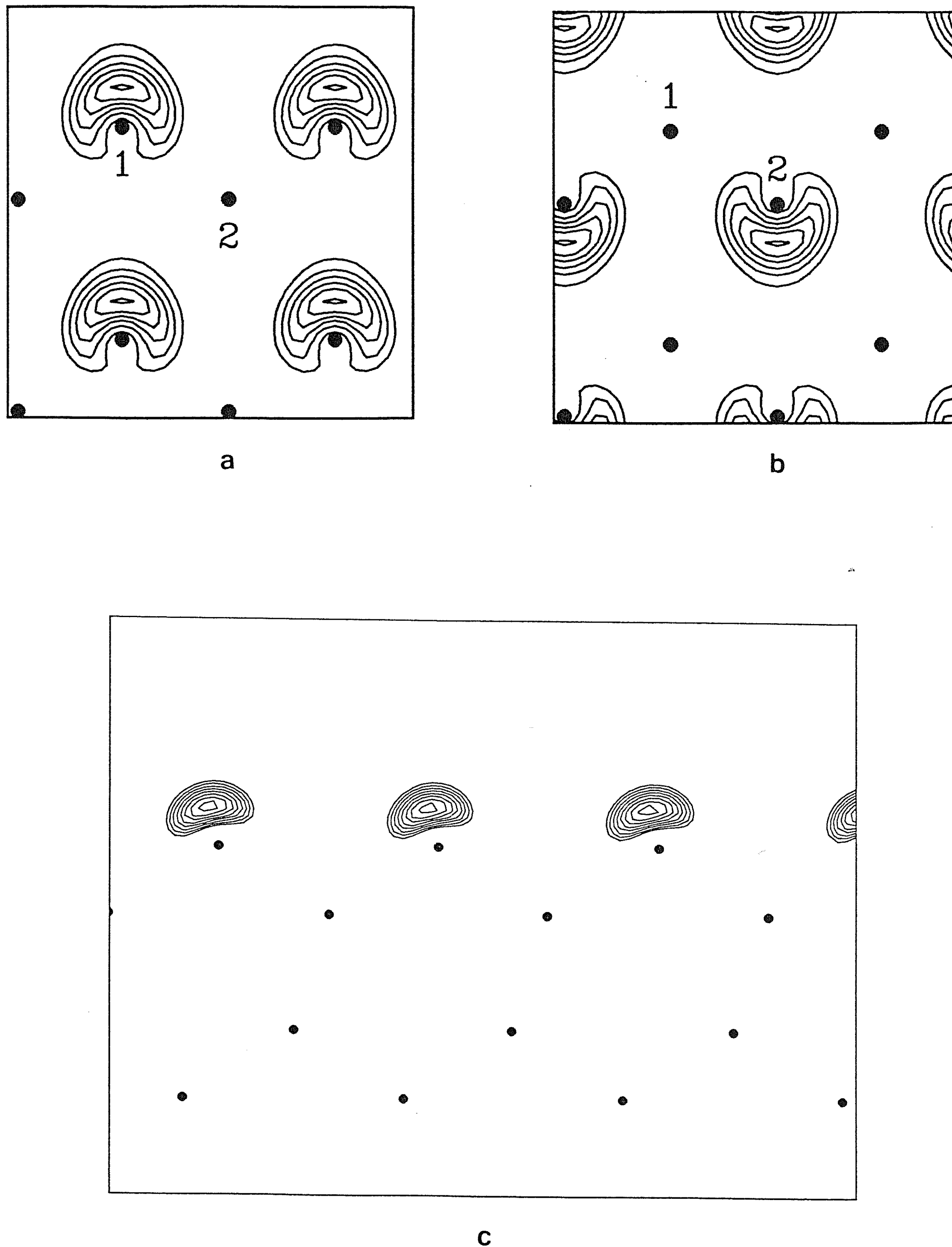

Figure 4.14: a) Charge density of a dangling bond state of surface B at 0.67 $k_{\Delta'}$, localized on atom 1 in the surface unit cell, plotted on the (100) plane. b) The same as in a) for the dangling bond localized on atom 2 in the surface unit cell. This eigenstate is degenerate in energy with the state in panel a). c) The eigenstate in panel a) plotted on the (001) plane. Contour lines are separated by 0.0005 a.u..

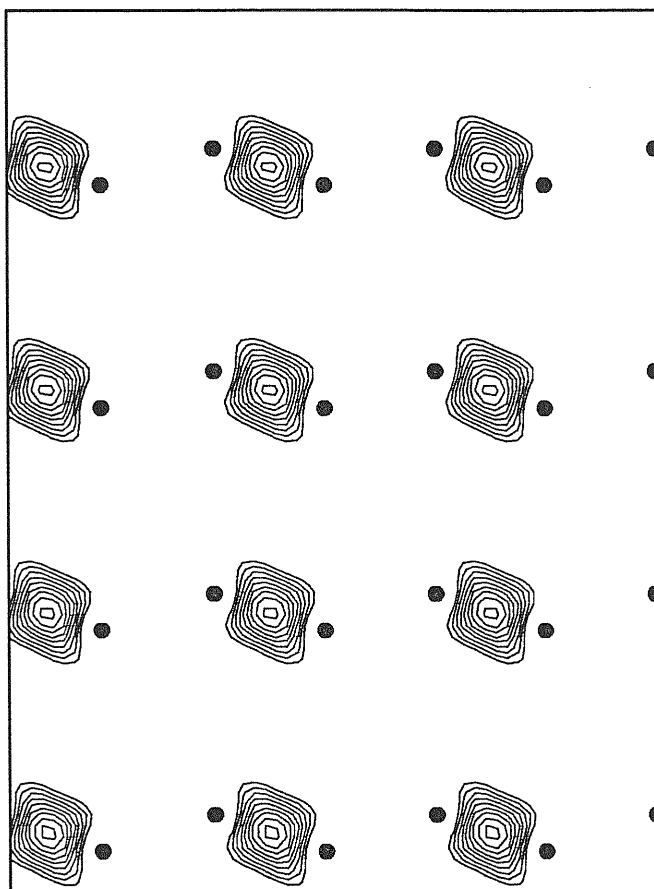

Figure 4.15: Charge density plot on the (100) plane of a surface state in the band 8 eV below E_F in surface A at $0.11\,k_{\Delta'}$. Contour lines are separated by 0.0005 a.u.. The mirror symmetry with respect to the [100] plane produces a surface state degenerate in energy with the state plotted.

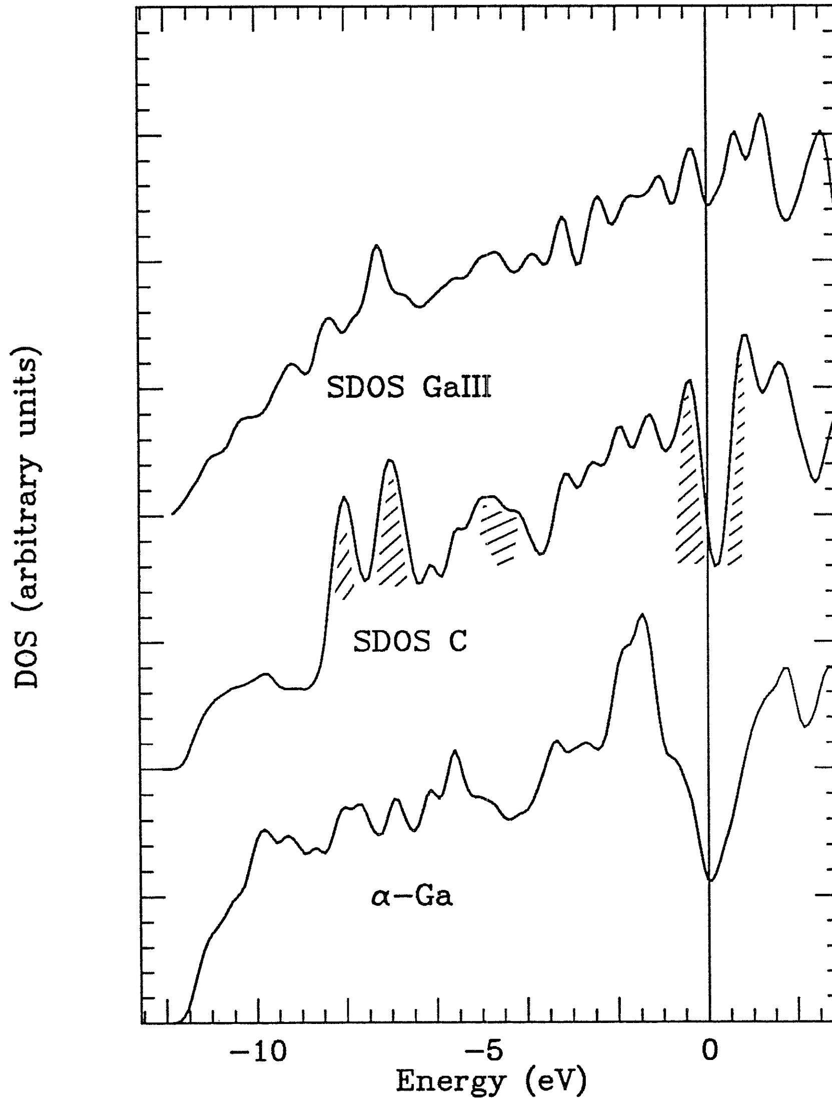

Figure 4.16: Surface projected DOS of surface C (14-layers slab), and of a relaxed 11-layers slab of epitaxial GaIII. The DOS projected on the center layer of the slab of α-Ga (bulk DOS, cfr. fig. 3.8) is also shown. The layer-resolved DOS have been computed with the layer-projected KS orbitals from 49 k points uniformly spaced in the ISBZ. Bands energies and projection integrals have been extended throughout the whole SBZ using the 2D version of the 3D tetrahedron method [65] (see appendix C for the relevant formula). The resulting DOS has been further convoluted with a gaussian with variance 80 meV. The SDOS of surface C is much more similar to the SDOS of epitaxial GaIII than to α-Ga bulk DOS. Compare also to the DOS of bulk GaIII in fig. 3.8.

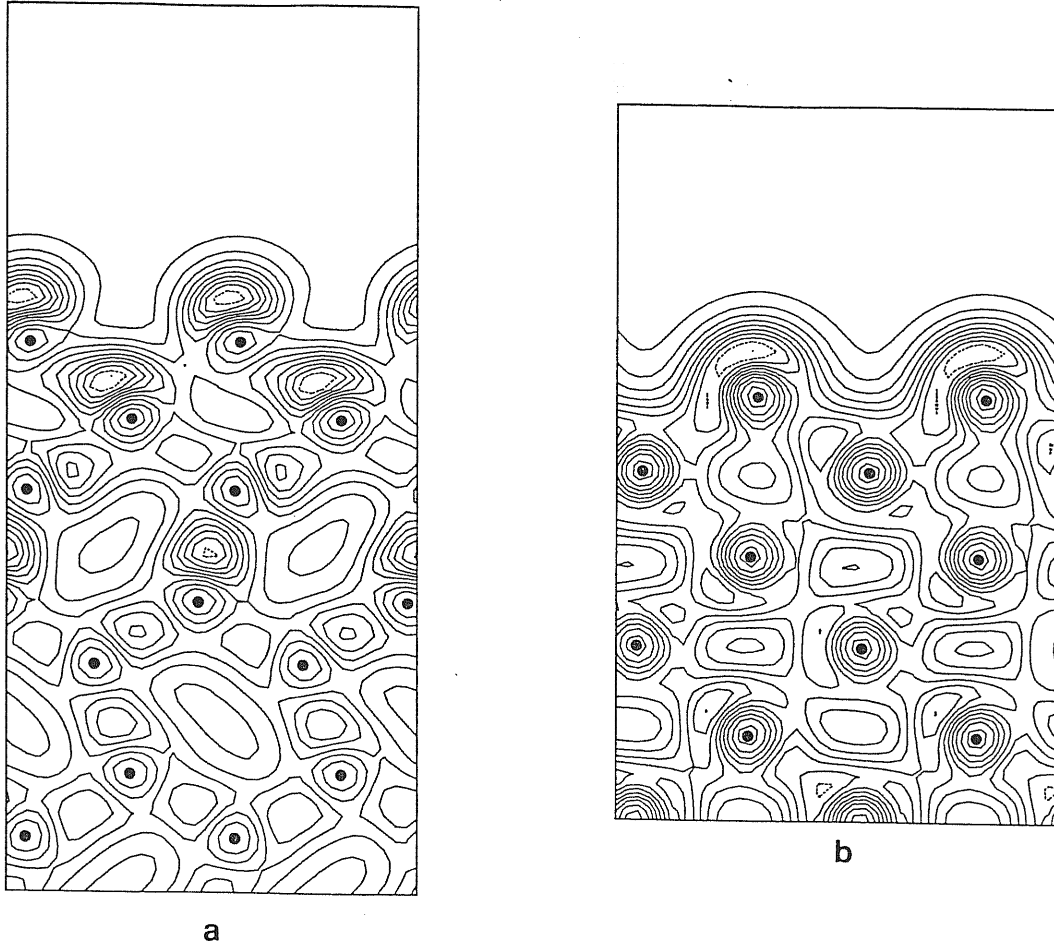

Figure 4.17: a) Charge density plotted on the (100) plane, collected from KS orbitals in the range (-0.5, 0.) eV of surface C (from 49 k points in the ISBZ). The charge density is normalized to its maximum value , and contour lines are separated by 0.1. Dotted lines indicate high charge density. b) the same as in a) for the slab of epitaxial GaIII.

as we can see in fig. 4.16. However a remnant of the α-Ga pseudogap is still present in SDOS of surface C, the two large peaks just above and below E_F in SDOS of surface C do not completely fill the pseudogap. The charge density collected from the KS orbitals in the energy regions of the latter peaks in the SDOS are plotted on the (100) plane in fig. 4.17 and 4.18 for surface C and for the surface of a relaxed slab of epitaxial GaIII. The peaks in SDOS of surface C just below and above E_F are produced from states (mainly near Γ point) extending throughout the GaIII film, while in slab of epitaxial GaIII there are only small surface resonances in these energy regions (cfr. figs 4.17 and 4.18).

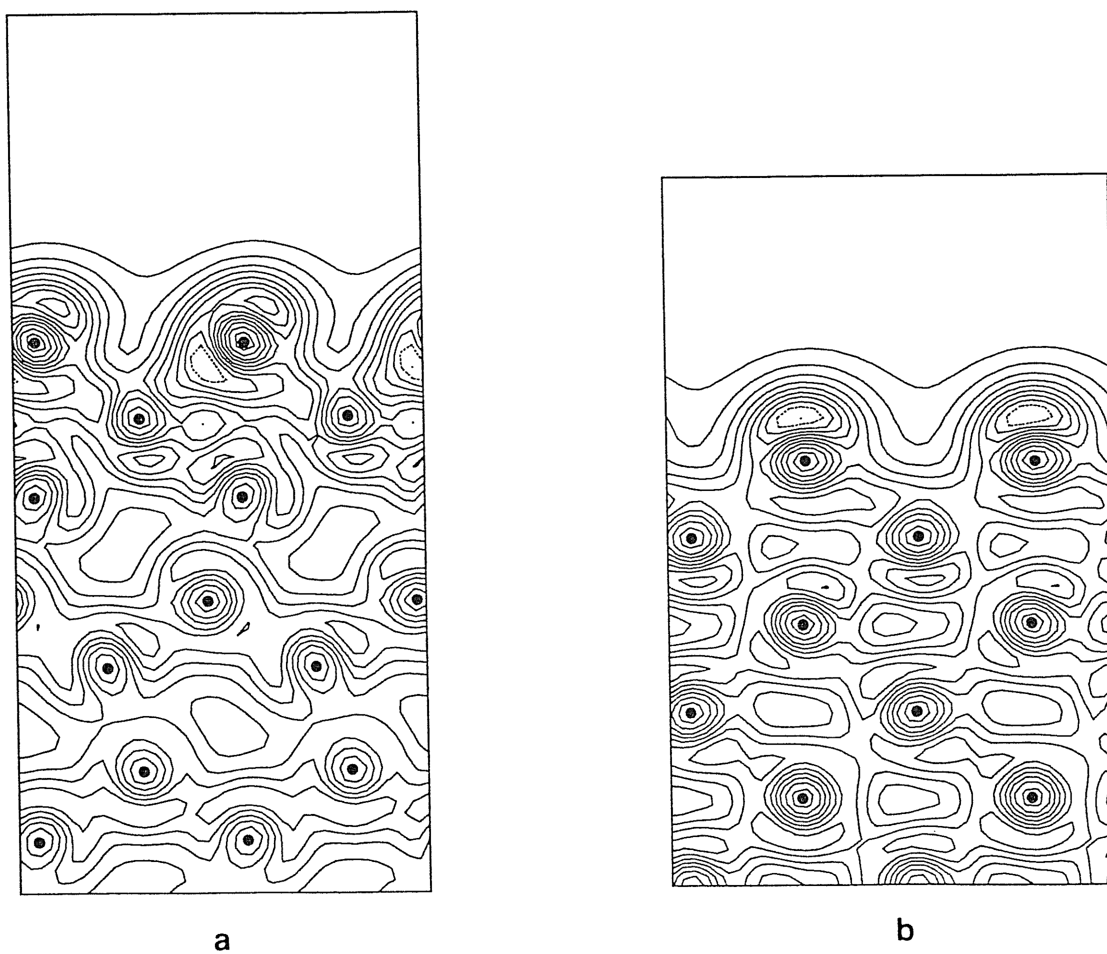

Figure 4.18: The same as in fig. 4.17 for the energy range (0.5,1.0) eV for a) surface C, and b) epitaxial GaIII.

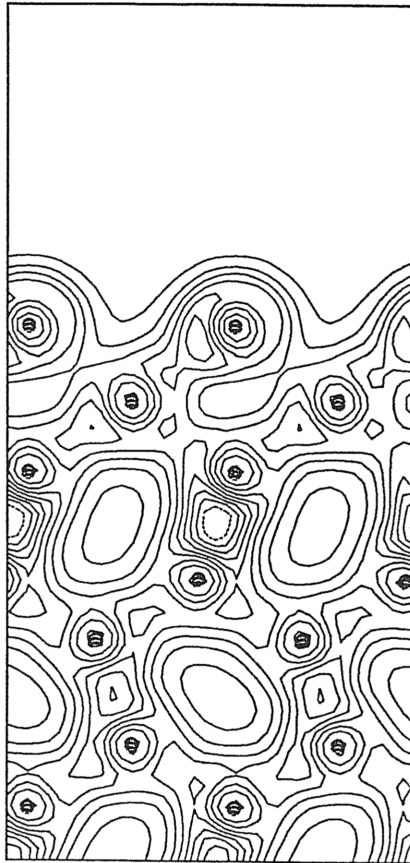

Figure 4.19: The same as in fig. 4.17 for the energy range (-4.5,-4.0) eV for surface C. The maximum of the charge is localized in the bond of the outermost dimer of α-Ga at the α-Ga/GaIII interface. The bulk forbidden states in this energy window are interface states.

The surface states 5-4 eV below E_F (cfr. fig. 4.11) in surface C, are localized in the bond of the outermost dimer of α-Ga at the α-Ga/GaIII interface, as one clearly recognize in fig. 4.19. They are interface states. Conversely the surface states in the range 7-8 eV below E_F are localized mainly on the outermost plane midway the two surface atoms along the [100] direction. Two representative states are shown in figs. 4.20 and 4.21.

Note also that the peak in the bulk DOS around 2 eV below E_F, which gives the maximum contribution to the bond charge of the dimers in the bulk α-Ga, is strongly smoothed in the SDOS of surface C in fig. 4.16, as a further indication of the disappearance

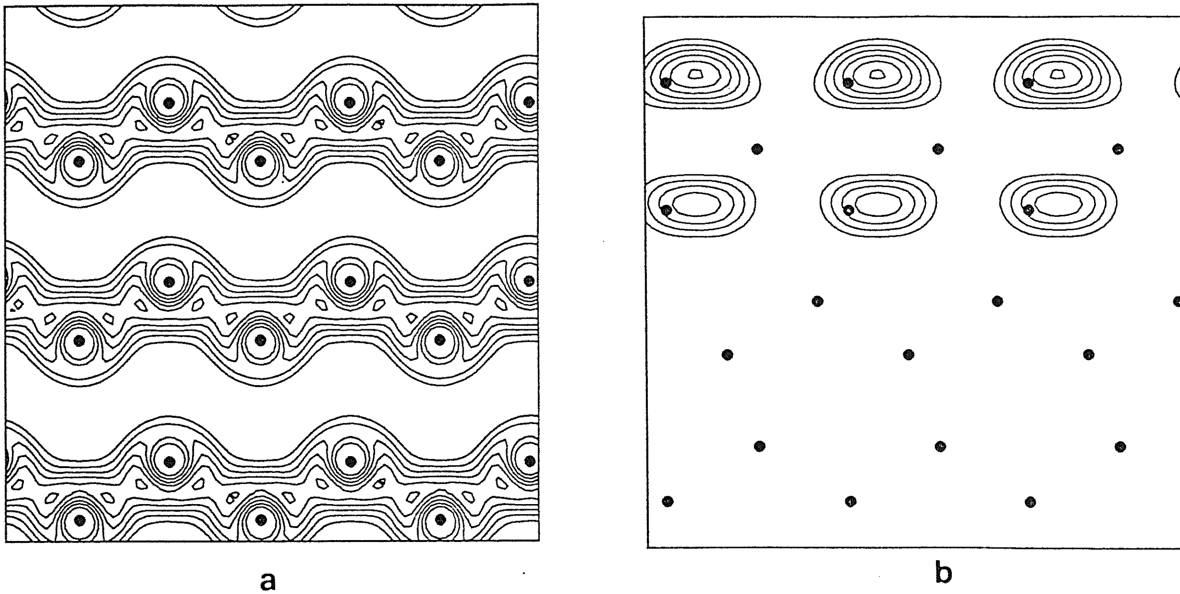

Figure 4.20: Charge density of a surface state of surface C, belonging to the bands 8 eV below E_F at $0.22\,k_T$. a) (001) plane. b) (100) plane at x=0.25. The dots correspond to atoms lying on the (100) plane at x=0. Contour lines are separated by 0.0002 a.u..

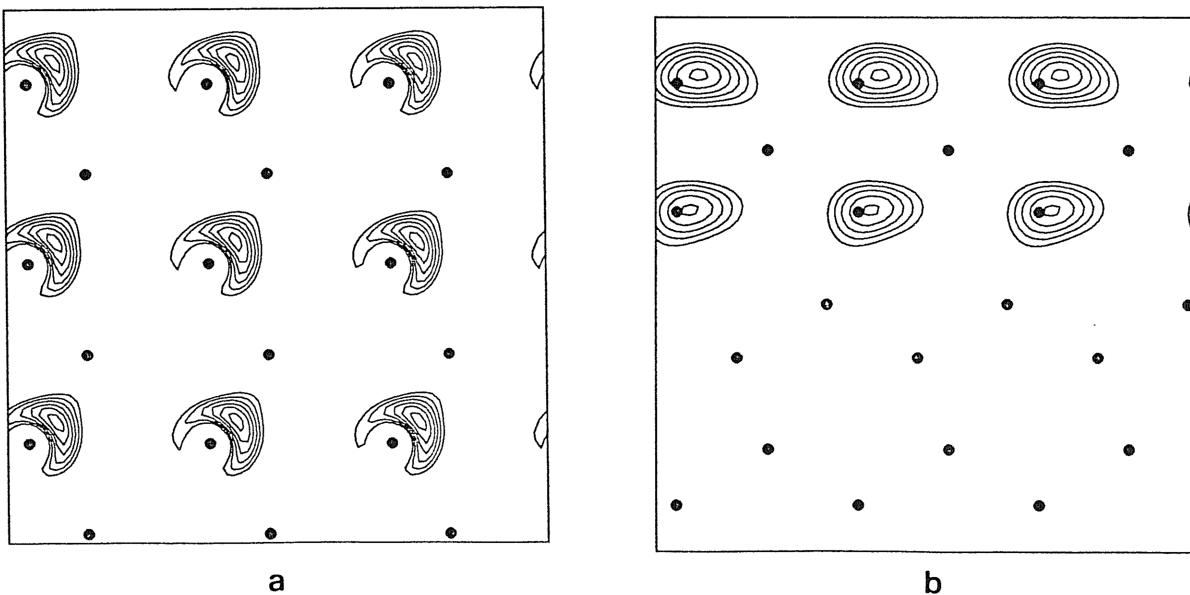

Figure 4.21: The same as in fig. 4.20 for a surface state in the band 7 eV below E_F at $0.33\,k_{\Delta'}$. a) (001) plane. b) (100) plane at x=0.25. The dots correspond to atoms lying on the (100) plane at x=0. A state degenerate in energy with the state plotted is obtained by applying a reflection with respect to the [010] plane followed by the fractional traslation (a/2,a/2,0). Contour lines are separated by 0.0002 a.u..

in the GaIII film of the covalent bonds typical of α-Ga.

Summarizing we have seen that the the presence of the GaIII film induces a large increase in the SDOS near E_F, which becomes smoother and more metallic, similar to GaIII. This "metallization" of the surface should in principle show up in photoemission measurements. The detection of surfaces states at 7-8 eV below the Fermi level in the whole SBZ in angle resolved photoemission, should be a further signature of surface C. Furthermore the residual pseudogap in SDOS of surface C is sufficiently small to account for the structureless $I-V$ spectra in fig. 4.22b, recorded with STM by Züger and Dürig [14]. The quantity plotted ($\frac{dI}{dV}/\frac{I}{V}$) is approximatively the ratio between the DOS at energy $V-E_F$ and the DOS at E_F [66]. The magnitude of the SDOS peaks just below and above E_F in surface C are roughly two times the SDOS at E_F (cfr. fig. 4.16), in agreement with the experimental $I-V$ spectra in fig. 4.22.

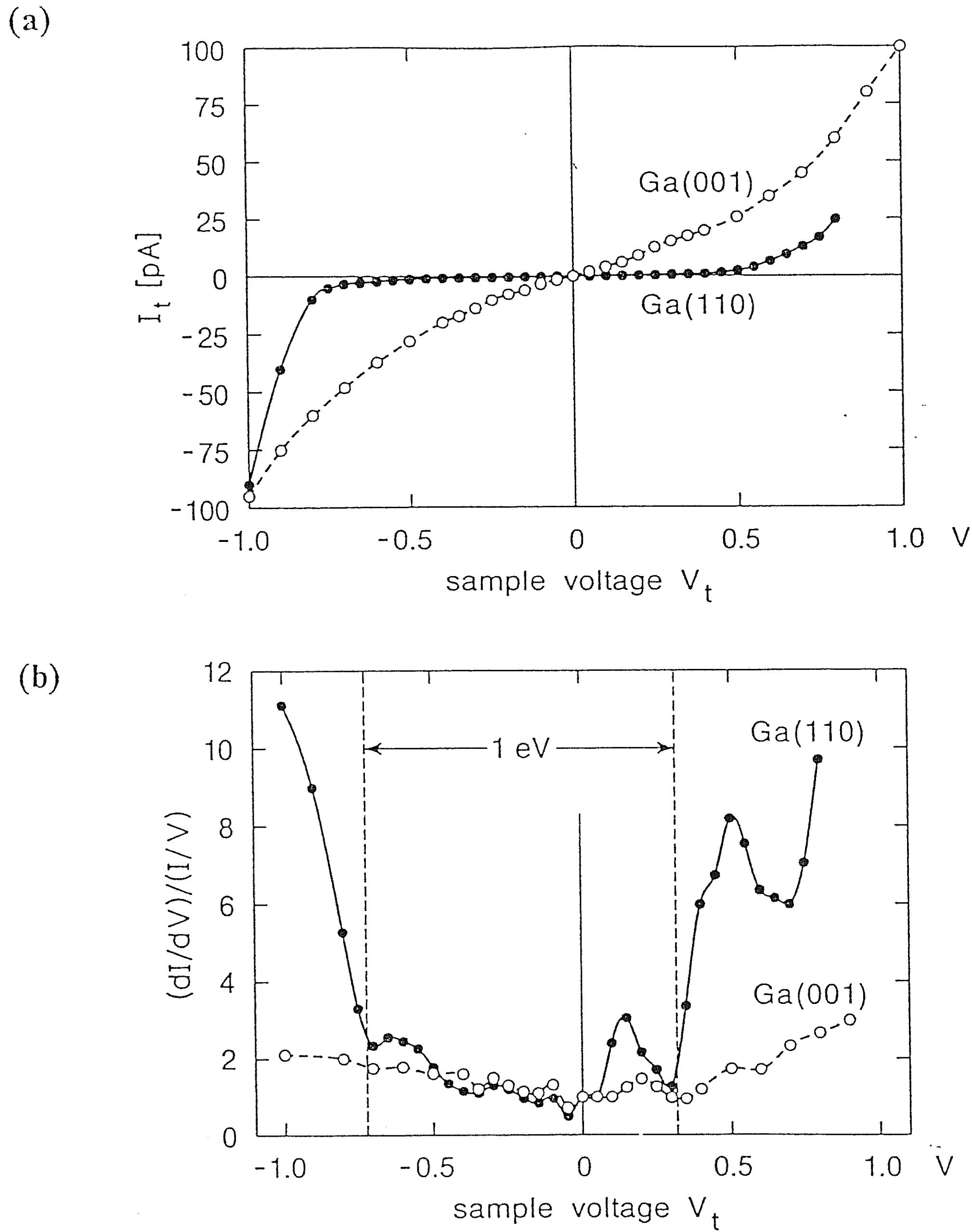

Figure 4.22: a) $I-V$ spectra measured on Ga(110) and Ga(001) surface at fix tip-sample separation with STM by Züger and Dürig [14]. On the (110) surface, the absence of the tunneling current between -0.5 and +0.4 V reveals a semiconducting character, whereas the linear voltage dependence demonstrates the metallic character of the (001) surface. b) $(dI/dV)/(I/V)$ spectra depicting the *relative* variation of the sample DOS in the vicinity of E_F. The Ga(110) shows an energy gap of approximatively 1. eV, while the DOS of Ga(001) is smooth. The figure is taken from ref. [14].

4.3 The role of metallization in the self-wetting phenomena

In the previous sections we have proposed, based on detailed ab initio calculations, that in the ground state the (001) surface of α-Ga is covered with two layers of epitaxial GaIII.

The scenario proposed is not the first realization of a "self wetting" phenomena. In general when two or more phases compete for the ground state of a bulk system there is a chance to observe the formation of a thin film of one of the losing structures at the surface of the winning bulk phase. There are known examples of this behaviour. In surface melting when the temperature is still below the bulk melting point, most crystal surfaces "self-wet" with a thin liquid film [11]. Another example is the valence transition at the surface of Sm metal, which has valence 3^+ in the bulk but becomes 2^+ at the surface, in spite of 0.26 eV/atom cohesive energy difference between bulk Sm^{3+} and Sm^{2+} [67]. These self wetting phenomena can be rationalized on the basis of a common ingredient: the emergent surface phase has a sufficiently lower surface free energy to make it worthwhile paying for the film plus interface free energy costs. The physical mechanisms underlying the surface free energy gain of the emergent phase may however have very different origin. In the case of surface melting, the surface free energy of the liquid is lower than that of the solid, mostly due to entropy [11]. In metallic Sm the surface energy of the Sm^{2+} state is lower, due to closer similarity to the divalent ground state of the free atom [67]. These surface energy gains are usually quite small, and the closeness of the bulk free energies is thus a necessary condition for the self wetting to appear.

We have seen indeed that the difference in bulk energies of epitaxial GaIII and α-Ga is small ($\Delta E \sim 5\, mRy/atom$), and the surface energy of epitaxial GaIII is sufficiently lower than surface energy of the ideal relaxed surface of α-Ga ($43\, mRy/atom$ *versus*

$57\, mRy/atom$) to pay for interface energy ($\gamma_{\alpha-III} \sim 2\, mRy/atom$) plus the difference in bulk energies for two layers of GaIII on top of α-Ga, but not for three or more. In the previous section we have seen that $\gamma_{\alpha-III}$ is so small partly due to the energy gain of the electrons transferred from the GaIII film to α-Ga, produced by the imbalance in the Fermi levels of α-Ga and GaIII. Since both the drop of Hartree potential and the structure of the interface do not depend sensibly on the numbers of GaIII layers (cfr. fig. 4.10 and table 4.1) we expect also the energy gain due to the charge transfer to be independent on the thickness of GaIII film. Therefore the $V(n)$ attraction which limits the wetting film thickness to strictly two atomic layers, can not be accounted for by a thickness dependence of the charge transfer.

At the moment the main source of the surface-interface attraction is still somewhat uncertain. From an inspection of interlayer distances in table 4.1, it does not seem that the gain in energy of surface C with respect to γ_3, and γ_4 could be explained by a better matching of the relaxation pattern of surface C with that of the free surface of GaIII, which is known to have the lowest surface energy. In other words a layering effect such as proposed by Chernov and Mikheev in the context of surface melting [68] (which should in our case be read as an interference between the relaxation pattern induced by the underlying α-Ga with the relaxation pattern induced by the free GaIII surface) does not properly correlate the data in table 4.1. There is in fact another source of surface-interface attraction: dispersion electromagnetic forces, i.e. Van der Waals interaction. When the thickness of the GaIII film covering α-Ga is much greater than the interatomic distances (which is surely not the case for our surface), macroscopic electrodynamics can be used to calculate the forces between the two interfaces. The interface-surface potential has the following asymptotic form in the non-retarded limit [12]:

$$V(n) \sim H/n^2 d^2 \tag{4.3}$$

d being the interplanar distance in the wetting film. The Hamaker constant H can be computed once the frequency dependent dielectric tensor of GaIII and α-Ga are known. H is expected to be negative, i.e. to yield attractive interaction, when the wetting film is a better conductor than the underlying solid [12]. GaIII is indeed a better conductor than the underlying α-Ga. The Hamaker constant for the α-Ga/liquid/vapor system has been explicitly computed in ref. [12], and it is $H = -3\,10^{-21} J$ for the (001) surface. We have seen in chapter 3 that GaIII is the crystalline phase, stable or metastable, obtained by cooling the liquid phase within a large range of values of pressure [2]. Moreover GaIII has an electronic density of states very similar to the liquid (cfr. 3.8 and fig. 2 in ref. [42]), so the Hamaker constant for the α-Ga/liquid/vapor system should be a good approximation for the α-Ga/GaIII/vapor system. If we use the Hamaker constant of the α-Ga/liquid/vapor system, and the surface-interface distance of our surface C in the asymptotic form 4.3 for $V(n)$, we obtain $V(2) \sim -1.3\, mRy/atom$. Strictly speaking this extrapolation of the macroscopic formula to a microscopic region is obviously not allowed, however this procedure gives us an interaction energy which is at least of the right order of magnitude. Therefore, even though this result cannot of course numerically account for the full interface attraction found, it does suggest that the large attractive deep of $V(n)$ at n=2 could be produced by the short range limit of the electromagnetic dispersion forces, which although not exactly known, must be attractive. The dispersion forces are only partially included in the LDA. The correlation effects responsible for the dispersion forces are expected to be well reproduced at short distance (LDA calculations do predict physisorption of closed shell atoms on metal surfaces), but they are not included at large

distances (for istance, LDA does not reproduce the image-like tail of the effective potential out of a metal surface), so if the main contribution to $V(n)$ were due to dispersion forces as we tentatively propose, our LDA results should underestimate the VdW attraction for configurations with a larger number of GaIII layers. It is difficult, unfortunately, to separate a specific term out of the cumulated total energy of our LDA calculation and this suggestion is therefore speculative, at least at the time being [10]. The two puzzling questions raised in the energetic of the wetting process, namely why $\gamma_{\alpha-III}$ is so small and why $V(n)$ is so attractive might thus both be accounted for by the metallization of the surface induced by the GaIII film.

The experimental data available to confirm or put in question our overall wetting scenario for α-Ga(001) surface are limited to the STM measurements by Dürig and Züger. Our results imply that the wetting with GaIII is confined to the first two surface layers up to T_m, consistently with the measured step-height distribution. The theoretical STM picture compares qualitatively well with the experimental one (see fig. 4.8), except for the chain dimerization apparent in experimental STM, and not reproduced by our calculation. In this respect we remark that the maximum of the current spots in STM do not necessarily coincide with the atomic positions, so that the dimerization inferred from STM could be magnified with respect to the true geometry. Moreover we have already mentioned that the buckling alone (anyway absent in our surfaces A, B and C) should be sufficient to activate in LEED the (2n+1, 0) spots, observed experimentally [13], and silent in the geometry of surface C. At the moment we are not able to clarify this point. Perhaps the interatomic distances along the chains in the [100] direction are too small to favour the dimerization, due to the 3% error in the theoretical lattice constant (see chapter 3). We indeed found, in

[10] Anyway, we expect the difference γ_C - γ_3 to be much smaller in an Hartree-Fock calculation, where correlation and consequently VdW interaction are absent.

a forcibly dimerized configuration of surface C, that by artificially expanding (contracting) the lattice parameter by 3 % with respect to theoretical equilibrium value, the forces which act to remove the dimerization undergo a 35 % reduction (43 % increment) [11].

A decisive test of our picture should of course come from structural tools, such as ion scattering, dynamical LEED, X-ray or atom diffraction, which should be able to discriminate between A, B, and C structures, and to eventually confirm and quantify the chain dimerization observed in STM. Static LEED is not sufficient to discriminate between A, B and C surfaces, since the 2D space group is the same for all these configurations.

Indirect tests of our proposed geometry should come from electron spectroscopy, which should reveal the "metallization" produced by the GaIII film, as we have discussed in the previous section. The GaIII film should induce also detectable modifications in the phonon spectra: the bulk phonon modes around 7 Thz [38], associated to the stretching of the dimer covalent bond, should be absent or strongly modified in the surface projected phonon density of states.

Finally, we may wonder whether this kind of solid-state incomplete wetting is a peculiar feature of α-Ga(001) surface or could be envisaged for other solids too. In general the presence of half-filled dangling bonds makes the surface energy of unreconstructed semiconductors higher than the surface energy of metals with respect to their cohesive energy (E_{coh}). The surface energy of metals are typically 0.2 E_{coh} [69], while the surface energy of covalent semiconductors are usually higher. For example the theoretical surface energies of Si(111) ideal and 7x7 reconstructed surfaces are 0.26 E_{coh}, and 0.24E_{coh} respectively [70]. If a simple reconstruction, still preserving the "covalent bonding" is not feasible, then the wetting with a fully metallic phase should in principle be favoured. This seems

[11] A full relaxation of the dimerized configuration with expanded lattice parameters ends up with a still undimerized chain, due perhaps to the larger compression of the outermost layer induced by the artificial in-plane expansion.

to be the case for the α-Ga(001), where the plausible structure of the ideal surface (B) does retain covalent unsaturated dangling bonds.

5 The α-Ga(010) Surface

5.1 Surface Structure

As reported, for instance, in ref. [35, 14] the (010) orientation is not present on α-Ga single crystals as grown from the melt. Instead four small facets all belonging to the family of lattice planes indexed $\{121\}$ are formed in the vicinity of the (010) orientation. The (010) surface must be prepared from cutting of the crystal. Its structure expected from the truncated bulk is shown in figure 5.1. The surface unit cell contains one atom, the Ga_2 dimers being oriented out of the surface plane by an angle $\theta = 16.9^0$, all in the same direction. An atomically resolved STM image of the (010) surface, recorded by Züger and Dürig [14], is reproduced in fig. 5.2. The best resolution of the image were obtained with tunnelling parameters $I_t = 5\,nA$, and $V_t = +50\,mV$, i.e by imaging empty electronic states of the sample. The symmetry observed with STM is essentially in accordance with that expected from the truncated bulk in fig. 5.1. However Züger and Dürig recognized a slightly different contrast of the spots on the edges and in the center of the marked cells in fig. 5.2, and suggested the possible occurrence of a 1x2 reconstruction.

Although the absence of the (010) orientation in single crystal suggests an high surface free energy $\gamma_{sv}^{(010)}$, large terraces extending over several 100 Å are present after sputter-cleaning cycles of the sample. Moreover the step structure is stable up to T_m. No dynamics

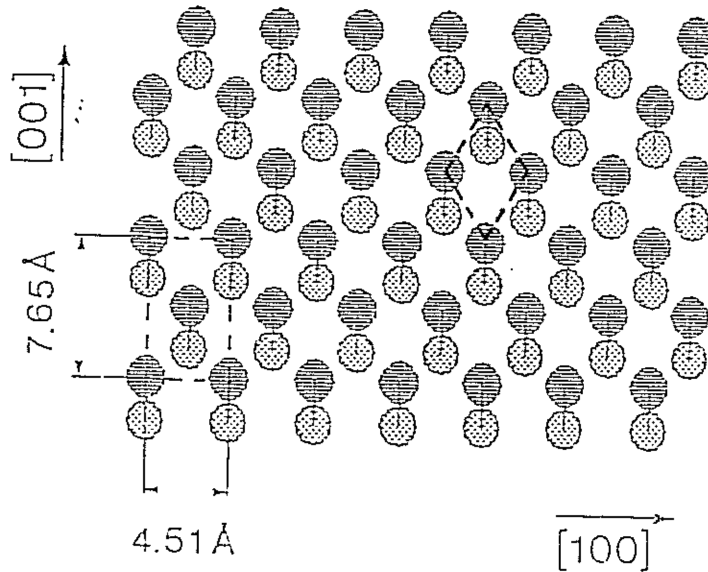

Figure 5.1: Truncated bulk structure of the (010) surface. The Ga_2 dimers are oriented out of the surface plane by 16.9^0 (indicated by different shading). The ideal rhombohedral surface unit cell in depicted by dashed lines. The dashed rectangle denotes a conventional unit cell, two times larger than the ideal rhombohedral surface unit cell. The figure is taken from ref. [14].

such as roughening or diffusion at steps edges was observed with STM up to the onset of bulk melting [14]. Thus the (010) surface presents a thermal stability similar to (001) surface, although the latter is even stable when macroscopic amounts of the underlying bulk are already molten. These properties immediately suggest a possible self-wetting of α-Ga(010) surface with a GaIII film stable above the bulk melting point of α-Ga, as we proposed for the (001) orientation in the previous chapter. The geometry of the (010) surface still permits an epitaxial growth of a tetragonally distorted FCC film on top of α-Ga. However the in-plane lattice constants are much larger on the (010) surface than on the (001) one (cfr. figs 5.1 and 4.3b), which cause a GaIII film covering the (010) surface to be unstable with respect to the formation of dimers similar to those of bulk α-Ga, as we have explicitly checked by a slab calculation. The final relaxed configuration of the slab presents an implausible large corrugation and a very high surface energy. This way

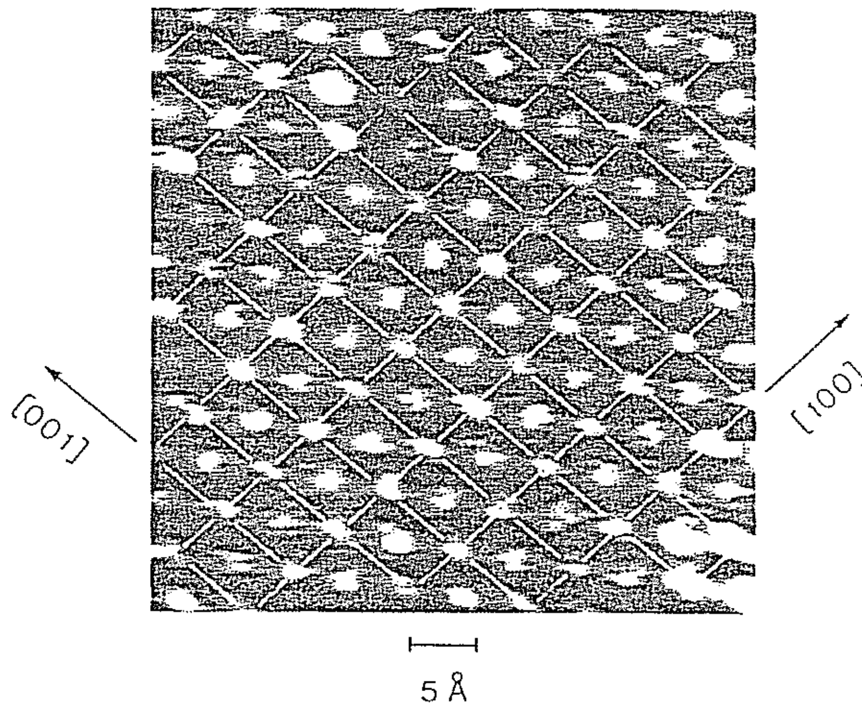

Figure 5.2: Atomically resolved STM image (46 Åx 42 Å) of the (010) surface displaying $\partial ln I_t / \partial x$ signal, (essentially $\partial z/\partial x$) measured by modulation technique [14]. The tunnelling parameters are $I_t = 5nA$, and $V_t = +50mV$ (positive voltage corresponds to imaging empty states of the sample). The corrugation calculated from this signal is 0.01 Å. The rectangular unit cells (cfr. fig. 5.1) are indicated by marked rectangles (slightly distorted by piezo-shift). The figure is taken from ref. [14].

can not be pursued, and then we explored the properties of the ideal surface.

As for the (001) orientation, the ideal (010) surface can be formed in two ways, by cutting the crystal at a plane without cutting the dimers (surface A), or at a plane cutting the Ga_2 dimers (surface B). In configuration A three metallic bonds per atom are broken, while two metallic bonds and one covalent bond per atom are broken in configuration B. On the basis of the simple bonds counting argument we expect surface A to be favoured. This is exactly what it turns out from our slab calculations. We fully relaxed slabs 16-18 layers thick for both A and B geometries. Convergency in k-sums were tested up to 36 points in the ISBZ, simple gaussian spreading technique has been used. Residual atomic forces in relaxed slabs were less than $2\, mRy/a_o$.

The surface energies (γ_A) for unrelaxed and relaxed surface A are 97 and 79 $mRy/atom$ respectively. The surface energies are converged within $\pm 1\, mRy/atom$ with respect to k-sums in ISBZ. However γ is strongly dependent on the k-point mesh used for the computation of the bulk energy (E_{bulk}) to be subtracted from the total energy of the slab. By using E_{bulk} obtained from k-point sampling in the bulk BZ, corresponding to 12-layers and 20-layers slabs we obtain a $7\, mRy/atom$ difference in γ. The choice of the k-point mesh in the bulk BZ "equivalent" to the slab geometry is more critical for the (010) surface than for the (001) one, due to the larger dispersion of electronic bulk bands along [010] than along [001] direction. This uncertainty does not affect much the comparison of the surface energies of different slabs with the same orientation, but it does affect the analysis of the anisotropy of surface energy, i.e. for example $\gamma^{(010)} - \gamma^{(001)}$. The values reported in the text for $\gamma^{(010)}$ refer to E_{bulk} calculated with a k-point mesh corresponding to a 12-layers slab, i.e. the geometry closest to the physical slab used for the surface calculation without the outermost dimer layer. The charge density on the (100) plane for surface A (18-layers slab) is shown in figure 5.3.

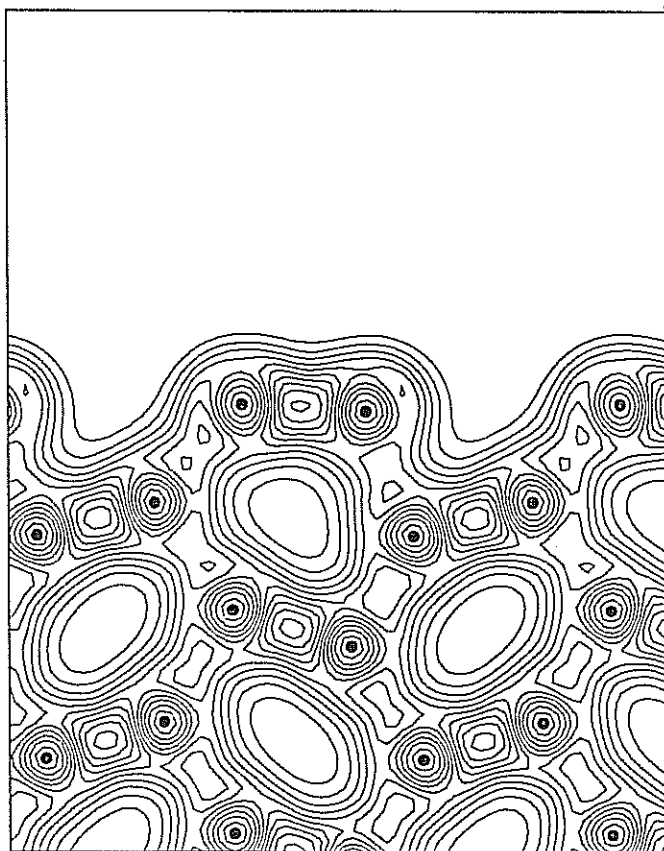

Figure 5.3: Charge density of surface A (ground state of (010) orientation) plotted on the (100) plane passing through all atoms shown. Note the decrease of the angle between the outermost dimer and the surface plane. Contour lines are separated by 0.005 a.u..

Surface B is obtained by removing the outermost atom of the surface dimers in fig. 5.3. The resulting surface has an exceedingly large corrugation. A better surface is obtained by moving the lone outermost atom in the hole underneath, midway the dimers of the second layer in fig. 5.3. By fully relaxing this configuration we ended up with a surface energy $\gamma_B = 85\, mRy/atom$, still higher than $\gamma_A = 79\, mRy/atom$. *Then we propose the structure in fig. 5.3 as ground state configuration of α-Ga(010) surface* .

Note in fig. 5.3 the decrease of the angle θ between the surface dimer and the surface plane from 16.9^o down to 2.8^o. The length of the surface dimer is equal to the bulk one, while the dimer in the second layer is 1 % contracted, and inclined by $\theta = 15.4^o$ ($\theta_{bulk} = 16.9^o$). A possible small difference in $\theta's$ angles of the two surface dimers in the rectangular unit cell in fig. 5.1 could be responsible for the asymmetry observed by STM [14]. Up to now we have not explored this possibility. The rotation of the surface dimer reduces the charge corrugation and is responsible for the large energy gain obtained by relaxation. Both atoms of the dimer lie nearly on the surface plane, and the atomic density of (010) surface is so $12.4\, nm^{-2}$, even larger than those of the (001) surface ($10.5\, nm^{-2}$, the theoretical lattice constants have been used). γ_A expressed in energy per unit area is $4.9\, mRy/\text{Å}^2$ for the (010) surface, equal within our error to the surface energy of our proposed ground state for the (001) orientation (surface C in the previous chapter). This result is not too surprising, given the similarity of atomic densities of surfaces (001) and (010). The absence of the (010) surface in the shape of single crystal grown from the melt could be due to growth kinetics which favour the other local minima in the polar plot of $\gamma_{sl}^{(hkl)}$.

Although the surface dimer is nearly parallel to the surface, the innermost atom of the dimer is not visible in the theoretical STM image (cfr. fig. 5.5), in agreement with the experimental image in fig. 5.2. Furthermore the largest corrugation in the theoretical STM

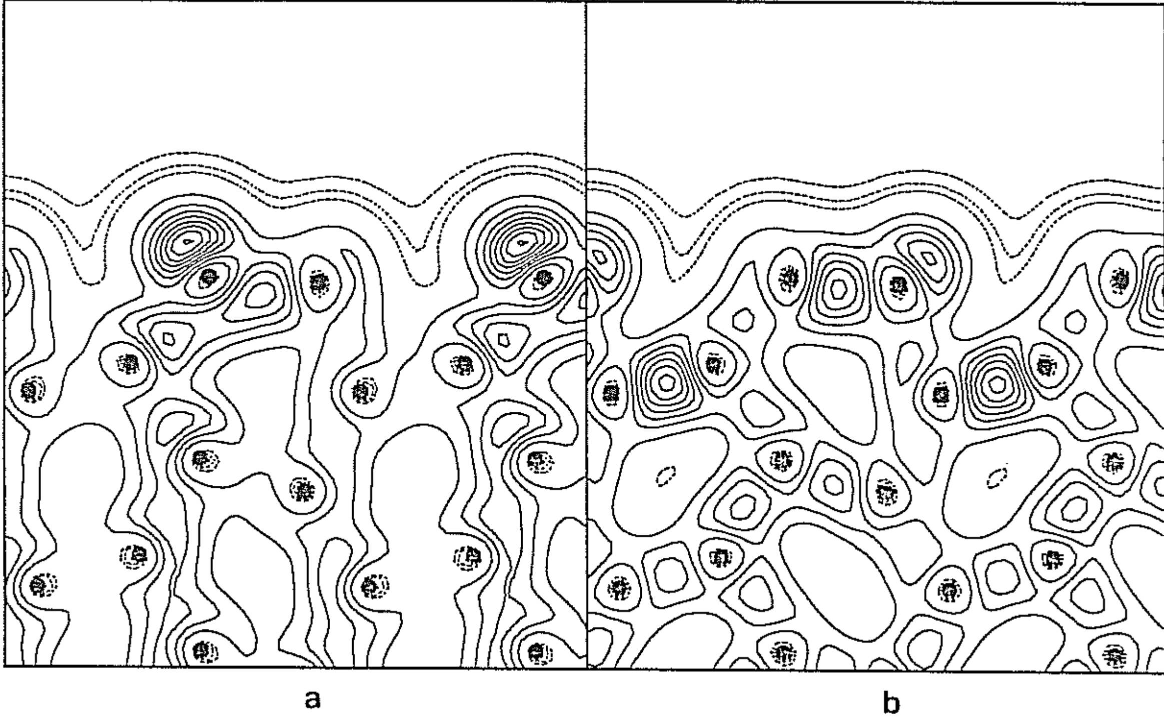

Figure 5.4: Charge density of ground state configuration of (010) surface plotted on the (100) plane, including states inside an energy window 0.5 eV wide above E_F (panel a), and below E_F (panel b). 52 k points uniformly spaced in the ISBZ are used. Continuous contour lines are separated by $3.8 \cdot 10^{-4}$ a.u., while dashed lines are separated by $5.8 \cdot 10^{-5}$ a.u., the lowest density being $5.8 \cdot 10^{-5}$ a.u.. The charge accumulation above the outermost atom in a) is produced by empty surface states (cfr. fig. 5.6).

picture is obtained by imaging empty electronic states, still in agreement with experimental results [14]. The reason for this latter property is clear by looking at the charge density collected from KS orbitals in the energy ranges (-0.5,0) and (0, +0.5) eV around E_F in fig. 5.4. The protrusion of charge above the outermost atom in fig. 5.4a is produced by a band of unoccupied surface states just above E_F (see fig. 5.6 in the next section).

The tip-surface distance in the real STM device is usually $5 - 8$ Å, while the outermost contour line in fig. 5.4 is located 3 Å above the surface, since the *ab initio* charge density is not well described at larger distances. In order to compute the STM image at large distances within the Tersoff-Hamann approximation we have extrapolated the tails of the KS orbitals by matching the KS orbitals of the slab calculation to their expected

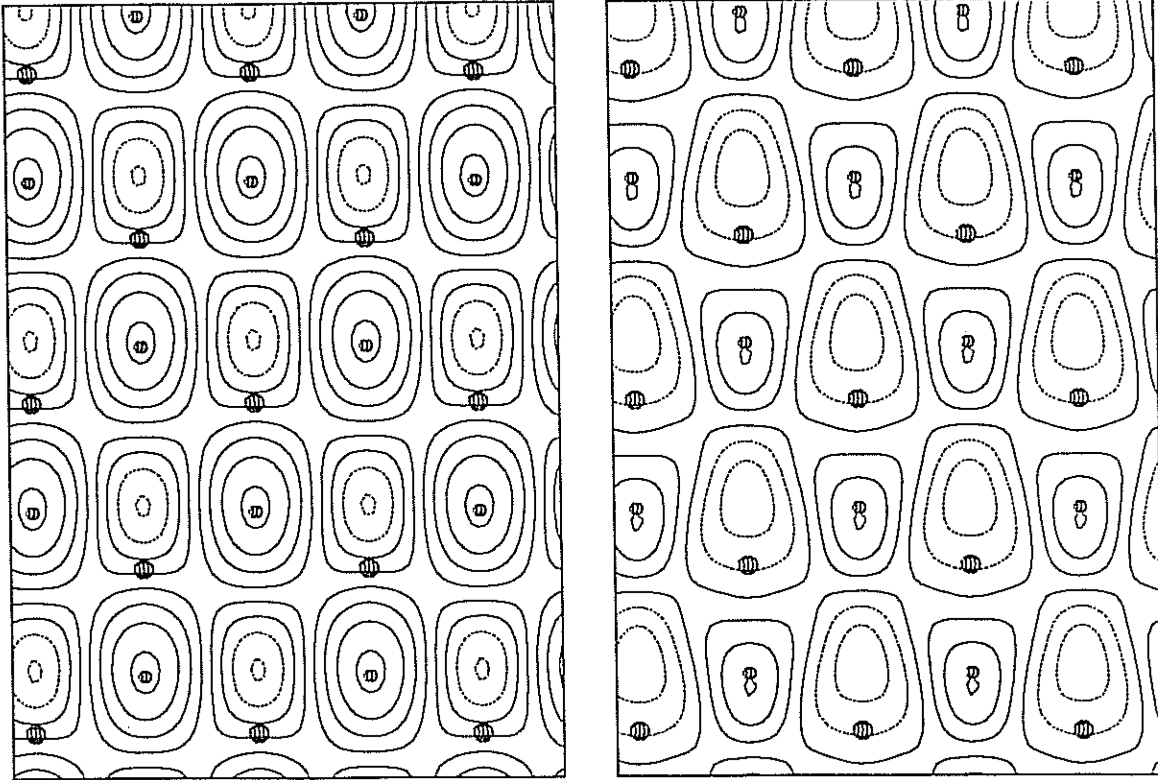

Figure 5.5: Theoretical STM image for fixed 5 Å tip-surface separation, obtained by the extrapolation of KS orbitals tails, including states inside an energy window 0.5 eV wide above E_F (left panel), and below E_F (right panel). 52 k points uniformly spaced in the ISBZ are used. The matching point between KS orbitals of the slab calculation and their expected asymptotic decay (see appendix C) is 1.3 Å above the surface. The image with a matching point 3 Å above the surface is not sensibly different. Dashed lines indicate high charge density. The outermost atoms of the dimers are depicted by larger dots.

asymptotic decay as described in appendix C. The resulting theoretical STM image 5 Å above the surface is plotted in fig. 5.5, including states inside an energy window 0.5 eV wide above (panel a) and below (panel b) E_F.

In contrast to fig. 5.4, at 5 Å far from the surface the maxima of charge density are always above the outermost atom of the dimer, both imaging empty and filled electronic states in figs. 5.5a and 5.5b. Thus the image is not expected to change qualitatively by changing the sign of tunnelling voltage. However the corrugation predicted by our calcu-

lations is still 20-30 % larger by imaging empty states, in agreement with the experimental evidence. Conversely by increasing further the tip-surface separation above 8 Å, our results predict the largest corrugation to be obtained by imaging filled states. Moreover in fig. 5.5 the minima of the charge are along the [100] direction, midway between the maxima, while a saddle point is present along the [101] line connecting the maxima; this feature is in agreement with the experimental results [71].

5.2 Surface Electronic Properties

The slab band structure of ground state configuration of the (010) surface is reported in fig. 5.6 along the high symmetry lines of the ISBZ.

We can recognize surface states in three energy regions: (i) empty surface states just above E_F near the bulk bands edge along the T direction, (ii) filled surface states in the small gap 3 eV below E_F, midway along T, and (iii) filled surface states 5-7 eV below E_F along T' and Σ. The charge density of representative surface states in the three energy regions (i), (ii), and (iii) is plotted in panel a, b, and c of figure 5.7 respectively.

The surface states just above E_F in fig. 5.7a are strongly localized above the outermost atom and in middle of the surface dimer bond. This surface band is responsible for the enhanced corrugation observed in STM by imaging empty states, as discussed in the previous section. The surface state around 3 eV below E_F in fig. 5.7b is strongly localized between the second and third dimer layers, the distance between the two atoms "bonded" by the surface state in fig. 5.7b being 5% lower than the corresponding bulk one. The surface state in fig. 5.7c, belonging to the surface band 5-7 eV below E_F is strongly localized along the bond of the two outermost dimers. The surface states (i) and (iii), strongly localized on the surface dimers, show up clearly in fig. 5.8 by comparing the SDOS with the DOS projected on the center layer of the slab. Surface states are indicated

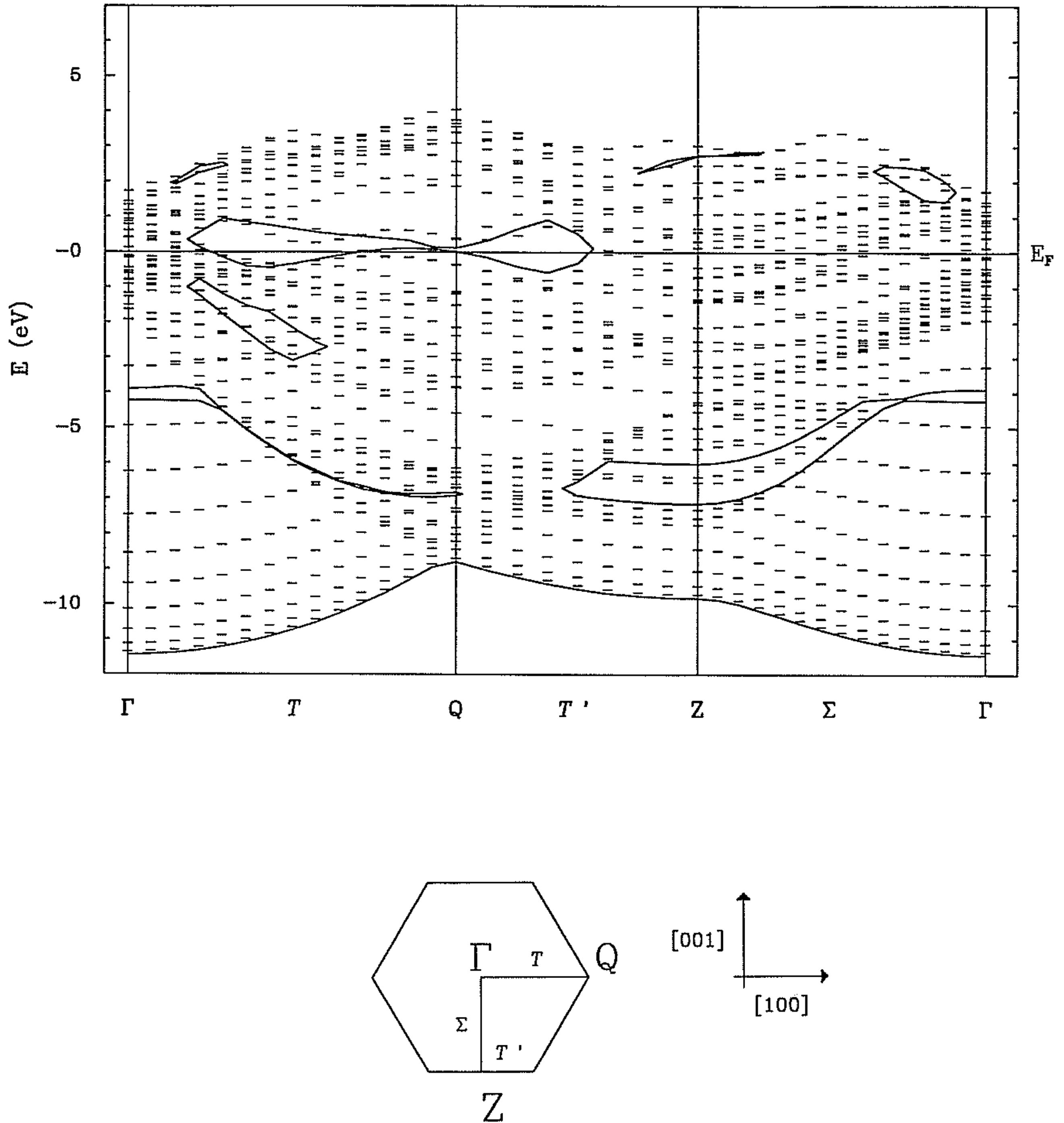

Figure 5.6: The surface band structure of (010) surface (cfr. fig. 5.3) from a 18-layers slab. Continuous lines represent the band edges of the surface projected band structure of the bulk. The zero of energy corresponds to the Fermi level. The energies of bulk and slab calculations are aligned by matching the average Hartree potential in the bulk and at the center of the slab. Inset: Irreducible Surface Brillouin Zone for the (010) surface.

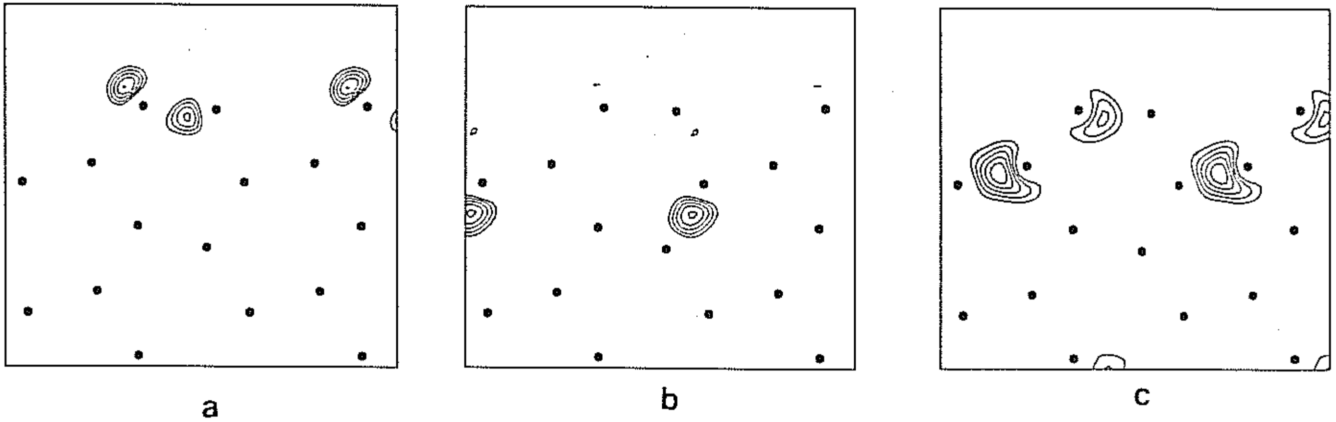

Figure 5.7: a) Charge density of the state at $0.5\,k_T$ of the surface band just above E_F. b) Charge density of the state at $0.5\,k_T$ of the surface band 3 eV below E_F. c) Charge density of the state at $0.83\,k_\Sigma$ of the surface band 5-7 eV below E_F. Contour lines are separated by 0.0005 a.u..

by shaded areas.

Concluding this section we remark that no indication of surface instability as produced, for instance, by half-filled surface states comes out from the analysis of the band structure, further supporting our proposed ground state geometry.

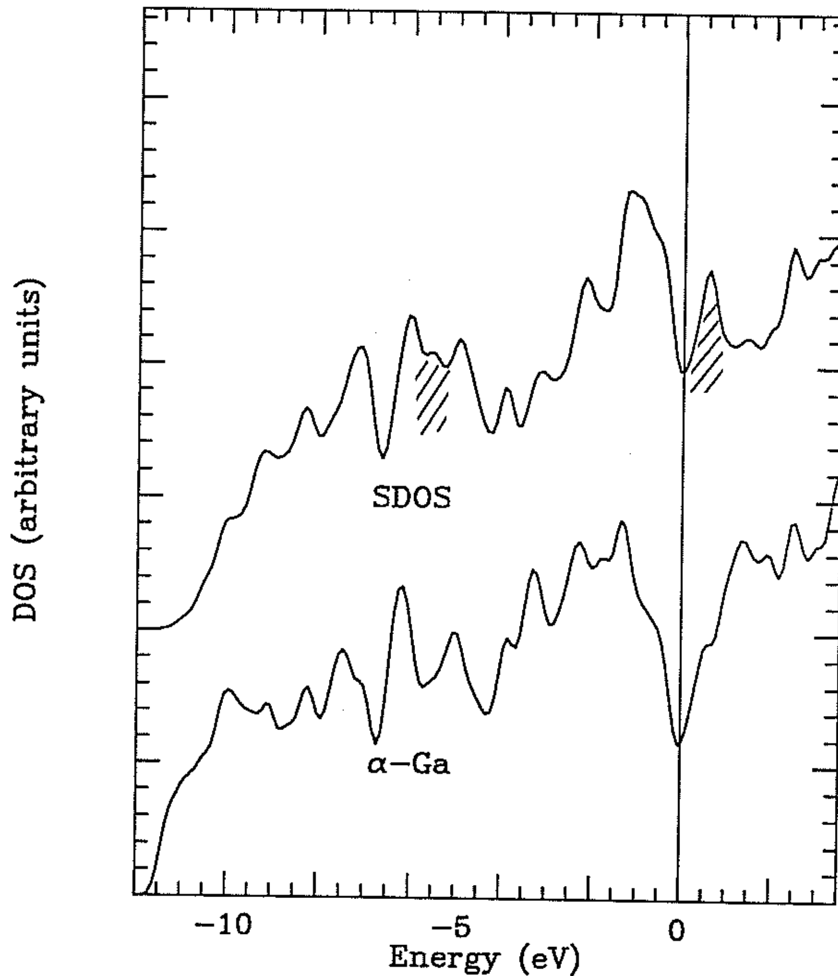

Figure 5.8: Layer-projected DOS for (010) surface (18-layers slab). The upper curve is the DOS projected on the surface layer, while the lower curve is the DOS projected on the center layer of the slab. The layer-resolved DOS have been computed with the layer-projected KS orbitals from 52 k points uniformly spaced in the ISBZ. Band energies and projection integrals have been extended throughout the whole SBZ using the 2D version of the 3D tetrahedron method [65] (see appendix B for the relevant formula). The DOS projected on the center layer of the (001) oriented slab reproduces better the bulk DOS (cfr. 3.8 and fig. 4.16) than the bulk-projected DOS reported in this figure, due to a larger dispersion of the bulk bands along the [010] direction than along the [001] direction.

5.3 Discussion

As suggested by the simple counting of bonds broken at the surface, the configuration without broken dimers is favoured on (010) surface. The resulting large corrugation of the ideal bulk termination is reduced by the rotation of the surface dimers, which is possible on the (010) surface, since all surface dimers are oriented in the same direction. Conversely the corrugation of the analogous configuration A of the (001) surface cannot be reduced through the same mechanism since there the adjacent dimers should rotate in opposite directions. On the (001) surface the adjacent atoms in the chain along [100] become closer and closer by rotating the dimers, and their mutual repulsion finally hinders further rotation stabilizing the unfeasible relaxed configuration A in figs. 4.5a and 4.6a. Therefore on the (001) orientation the plausible ideal configuration is surface B, obtained by breaking the surface dimers. Conversely, on the ideal (010) surface no surface dimers are broken, and therefore no unsaturated dangling bonds are present as driving forces for a large atomic rearrangement. These arguments account for the reconstructing and non-reconstructing behaviour we have found on (001) and (010) surfaces.

The absence of surface mobility also on the (010) orientation near the bulk melting, as detected by STM, cannot be justified by a self-wetting scenario similar to that suggested for the (001) surface in the previous chapter. However we remark that although the melting point of α-Ga is much lower than those of most other metals, the potential barriers to be overcome for adatom diffusion are probably not so much lower. Therefore adatom diffusion could be very low up to T_m for *all* gallium surfaces. Besides, another effect decreasing the surface mobility could be at work specifically of the (010) surface. Namely, since the diffusion of the whole surface dimer is probably unfavoured, the surface mobility should be mainly due to single atom diffusion which requires the dissociation of surface

dimers. The dissociation energy of a surface dimer E_{diss} can be estimated from our results as $E_{diss} = 2(\gamma_B^{(010)} - \gamma_A^{(010)}) = 1905K$. An upper estimate for the dissociation entropy S_{diss} comes from the value of the melting entropy of α-Ga ($S_m = 2.23$) [1]. Accordingly, the abundance of broken surface dimers at the melting point is expected to be as low as $n \sim exp(-E_{diss}/T_m + S_{diss}) < 1.7\%$.

[1] The melting entropy of an atom at surface is larger than the melting entropy in the bulk, but the configurational entropy of the adatom on a crystalline substrate is supposed to be lower that entropy in the bulk liquid, so $S_{diss} = S_m$ could be a good compromise.

6 Conclusions and outlooks

The flexibility of simultaneously forming two kinds of chemical bonds makes gallium a metal with peculiar properties. Our calculations essentially reproduce the previous ab initio results [9, 8] on the semimetallic phase α, showing a pile up of charge in the Ga_2 dimer characteristic of a covalent bond and its fingerprint in the electronic density of states, as a pronounced pseudogap at the Fermi level. However the hierarchy in energy of the other losing structure is largely modified in our refined calculation with respect to previous results [8], and accounts now well for the experimental results on gallium phase diagram. The less-stable fully metallic phases are very close in energy to the ground state α, all phases lying in a narrow energy window 6 mRy/atom large. Both the partial covalent character of α-Ga and the closeness in energy of the other fully metallic phases play a crucial role in the physics of α-Ga surfaces, where the relative importance of covalency and metallicity changes with respect to the bulk. We found that in one of the two possible ideal configurations of the (001) surface the covalent character of α-Ga shows up forcing the presence of unsaturated dangling bonds. As in most semiconductors the instability produced by the unsaturated dangling bonds is removed by a large rearrangement of surface geometry. We have proposed, based on detailed ab initio calculations, that in the ground state the (001) surface of α-Ga is in fact covered with two layers of GaIII grown epitaxially on α-Ga. GaIII is a denser phase stable in the bulk at high pressure and

temperature. This new realization of a "self-wetting" phenomenon is made possible by the small surface energy of GaIII, so much lower than the surface energy of ideal relaxed α-Ga surface to make it worthwhile paying for the difference in bulk energy between α-Ga and GaIII plus the interface energy. The cost of the GaIII film is indeed small due to the closeness in energy of the bulk phases, and the interface energy is reduced by the charge transfer across the α-GaIII interface connected with the 1 eV contact potential between the more electronegative α-Ga and more metallic GaIII. The metallization of the surface has been tentatively suggested to be also the source of the strong surface-interface attraction which, consistently with experimental step-distribution, limits the GaIII film to strictly two atomic layers, causing the wetting of α-Ga by GaIII to be incomplete. This surface-interface attraction could be the short-range counterpart of the long-range van der Waals interaction which is known to be attractive for a poor metal covered by a better conductor. This suggestion, however, is at the time being only speculative and to be confirmed requires a further analysis of the different terms which constitute the cumulated total energy in our calculation.

The experimental data available to confirm or put in question our overall wetting scenario for the α-Ga(001) are limited to the STM measurements by Dürig and Züger. The theoretical STM image of our proposed ground state compares qualitatively well with the experimental one, except for the chain dimerization inferred from the experimental image, and absent in our configuration. This point requires further study: from the theoretical side a test of the validity of the LDA and frozen core approximations which produces a systematic 3 % error in the equilibrium lattice constant of gallium phases should be further checked via CI quantum chemistry calculation and all-electron LDA calculation on the Ga_2 molecule. While a certain tendency to overestimate the atomic density is common in most LDA calculation, our error in the equilibrium lattice constant is somewhat

larger than usual and could be important in the fine details of the surface structure. The chain dimerization is nevertheless a minor effect with respect to our proposed atomic rearrangement which should be easily detectable by structural tools such as ion scattering, dynamical LEED, and X-ray diffraction, able in principle (as opposed with STM) to discriminate between the ideal structures and our proposed ground state.

Bulk GaIII is expected to melt above the melting point of α-Ga at the density of the film covering the α-Ga(001) surface. This argument could account for the anomalous thermal stability of the (001) surface detected with STM. Although there are now experimental [72] and theoretical [73] evidences on the possibility of superheating closed packed surfaces (e.g. Au(111) and Pb(111)), the α-Ga(001) surface presents a more pronounced stability: in STM measurements [14] it appeared even stable when macroscopic amounts of the underlying bulk is already melted. Our self-wetting scenario could therefore account for the enhanced thermal stability of α-Ga(001). Besides this peculiar behaviour of the (001) orientation, all the other surfaces studied by STM ($\langle$ 001 $\rangle$, (111), (110)) present a very low mobility up to T_m (303 K). The low diffusion at room temperature could be accounted for by considering that although the melting point of α-Ga is much lower than most other metals, the potential barriers to be overcome for adatoms diffusion and/or the energy for the creation of a couple vacancy/adatom are not probably not so much lower. An ab initio study of the energy barriers for adatom diffusion would be quite illuminating in this respect.

In contrast with the (001) orientation the (010) surface does not reconstruct. We have shown that on the ideal (010) surface there are no unsaturated dangling bonds as driving force for the reconstruction, and surface atoms therefore undergo only a minor rearrangements consisting of a 14 degrees rotation of the surface dimers.

Conversely a large atomic rearrangement is expected on the (110) surface which ap-

pears to be semiconducting in the STS measurements reported in fig. 4.23. The covalency of α-Ga should therefore prevails on this orientation. Theoretical work on the (110) surface is in progress.

In summary our study reveals interesting phenomena at the surfaces of α-Ga driven by the interplay between covalency and metallicity. We hope that these results will stimulate further experimental work on this peculiar system.

Acknowledgements

First of all I would like to express my thanks to my supervisors Prof. Erio Tosatti and Dr. Guido Chiarotti , for their guidance and encouragement during the course of this work. I am also grateful to Drs. U. Dürig and O. Züger for discussions and information. Special thanks are due to Prof. S. Baroni, Dr. M. Buongiorno Nardelli, Dr. A. Dal Corso, and Dr. P. Giannozzi for introducing me to the use of their DFT Fortran library. Discussions with most members of the Condensed Matter Group in SISSA, and in particular with Prof. R. Resta and Dr. N. Takeuchi are gratefully acknowledged.

Appendix A Non Linear Core Correction to Pseudopotential

In this appendix we describe the method used to generate a pseudopotential for Ga with the nonlinear core correction (NLCC).

In the pseudopotential formalism for total energy calculations the charge density is divided in core and valence contribution and the energy of the core is assumed to be constant and subtracted out. Furthermore the core contribution is often completely neglected and the total energy is given in term of the (pseudo) charge density alone. All interaction between the core and valence electrons is thus transferred to the pseudopotential. This implies a linearization of the interaction which can only be an approximation for the *explicitly* non local XC energy in LDA. If the core and valence charge densities are well separated in space this will introduce non serious errors as can be seen from the many success of the method. However if there is significant overlap between the two densities the linearization will lead to reduced transferability of the pseudopotential and to systematic errors in the calculated energy. In order to test the vality of the linearization of XC energy for Ga, present in the pseudopotential of ref. [18], we generated a pseudopotential corrected according to the method proposed by Louie, Froyen and Cohen [20] and currently known under the name of nonlinear core correction (NLCC). The idea is to evaluate

the XC energy using the total - rather than valence - charge density: this is achieved by adding the frozen core charge to the self-consistent valence charge. The core charge is computed once and for all in the same atomic calculation as the pseudopotentials. The core charge has significant effect only where the core and valence charge densities are of similar magnitude. It is without importance close to nucleus where most of the core charge resides. Therefore we replaced the full core charge, impractical to use within plane-waves expansion methods, with a partial core charge which is equal to the full one outside a radius r_0 midway between the nucleus and the point where core and valence charge densities intersect. We therefore assumed

$$\rho_{core}(r) = (a_{cc} + b_{cc}r^2)e^{-\alpha_{cc}r^2} \tag{A.1}$$

where $a_{cc}, b_{cc}, \alpha_{cc}$ are determined by fitting the expression above to the full core charge outside r_o. The norm-conserving pseudopotential have been generated using a scheme originally proposed by von Barth and Car [74]. In this scheme, the semilocal potentials are assumed to depend on few parameters. The usual choice is

$$V_l(r) = -\frac{Z_v}{r} erf(\sqrt{\alpha_c}r) + (a_l + b_l r^2)e^{-\alpha_l r^2} \tag{A.2}$$

where Z_v is the valence charge. The parameters α_c, a_l, b_l, and α_l are determined by minimizing the squared differences between the valence orbitals energies and the radial wave functions (beyond some core radius r_c) resulting from a self-consistent all-electron calculation and a pseudopotential one, made using Eqs. A.1 and A.2 [75]. The electronic configurations used for the generation of the pseudopotential are $4s^2 4p^1$, and $4s^{0.75}4p^{0.25}$ as in ref. [18]. The parameters of the NLCC-pseudototential are reported in table A.1.

The all-electron and pseudo wave functions for the two atomic configurations are com-

	cc	α_c	$l=0$	$l=1$	$l=2$
α	0.3112	0.5251	1.2534	0.9502	0.9921
a	0.3730		11.234	5.2681	−0.4214
b	1.2183		−6.4844	−2.3286	1.0750

Table A.1: Coefficient of the NLCC-pseudopotential for gallium. see Eqs. A.2 and A.1.

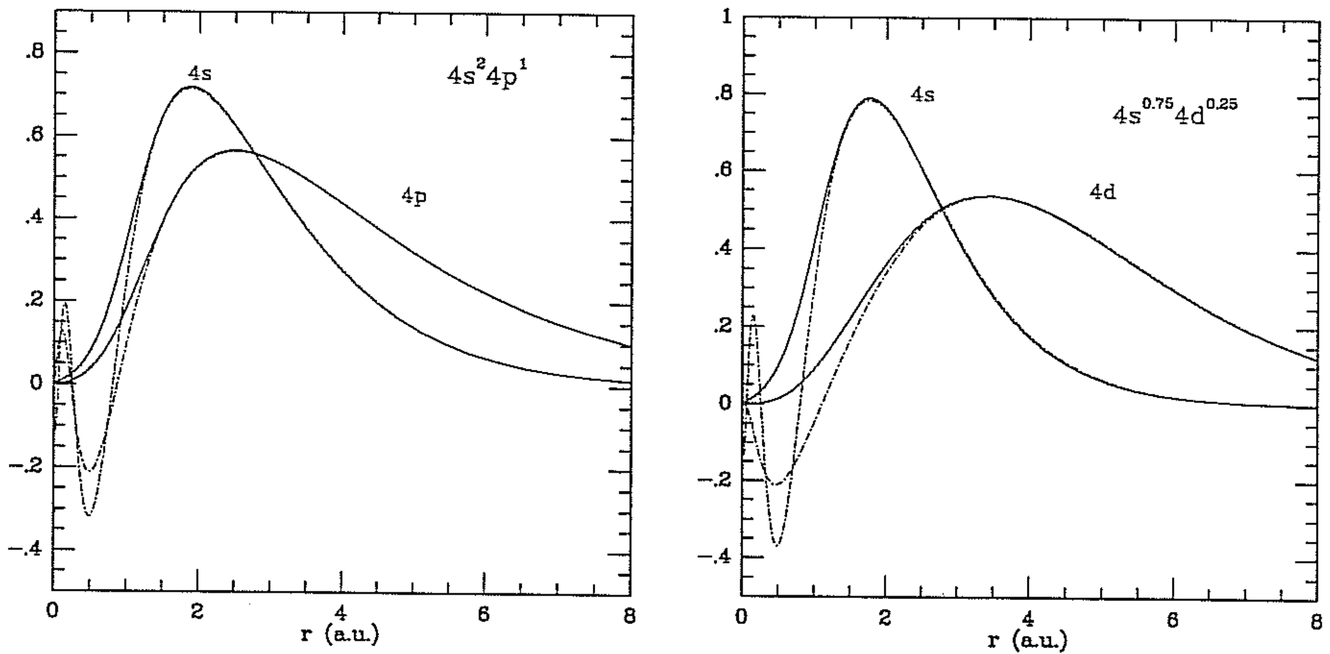

Figure A.1: Comparison between the pseudo and the corresponding all-electron radial wave functions for the configurations $4s^2 4p^1$, and $4s^{0.75} 4p^{0.25}$ for the NLCC pseudopotential of Ga.

pared in fig. A.1. The agreement between all-electrons and pseudo wave functions is worse for our NLCC-pseudopotential than for the pseudopotential in ref. [18]. The NLCC-pseudopotential used in our bulk calculations is not in the Kleinman-Bylander form. As discussed in chapter 3 the NLCC has negligible effects on the lattice parameters of gallium phases at equilibrium. However the bulk modulus increase of 7, 13 and 8 % in α-Ga, GaII and fcc respectively with respect to the values obtained with the pseudopotential in ref. [18]. Also the transition pressures suffer large changes as discussed in chapter 2. Nevertheless the main message of our NLCC results is that neglect of NLCC is not the source of the error in the equilibrium volume found with the pseudopotential in ref. [18].

Appendix B
Linear analytic method for Brillouin Zone integration in 2D

In this appendix we report the relevant formula for the 2D version of the 3D tetrahedron method for the calculation of electronic densities of states [65].

The contribution of the band n to the density of states for a 2D Brillouin Zone is

$$g_n(\epsilon) = \frac{1}{2\pi^2} \int_{\epsilon(\mathrm{k})=\epsilon} \frac{dl}{|\nabla \epsilon_n(\mathrm{k})|} \tag{B.1}$$

where $\int dl$ indicates the integral over the line $\epsilon(\mathrm{k}) = \epsilon$ in the IBZ (Surface IBZ in our application). Hereafter the inessential band index will be dropped. The integral is calculated as the sum of contributions from triangular microzones in the IBZ assigned by a uniform mesh of k-points. Therefore the density of states is decomposed as $g(\epsilon) = \sum_j g_j(\epsilon)$, where j indexes the microzones.

The eigenvalues $\epsilon(\mathrm{k})$ are evaluated only in the k points of the mesh which represent the vertices of the microzones. A value of $\nabla\epsilon$ is assigned to each microzone from linear interpolation of the values $\epsilon_1, \epsilon_2, \epsilon_3$ at the vertices of the triangular microzone. Then the contribution to the DOS from each microzone is approximated (apart from inessential constants) as $g_j(\epsilon) \sim S(\epsilon)/d\epsilon$, where $S(\epsilon)$ is the area of the polygon defined by the two parallel lines perpendicular to $\nabla\epsilon$ passing through the points at energy ϵ and $\epsilon + d\epsilon$ inside

the microzone j , and the boundaries of the microzone. This area is depicted schematically in figure B.1.

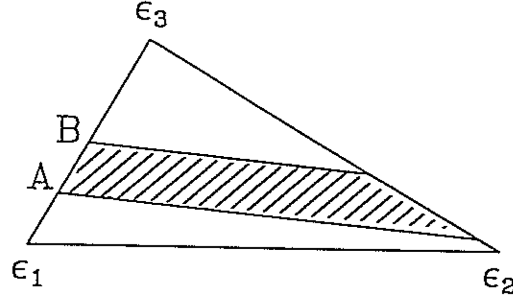

Figure B.1: The shaded area corresponds to the area S inside a triangular microzone which weights the contribution of the microzone to the DOS. See text.

At point A in figure B.1, $\epsilon(\mathbf{k}) = \epsilon$, and at point B $\epsilon(\mathbf{k}) = \epsilon + d\epsilon$, so the two parallel lines are separated by $d\epsilon/|\nabla\epsilon|$. ϵ_i at the vertices are indexed in order of increasing energy. The area $S(\epsilon)$ is equal to

$$S(\epsilon) = \frac{\Delta_1}{\Delta_{31}\Delta_{21}} 2A\, d\epsilon \quad \text{for } \epsilon_1 < \epsilon < \epsilon_2$$

$$S(\epsilon) = \frac{\Delta_3}{\Delta_{32}\Delta_{13}} 2A\, d\epsilon \quad \text{for } \epsilon_2 < \epsilon < \epsilon_3$$

$$S(\epsilon) = 0 \quad \text{for } \epsilon < \epsilon_1 \text{ and } \epsilon > \epsilon_3 \tag{B.2}$$

where $\Delta_{ij} = \epsilon_i - \epsilon_j$, and $\Delta_i = \epsilon - \epsilon_i$, and A is the area of the microzone.

For the calculation of the layer-resolved density of states the contribution from the microzone j, $g_j(\epsilon)$, is multiplied by the integral over the area $S(\epsilon)$ of the projection $p(\mathbf{k})$

of the slab wavefunctions on the relevant layer. Still the integral of $p(\mathbf{k})$ over S is performed by linear interpolation of $p(\mathbf{k})$ inside the microzone from the known values p_1, p_2, p_3 at its vertices.

Appendix C
Calculated STM image

The simple first order perturbation theory first applied to tunneling by Bardeen [76] was specified to tip-surface tunnelling in STM by Tersoff and Hamann [59]. In this approximation assuming a spherical tip with s-wave function and featureless density of states, and with other reservations discussed in details, e.g. in a recent review article [77], the differential tunneling conductance is simply proportional to the surface DOS at the Fermi level measured at the tip center $\mathbf{r_o}$

$$\frac{dI}{dV} \sim A\,\rho(\mathbf{r_o}, E = E_f) = A \sum_{n\mathbf{k}} |\psi_{n\mathbf{k}}(\mathbf{r_o})|^2 \delta(E_{n\mathbf{k}} - E_f) \tag{C.1}$$

the constant A depending on the radius, work function and DOS of the tip. For small tunnelling voltage

$$I \sim \rho(\mathbf{r_o}, E = E_f)\, V \tag{C.2}$$

so the variation in the current intensity at constant voltage and surface-tip separation reflects the variation of the local charge density which can be used as a surface topograph to the extent to which the wavefunctions at the Fermi level are sufficiently representative of the full set of occupied states. This may be the case in a regular metal, but it is clearly not so in a semimetal and even less in a semiconductor [77, 78].

The expression C.2 is used for our calculations of the theoretical STM images. The typical tip-surface separation in experimental devices is of the order of 5-8 Å, so the wavefunctions should be evaluated very far from the surface in order to compare with experimental results. On the other hand in a slab calculation the wavefunctions are well described only nearer the surface due to the finite thickness of the vacuum region (9Å in our case), and due to the low cutoff energy which can not describe the exponential decay very far from the surface. By plotting the logarithm of the charge density as a function of the distance from the surface we recognized a good exponential decay of our wavefunctions up to 3Å from the surface. However the exact form of the wavefunctions tail far from the surface is known as [59]

$$\psi_{n\mathbf{k}}(\mathbf{r}) = \Omega^{-\frac{1}{2}} \sum_{\mathbf{G}} a_{\mathbf{G}} e^{-(\kappa^2+|\kappa_G|^2)^{\frac{1}{2}} z} \, e^{i\kappa_G \mathbf{x}} \tag{C.3}$$

where x lie in the plane parallel to the surface, and z is perpendicular to the surface. $\kappa = 2\pi/h\,(2m\phi)^{\frac{1}{2}}$, ϕ is the work function, $\kappa_G = \mathbf{G} + \mathbf{k}_{||}$, and $\mathbf{G}$ is a surface reciprocal lattice vector. The $\psi_{n\mathbf{k}}$ obtained from the solution of the KS equation in reciprocal space read

$$\psi_{n\mathbf{k}}(\mathbf{r}) = \Omega^{-\frac{1}{2}} \sum_{\mathbf{G},g_z} b_{\mathbf{G},g_z} e^{i g_z z} \, e^{i\kappa_G \mathbf{x}} \tag{C.4}$$

where $(\mathbf{G}, g_z)$ are reciprocal lattice vector of 3D supercell. By equating eqs. C.3 and C.4 at a point z_o far from the surface, where ψ is well described by C.4, and hopefully also by C.3, we obtain the coefficient $a_{\mathbf{G}}$ in C.3, which let us evaluate the STM image at a point z arbitrarely far from the surface. For z in the range 5-8 Å, our STM images are not sensibly dependent on the position of the matching plane z_o at a distance from surface varying in the range 1.5-3 Å. Due to the use of a coarse mesh in the SBZ we included in the sum over

n, k in eq. C.1, states inside an energy window 0.5 eV large, below or above the Fermi level depending on the sign of the experimental tunneling voltage to be compared with. The work function in eq. C.3 is consequently modified as $\phi \rightarrow \phi - (E_{n,\mathrm{k}} - (E_f + 0.5\, eV))$ by imaging empty states, and $\phi \rightarrow \phi - (E_{n,\mathrm{k}} - E_f)$ by imaging filled states.

Bibliography

[1] R.W.G. Wyckoff, *Crystal Structures*, 2nd. ed. (Wiley, New York, 1962), Vol. I, p. 22. A word of caution is in order: of the six possible ways to assign a, b, c to the three crystal axes, at least three different versions can be found in literature.

[2] L. Bosio, J.Chem. Phys. **68**, 1221 (1978).

[3] L. Bosio, A. Defrain, H. Curien and A. Rimsky, Acta Crystallogr. B **25**, 995 (1969).

[4] L. Bosio, H. Curien, M. Dupont and A. Rimsky, Acta Crystallogr. B **28**, 1974 (1972).

[5] L. Bosio, H. Curien, M. Dupont and A. Rimsky, Acta Crystallogr. B **29**, 367 (1973).

[6] V. Heine, J. Phys. **C**, 222 (1968).

[7] J.E. Inglesfield, J. Phys. **C 1**, 1337 (1968).

[8] X.G. Gong, G.L. Chiarotti, M. Parrinello and E. Tosatti, Phys. Rev. **B 43**, 14277 (1991).

[9] J. Hafner and W. Jank, Phys. Rev. B 42, 11530 (1990).

[10] L.F. Vereshchagin, S.S Kabalkina, and Z.V. Toritskaya, Dokl. Akad. Nauk. SSSR **158**, 1061 (1965) [Sov. Phys. Dokl. **9**, 894, (1965)].

[11] see, e.g. E. Tosatti, in *The Structure of Surfaces II* , ed. by J.F. Van der Veen and M.A. Van Hove, Springer-Verlag (1988) p. 535.

[12] A. Dal Corso and E. Tosatti, Phys. Rev. B **47**, 9742 (1993).

[13] O. Züger and U. Dürig, Phys. Rev. B **46**, 7319 (1992).

[14] O. Züger, Phd Thesis, ETH Zurig (1992); O Züger and U. Dürig, Ultramicroscopy, **42**, 520 (1992).

[15] For a review on the application of Density Functional Theory in solid state calculations see W. E. Pickett, Computer Phys. Reports **9**, 115 (1989).

[16] J.P. Perdew and A. Zunger, Phys. Rev. **B 23**, 5048 (1981).

[17] L.Kleinman and D.M. Bylander, Phys. Rev. Lett. **48**, 1425 (1982).

[18] R. Stumpf, X. Gonze and M. Scheffler, unpublished.

[19] G.B. Bachelet, D.R. Hamann, and M. Schlüter, Phys. Rev. **B 26**, 4199 (1982).

[20] S. G. Louie, S. Froyen, and M.L. Cohen, Phys. Rev. **B 26**, 1738 (1982).

[21] D.D Johnson, Phys. Rev. **B 38**, 12087 (1988).

[22] E.R. Davidson, Computer Phys. Commun. **53**, 49 (1989).

[23] A. Baldereschi, Phys. Rev. **B 7**, 5212 (1973); D.J Chadi and M.L. Cohen, Phys. Rev. **B 8**, 5747 (1973); H.J. Monkhorst and Pack, Phys. Rev. **B 13**, 5188 (1976).

[24] C.L. Fu and K.M. Ho, Phys. Rev. **B 28**, 5480 (1983).

[25] M. Methfessel and A.T. Paxton, Phys. Rev. **B 40**, 3616 (1989).

[26] R.P. Feynman, Phys. Rev. **56**, 340 (1939).

[27] O. H. Nielsen and R.M. Martin, Phys. Rev. **32**, 3780 (1985); *ibidem* **32**, 3792 (1985).

[28] W.H. Press *et al*, *Numerical Recipes*, Cambridge University Press (Cambridge 1986).

[29] P. Gomes Dacosta, O. H. Nielsen and K. Kunc, J. Phys. **C 19** , 3163 (1986).

[30] M. Pasternak, J.N. Farrel and R.D. Taylor, Phys. Rev. Lett. **58**, 575 (1987).

[31] R.W. Powell, M.J. Woodman and R.P. Tye, Br. J. Appl. Phys. **14**, 432 (1963).

[32] A.R. Ubbelohde, *The Molten State of Matter* (Wiley, New York, 1978).

[33] Y. Waseda, *The Structure of Non-Crystalline Materials* (McGrow-Hill Inc., New York 1980), p.54.

[34] O. Hundery and R. Ryberg, J. Phys. **F 4**, 2084 (1974).

[35] R. Kofman, P. Cheyssac and J.Richard, Phys. Rev. B **16**, 5216 (1977).

[36] F. Greuter and P.Oelhafen, Z. Physik B **34**, 123 (1979).

[37] D.J. Stroud and M.J. Stott, J. Phys. **F 5**, 1667 (1975).

[38] W. Reichardt, R.M. Nicklow, G. Dolling and H.G. Smith, Bull. Am. Phys. Soc. 14, 378 (1969); Landolt-Börnstein, New Series III/13a, p.59 (Springer-Verlag, Berlin 1981).

[39] L. Bosio, R. Cortes, J.R.D Copley, W.D. Teuchert and J.Lefebvre, J. Phys. **F 11**, 2261 (1981).

[40] W.A. Reed, Phys. Rev. **188**, 1184 (1969).

[41] R. Griessen, H. Krugmann and H.R. Ott, Phys. Rev. B **10**, 1160 (1974).

[42] X.G. Gong, G.L. Chiarotti, M. Parrinello and E. Tosatti, Europhys. Lett. **21**, 469 (1993).

[43] A. Bererhi, A. Bosio and R. Cortes, J. Non-Cryst. Solids **30**, 253 (1979).

[44] W. Bückel and R. Hilsch, Z. Phys. **138**, 461 (1975); J. Berty, M.J. David and L. Lafourcade, J. Chim. Phys. **74**, 952 (1977).

[45] C.E. Weir, G.J. Piermarini and S. Block, J. Chem. Phys. **54**, 2768 (1971).

[46] M. Shinoi, sl Liquid Metals (Academic Press, New York 1977), p. 158.

[47] F.D. Murnaghan, Proc. Nat. Acad. Sci. U.S.A. **30**, 244 (1944).

[48] K.R. Lyall and J.F. Cochran, Canad. J. of Physics, **49**, 1075 (1971).

[49] C. Regnaut, J.P. Badiali and M. Dupont, J. Phys. Colloq. **C 8**, 604 (1980).

[50] R.O. Jones, preprint (1993).

[51] K. Balasubramanian, J. Phys. Chem. **94**, 7764 (1990).

[52] J. Zak *Irreducible Representations of Space Groups* (Benjamin, New York 1969).

[53] S. Gottlicher and E. Wolfel, Z. Electrochemie **63**, 891 (1959).

[54] M. T. Yin and M. L. Cohen, Phys. Rev. B **26**, 5668 (1982).

[55] G.L. Chiarotti, private communication.

[56] M. Bernasconi, G.L. Chiarotti, and E. Tosatti, Phys. Rev. Lett. **70**, 3295 (1993); M. Bernasconi, G.L. Chiarotti, and E. Tosatti, Surf. Sci., in press.

[57] . see, e.g., the articles by C.M. Bertoni and J.E. Inglesfield in *Interaction of atoms and molecules with solid surfaces*, edited by V. Bortolani, N.H. March and M.P. Tosi (Plenum, New York 1990), and references therein.

[58] W.R. Tyson and W.A. Miller, Surf. Sci. **62**, 267 (1977).

[59] J. Tersoff and D.R. Hamann, Phys. Rev. B **31**, 805 (1985).

[60] A. Baldereschi, S. Baroni and R. Resta, Phys. Rev. Lett. **61**, 734 (1988).

[61] R. Smoluchowski, Phys. rev. **60**, 661 (1944).

[62] A.J. Bennett and C.B. Duke, Phys. Rev. **160**, 541 (1967); J.Ferrante and J.R. Smith, Phys. Rev. B **31**, 3427 (1985).

[63] J.N. Swingler and J.C. Inkson, Solid State Commun. **24**, 305 (1977); J.P. Muscat and G. Allan, J. Phys. F **7**, 99 (1977).

[64] N. Roberts and R.J. Needs, Surf. Sci. **236**, 112 (1990); J.A. Appelbaum, G.A. Baraff and D.R. Hamann, Phys. Rev. B **14**, 588 (1976).

[65] O.Jepsen and O.K. Andersen, Solid State Comm. **9**, 1763 (1971); H.L.Skriver *"The LMTO Method"*, (Springer-Verlag, Berlin 1984), p. 194.

[66] R.M. Feenstra, J.A. Stroscio and A.P. Fein, Surf. Sci. **181**, 295 (1987).

[67] G.K. Wertheim and G. Crecelius, Phys. Rev. Lett. **40**, 813 (1978); B. Johansson, Phys. Rev. B **19**, 6615 (1979).

[68] A.A Chernov and L.V. Mikheev, Physica A **157**, 1042 (1989).

[69] B. C. Allen, in *Liquid metals Chemistry and Physics* edited by S. Z. Beer (Dekker, New York, 1972), p.161; A. A. Lucas, in *Collective Properties of Physical Systems*, edited by B. Lundqvist, S. Lundqvist, and V. Runnström-Reio (Academic, New York, 1973), p.169.

[70] The theoretical value of E_{coh} for Si is taken from M.T. Yin and M.L. Cohen, Phys. Rev. B **26**, 5668 (1982). The surface energy for Si(111)(1x1) is taken from R.D. Meade and D. Vanderbilt, Phys. Rev. B **40**, 3905, (1989). The surface energy for Si(111)(7x7) is taken from I. Stich *et al*, Phys. Rev. Lett. **68**, 1351 (1992).

[71] U. Dürig, private communications.

[72] J. W. Herman and H. E. Elsayed-Ali, Phys. Rev. Lett. **68**, 2952 (1992); *ibidem*, 1228 (1992); E. A. Murphy, H. E. Elsayed-Ali and J. W. Herman, Phys. Rev. B **48**, 4921 (1993).

[73] P. Carnevali, E. Ercolessi and E. Tosatti, Phys. Rev. B **36**, 6701 (1987); H. Häkkinen and U. Landman, Phys. Rev. Lett. **71**, 1023 (1993).

[74] U. von Barth and R. Car (unpublished).

[75] We thank A. dal Corso and P. Giannozzi for providing us the program for the generation of the pseudopotential.

[76] J. Bardeen, Phys. Rev. Lett. **6**, 57 (1961).

[77] J. Tersoff in *Scanning Tunneling Microscopy ans Related Methods*, edited by R.J. Behm, N. Garcia and H. Rohrer, Kluwer Academic Publishers (1990), pag. 77.

[78] A. Selloni, P. Carnevali, E. Tosatti, and C.D. Chen, Phys. Rev. B **31**, 2602 (1985).